Theory of Complex Lattice Quasicontinuum and Its Application to Ferroelectrics

Thesis by

Olga Kowalewsky

In Partial Fulfillment of the Requirements

for the Degree of

Doctor of Philosophy

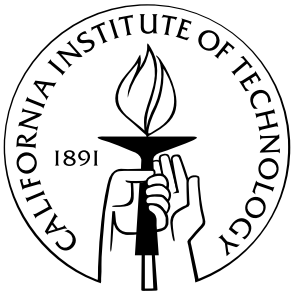

California Institute of Technology

Pasadena, California

2005

(Defended November 11, 2004)

For Erik

"...look closely, whenever rays are let in and pour the sun's light through the dark places in houses ...you will see many particles there stirred by unseen blows change their course and turn back, driven backwards on their path, now this way, now that, in every direction everywhere. You may know that this shifting movement comes to them all from the atoms. For first the atoms of things move of themselves; then those bodies which are formed of a tiny union, and are, as it were, nearest to the powers of the atoms, are smitten and stirred by their unseen blows, and they, in their turn, rouse up bodies a little larger. And so the movement passes upwards from the atoms, and little by little comes forth to our senses, so that those bodies move too, which we can descry in the sun's light; yet it is not clearly seen by what blows they do it."

Lucretius (c. 95-55 BC)

Acknowledgements

I would like to express my warmest gratitude to my supervisor Professor Michael Ortiz for his guidance, advice and support all of these years. It is only with his help that I was able to work on such an interesting and cutting edge project, and I cannot express my appreciation enough for the opportunity to do so. I have been very privileged to work with him and learned a great deal about mechanics from him.

Thank you to the other members of my thesis committee, Professor Kaushik Bhattacharya, Professor Guruswami Ravichandran, Professor James Beck and Professor Nadia Lapusta, for their many helpful comments and discussions.

Thanks also to Dr. Jarek Knap for his help, advice, and for writing the code which enabled me to conduct my research. A special thank you to Lydia Suarez for her guidance and assistance, and to the computer guru Marta Kahl, who rescued me many times from computer disasters.

Thank you to my husband Erik for his unconditional and infinite support which helped me to finish this work.

I would also like to thank my group, and in particular Puru, Rena, Marisol, Matt, Adrian, Bill, John, Matias, Yash, Xiangbin and Ben, for being great office mates and Arash for many valuable discussions.

Last, I gratefully acknowledge the financial support of the Army Research Office (DAAD-19-99-1-0319) through a MURI grant.

Abstract

Complex lattice Quasicontinuum theory is developed and applied to the description of ferroelectric phenomena. Quasicontinuum theory is a multiscale theory that provides a unified description of materials by combining atomistic and continuum approaches. It provides a seamless transition between atomistics and continuum, but the description of the material is derived directly from the underlying atomic structure, using the computationally expensive atomistics only where needed, at the location of phenomena of atomistic origin.

Complex lattice Quasicontinuum theory can be applied to complex lattice crystals consisting of many kinds of atoms. One highlight of it is treatment of each component lattice as separately and independently as possible. The component Quasicontinua are coupled through the microscopic forces within nodal clusters, making the complex atomistics of the heterogeneous lattice the basis of the description.

Ferroelectrics are especially suited to the application of Quasicontinuum theory. The nature of defects in ferroelectric materials is atomistic, but their influence over the material is long ranged due to induced elastic fields. Many different ferroelectric phenomena involving the perovskite ferroelectrics Barium Titanate and Lead Titanate are investigated and simulated. For Barium Titanate: the 180 degree domain wall structure and quasistatic crack under load. For Lead Titanate: the 180 degree domain wall structure and a domain wall step.

The results for the domain walls show that the domain wall thickness is atomistically small, of the order of few lattice constants, which is in agreement with recent ab initio molecular dynamics simulations, but we also observe long range effects resulting from the presence

of the wall. During crack loading in the sample of Barium Titanate we observe polarization changes around the crack tip which are consistent with experimental observations of an increase of fracture toughness. The quasicontinuum study of a domain wall step gives an atomistical view into the equilibrium structure of the step.

Quasicontinuum is able to model these phenomena with atomistic precision around the defects and non-homogeneities, and also capture the influence of long-ranging effects in the samples. These studies could also give valuable modeling input for larger scale continuum approaches.

Contents

List of Figures

List of Tables

Chapter 1

Introduction and Motivation

The goal of theoretical research is not only to understand and explain experiments, but also to predict and foresee new phenomena, behavior and properties as yet unrevealed by experimentation. Therefore, theories and numerical simulations must approach realistic conditions as closely as possible, ideally with all the quantity and complexity intrinsic to the real physical world.

At the present time, this ideal is far from reality. There is a constant push to develop more complex and better theories and to extend the limits of the existing ones.

Theoretical research in the field of mechanics has traditionally dealt with large structures like bridges, buildings and machines, subjects well suited to modeling by continuum mechanics. But with the advent of powerful tools in microscopy and the subsequent development of micro- and nano-technologies, the reach of mechanics has necessarily been extended to much smaller scales, approaching a level more typically considered by physics. The field of mechanics at this scale, which is growing quickly and getting a lot of attention recently, must consider subjects too small for traditional methods. Continuum mechanics is not equipped to accurately describe the atomistic interactions necessary for modeling subjects at this scale. But while the precise, but limited, methods of physics might provide this accurate description, mechanical modeling of atomistics at even the relatively small scale required by micro- and nano-technologies is computationally out of reach.

This is the area for which Quasicontinuum theory [1, 2] has been developed and where

it feels at home. Quasicontinuum theory is a multiscale theory. That is, it is designed to bridge the approaches of continuum mechanics and atomistics (solid state physics) by handling both length scales inside one problem. It uses the atomistic origin of phenomena and finite element method mechanisms to ultimately determine the continuum description, and to describe the constitutive response of the material. Quasicontinuum theory is able to give a smooth transition between the atomistic and continuum scales. It is able to adapt its meshing to the specific problem encountered, without patching, and so to model at a fine, atomistic, resolution where needed (near effects and high energy zones), but leave a coarse continuum mesh where deformation of the material body is homogeneous and small.

Quasicontinuum theory was originally developed to model crystals (for reviews see [3, 4, 5]), where all of the atoms in the crystal are of the same kind of element, and ordered in a Bravais lattice with the basis consisting of one atom. The theory was recently developed to model three-dimensional homogeneous lattices using an entirely non-local approach, and to be computationally faster and more efficient [6].

Of course, most crystals are "complex", in that they consist of many types of atoms. The majority of crystals of importance to the development of micro- and nano-technology are in this category. All ionic crystals are of a complex nature.

Of particular interest, ferroelectric crystals such as the perovskites Barium Titanate and Lead Titanate [7] have a complex lattice structure that could not be modeled with Quasicontinuum theory as previously developed. However, these materials are in particular need of the type of modeling Quasicontinuum theory can provide, because ferroelectric phenomena originate at the level of atomistics, but nevertheless have long ranging effects on the material. Solving these problems was our motivation for this work.

The objective of this work is twofold. First, we will discuss the development and extension of Quasicontinuum theory to describe crystals with a complex lattice structure. Second, we will discuss results obtained by using the newly developed complex lattice Quasicontinuum theory to accurately and seamlessly model, at the atomistic and continuum scale, prob-

lems concerning ferroelectric phenomena in Barium Titanate ($BaTiO_3$) and Lead Titanate ($PbTiO_3$) crystals.

One of the primary challenges in developing non-local complex lattice Quasicontinuum theory was that Quasicontinuum theory, as originally formulated, did not only deal exclusively with homogeneous lattices, but the structure of the theory itself assumed a homogeneous sample. For instance, the interpolation of atoms and approximation of energy and representative forces which were used in the original theory could not be used in samples with a complex lattice structure. These issues were resolved by separating the sample into discrete homogeneous Bravais sublattices and treating each sublattice as separately as possible, and then coupling the sublattices by using only the real microscopic forces between the atoms in them. This simple approach allowed us to reduce the computational effort needed. While there has been progress in extending Quasicontinuum theory to complex lattices using a local formulation [8, 9], which assumes homogeneous deformation inside each triangulation element, our approach is much different in that it uses a non-local formulation capable of atomistic resolution and thus able to capture atomistic defects.

Complex lattice Quasicontinuum theory was implemented as a C++ [10, 11] extension of existing C code [12], which itself needed extensive modification.

After developing complex lattice Quasicontinuum theory, we applied it to several important problems concerning properties of the ferroelectrics $BaTiO_3$ and $PbTiO_3$. Ferroelectrics are crystals, in which spontaneous electric polarization can be reversed by application of an external electric field. Ferroelectrics are in thermal equilibrium in each polarization state [13]. Instructive reviews of ferroelectric phenomena can be found in [14, 15, 16, 17, 7]. For recent developments refer to [18, 19, 20, 21]. Ferroelectrics are widely used in actuators, capacitors and transducers for their excellent piezoelectric and dielectric properties [7], but recently they are in development as very important components of Dynamic Random Access Memory (as thin-film capacitors) [22, 23] and Non-Volatile Random Access Memory (used as memory elements themselves) [24, 25, 13] devices. The ferroelectric memory devices would

have many advantages over the now widely used magnetic memories: low-voltage operation, small size, radiation hardness and very high speed.

Some of the most researched ferroelectrics are Barium Titanate and Lead Zirconium Titanate (PZT). PZT is a family of ferroelectric materials of the formula $Pb(Zr_xTi_{1-x})O_3$ with Lead Titanate $PbTiO_3$ being an important end member of this family.

Below a certain Curie temperature (specific to each material) ferroelectrics exhibit spontaneous polarization. But often the microstructure of a particular ferroelectric sample is very complicated. Ceramic samples consist of many grains with different domains (regions of different spontaneous polarization) and crystal samples also consist of many domains. Therefore understanding domain wall structure and the properties of domain boundaries (domain walls) is very important in designing efficient ferroelectric devices. Building of domain wall steps is part of the mechanism of polarization switching, the property which is exploited in many devices. Therefore, understanding the structure and mechanism of steps is very important. Last, the perovskite ferroelectrics Barium Titanate and PZT are very brittle and can be destroyed by fracture, so understanding fracture in these materials is a key to building reliable devices. Thus our research on the structure of domain walls, domain wall steps and fracture in ferroelectrics deals with the most important phenomena used for building devices.

Considerable research on domain walls both static and dynamic (which is related to building of steps), and fracture in ferroelectrics has been done with phenomenological continuum theories. Only recently has some research been done considering the discrete atomistic nature of the material with ab initio input. But these investigations have been of a very small scale and do not consider long ranging effects. Quasicontinuum theory handles both the fact that these phenomena arise from complex ab initio couplings, which continuum mechanics has difficulties addressing, and the fact that there are long ranging effects in the sample, which cannot be captured by molecular dynamics. For specific literature citation, refer to the particular application chapter.

For $BaTiO_3$ investigations, we used the potential devised by Goddard, et al. [26, 27] with slight modification, and for $PbTiO_3$ investigations, we used the potential devised by Sepliarsky et al. [28]. In both cases, we applied the Wolf et al. [29] summation rule to handle the electrostatic components of the atomic interactions.

We first examined the problem of a 180 degree domain wall in $BaTiO_3$. We were able to simulate the equilibrium configuration of an approximately 11 million atom sample without imposing periodic boundary conditions. We found that the domain wall thickness, the area in which most of the polarization switching occurs, lies in the range of 4-6 unit cells, or 1.5-2.5 nm. These figures agree with experimental results [30, 31], and also with existing theoretical and numerical calculations [32, 33]. Moreover, we were also able to see long range effects, arising from the presence of the wall, which previous molecular dynamics simulations were unable to detect.

To demonstrate the ability of complex lattice Quasicontinuum theory to handle more challenging problems, we examined the problem of a crack in an over 100,000 atom $BaTiO_3$ sample. We were able to model quasistatic loading of the crack in the sample with automated adjustment of the resolution with increasing load. The sample showed a systematic polarization pattern building around the crack tip with initiation of domain layers. We found that this pattern grows and becomes more distinct with growing crack load. Our results are in qualitative agreement with observed changes in fracture toughness in ferroelectrics, which is attributed to domain switching in front of a crack tip [34, 35]. Our simulated sample captures a resolution still too small for current ferroelectric fracture measurements and continuum approaches, and can give continuum theories insights about the correct mechanisms and parameters which should be used for the model.

We then simulated the equilibrium configuration of a 180 degree domain wall in a 400,000 atom sample of $PbTiO_3$. This sample size would have been too large to model using an (atomistic resolution) molecular dynamics simulation with the Sepliarsky et al. potential, because the non-electrostatic portion of the potential is very far reaching. We found that

the area where most of the switching of the polarization occurred was in the 2-6 unit cells adjacent to the wall, giving a domain wall thickness of 1 nm to 2.5 nm. This is consistent with recent ab initio calculations [36] and experimental results [37]. But we were able to calculate much larger regions around the domain wall than the available ab initio calculations. We were also able to see long ranging effects from the presence of the wall, such as a long "tail" of polarization adjustments originating from the wall and extending far into the bulk of the sample.

Last, we calculated the equilibrium configuration of a 180 degree domain wall in a sample of $PbTiO_3$, with a step in the wall surface. Our calculations show, at an atomistic level of precision, that polarization around the step tends to arrange in such a way to minimize the net bounded polarization charge at the interface and smooth out the sharp step transition. We see a large region affected by the presence of the step.

This work is designed as follows. Chapter 2 introduces Quasicontinuum theory, specific to homogeneous lattices, as in [2, 6]. Chapter 3 explains the development of complex lattice Quasicontinuum. Chapter 4 is devoted to its numerical implementation. Chapters 5 and 6 introduce the potentials and the electrostatic summation rule used in this work. Chapters 7-10 are devoted to applications: $BaTiO_3$ 180 degree domain wall configuration (Chapter 7); crack in a $BaTiO_3$ tetragonal phase sample (Chapter 8); $PbTiO_3$ 180 degree domain wall configuration (Chapter 9) and step in a 180 degree domain wall in $PbTiO_3$ (Chapter 10). Extensive literature reviews specific to each problem can be found in each applicable chapter.

Chapter 2

Quasicontinuum

2.1 Quasicontinuum Bridges Continuum Mechanics and Solid State Physics

The traditional continuum mechanics approach to theoretical research in mechanics assumes that materials are comprised of an infinitely divisible continuum medium with a constitutive behavior taken as a phenomenological input which does not change upon zooming in to smaller and smaller parts of the material. Continuum mechanics has been very valuable for many applications. One of its advantages is that it can describe the behavior of large scale bodies, which we use in everyday life. But the problem with continuum mechanics has always been the constitutive relations, which describe the deformation reaction of the body to stress [38, 39, 40, 41]. To some degree they are external phenomenological input to a given boundary value problem. In many cases the relations come from the experimental observations and are backed by them. However when constitutive relations are selected for a particular model, there is always a possibility that through this the system will be constrained and will not describe real physical behavior.

Contrary to continuum mechanics, the solid state physics approach [42] describes bodies consisting of discrete parts: atoms. The nucleus and electrons [43], [44] are the primary building blocks which get most of the attention in solid state physics. Knowing eigenfunctions

of the quantum mechanics Hamiltonian written out for the particular system of atoms, we can describe what is happening or going to happen with the system. This information is very precise. But the mathematical, numerical and, finally, computational burden largely scales with the number of atoms involved, resulting in investigators being unable to analyze even relatively small systems using supercomputers. The systems which are calculated this way are not found in our everyday life, and very often these systems cannot be reproduced even in very extensive experiments.

Quasicontinuum bridges the approaches of continuum mechanics and atomistics (solid state physics). It uses continuum mechanics, but derives constitutive relationships from atomistics. Or, seen a different way, it uses atomistics but involves scaling and interpolating schemes from continuum mechanics and the finite element method for description of much larger systems. Before we describe in detail what Quasicontinuum theory is, we would like to mention one more thing which motivated its development.

2.2 Quasicontinuum is a Multiscale Model

The importance of multiscaling and the multiscaling origin of many central phenomena in science cannot be overstated.

Many problems considered in mechanics have different length scales involved in them. While there are many examples, two of them have a particular relation to this work.

Consider a nano-indentation at the elastic-plastic material limit. There are few dislocations, perhaps tens, evolving under the indentor which require explicit atomistic treatment. And there is a much larger scale represented by the indentor itself and the material far away from the indentor tip which can be treated with continuum methods.

Another example is a very small crack in a large specimen. One length scale is the crack itself, with possible dislocations emitting from the tip or breaking of the bonds resulting in crack propagation. The other length scale is far away from the crack where the material can

be again theoretically described as a continuum.

More examples of multiscale phenomena are considered and simulated in this work.

Quasicontinuum is truly a multiscale model. It bridges atomistics and continuum. It can handle both length scales inside one problem. As in the above example of nano-indentation it can explicitly follow nucleation and movement of every single dislocation under the indentor and also track the deformation of the entire large specimen using approaches similar to continuum mechanics, but deriving the constitutive relations from the underlying atomistics. Similarly, in the nano or micro crack example, Quasicontinuum can follow movement of every single atom near the crack tip where the stress energy density is very high, but still use a continuum approach further away from the crack tip.

Quasicontinuum, in contrast to other multiscale methods available, gives a smooth transition between atomistics and the continuum [45]. It uses the atomistic origin of phenomena to ultimately determine the continuum description, and describe the constitutive response of the material.

Importantly Quasicontinuum also has the criteria and capability to adapt meshing to the specific problem, changing based on different conditions in time and loads. There is no patching required between different length scale zones. Quasicontinuum makes a smooth mesh or transition from different length scales, giving a fine, atomistic resolution near defects and high energy zones, where it is needed, and leaving the coarse continuum mesh where deformation of the material body is homogeneous and small. Quasicontinuum does not have to make any assumptions about the deformation energy concentration a priori - the algorithm scheme will resolve automatically which regions to treat using which length scales.

2.3 Original Development of Quasicontinuum

Quasicontinuum was originally developed by Tadmor, Phillips and Ortiz. It was first introduced in [1] and then described in more detail in [2]. Since then many differ-

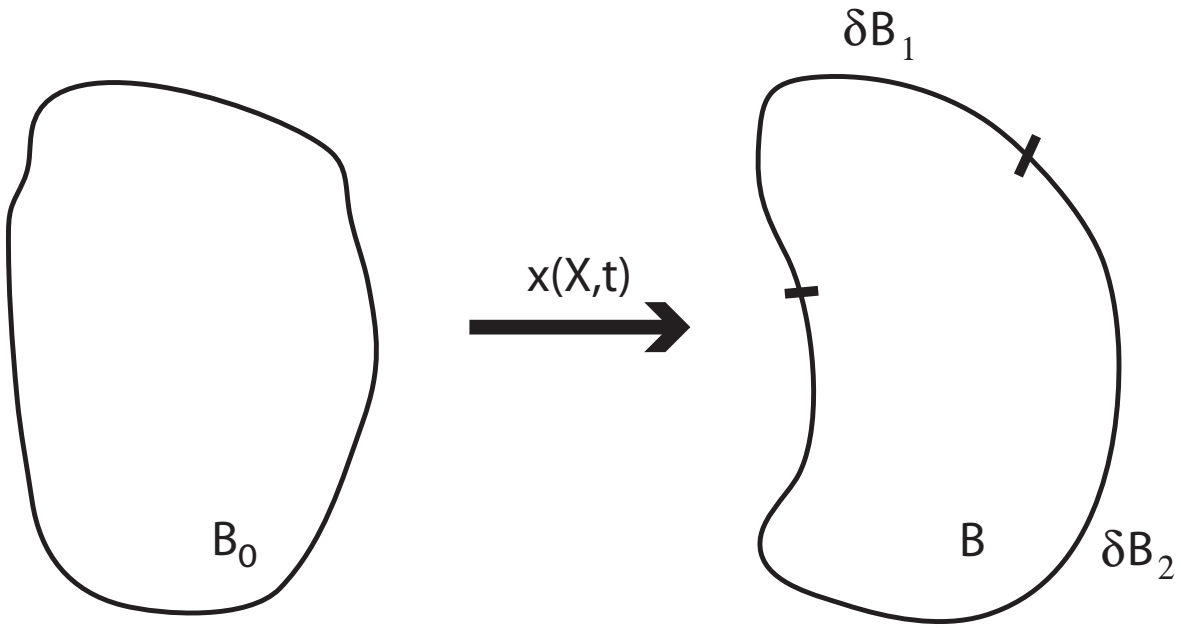

Figure 2.1: A continuum boundary value problem.

ent variants have been developed over a series of publications with numerous examples [46, 47, 48, 49, 45, 50, 51, 52, 6, 53, 54]. A good overview is presented by Miller and Tadmor in [5]. Many more publications and resources are available in the specifically designated web page [55].

To be able to describe the Quasicontinuum theory, show its relations to atomistics and continuum models, show its multiscale origin and also to introduce the notation, we first briefly review a general continuum mechanics boundary value problem, and also the finite element method and lattice statics approaches.

2.3.1 Continuum Boundary Value Problem

Consider a general boundary value problem [38, 39, 56, 41], see Figure 2.1, where a material specimen or a body occupies a reference configuration $B_0 \in R^3$. Deformation and motion of

this body is described by the deformation mapping $\mathbf{x}$:

$$\mathbf{x}(\mathbf{X}, t) : R^3 \rightarrow R^3$$

which is a function of time t and the coordinates from the undeformed body domain $\mathbf{X} \in B_0$. The body is subject to the following boundary conditions: fixed displacement $\tilde{\mathbf{x}}$ on part of the boundary ∂B_1 (Dirichlet boundary conditions) and traction $\tilde{\mathbf{T}}$ on the other part ∂B_2 (Neumann boundary conditions)[57, 58]. There is also a force acting on the body B, where the force per unit volume of the body is $\mathbf{G}$.

The potential energy of the body in a deformed configuration $\mathbf{x}$ is defined as

$$E^{pot}(\mathbf{x}) = \int_B w(\mathbf{x})\ dv - \int_B \mathbf{G}\mathbf{x}\ dv - \int_{\partial B_2} \mathbf{T}\mathbf{x}\ ds$$

where $w(\mathbf{x})$ is the strain energy density. The first and second integrals are taken over volume and the third integral over the surface of the body B.

According to the principle of minimum potential energy [59, 38, 39, 56, 41], given the displacement boundary conditions, traction boundary conditions and the body force, the body will assume the configuration $\mathbf{x}^{eqv}$, which is in agreement with displacement boundary conditions and also minimizes the potential energy

$$E^{pot}(\mathbf{x}^{eqv}) = \min_{\mathbf{x}} E^{pot}(\mathbf{x})$$

Once we determine how the strain energy density depends on the deformation of the body, the problem becomes solely a minimization problem of finding the right deformation mapping $\mathbf{x}$ satisfying the given boundary conditions. The constitutive relations which give the relation between strain and stress in the body will provide this input. We need to make an educated guess about what model of constitutive relations to use in a particular case. There are many models available and we have to choose one which is most suitable

for our purposes depending on what material constitutes the body. Often if we have any inhomogeneity, defects, interfaces or boundary in the problem, we would have to consider a specific constitutive relation just for that particular region, making sure that the jump conditions for strain and stress are satisfied. This can become quite cumbersome.

2.3.2 Finite Element Formulation

Finite element method [60, 61, 62, 63] applied to the continuum boundary value problem reduces dramatically the degrees of freedom of the problem and the computational effort. Let us divide B into finite elements. The nodes of this partitioning will be the only non-constrained variables of the system with the deformation of the rest of the body determined by interpolation from the deformation at the nodes. The deformation mapping thus becomes

$$\mathbf{x}_h(\mathbf{X}, t) = \sum_{a=1}^{N} \mathbf{x}_a(t) N_a(\mathbf{X})$$

where $a = 1, \ldots, N$ runs over N nodes of the mesh, $\mathbf{x}_a(t)$ is the node a coordinate at time t and $N_a(\mathbf{X})$ is the shape function of node a at position $\mathbf{X}$. The subscript h is the notation accepted in finite element definition and refers to the size of the mesh as whole such as, for example, the size of the smallest element. It distinguishes a particular mesh for reference purposes.

Shape functions $N_a(\mathbf{X})$ are interpolation functions,which are defined on the undeformed body B_0 and have the following properties:

(i) The functions should belong to at least C_0.

(ii) Outside the elements which include the node a, the shape function $N_a(\mathbf{X})$ is identically zero.

(iii) If b is another node in the mesh, then

$$N_a(\mathbf{X}_b) = \delta_{ab}$$

(iv) For any $\mathbf{X} \in B_0$

$$\sum_{a=1}^{N} N_a(\mathbf{X}) = 1$$

For the rest of the formulas in this section, we consider $\mathbf{x}$ being not the coordinates, but the displacement field. The displacement of a point is the difference between its coordinates in deformed and undeformed configurations. The interpolation with the shape functions happens exactly as with the coordinates.

Since the deformation of the body is being interpolated from the nodal coordinates or displacements, the displacements are the only true variables or unknowns of the boundary value problem. With the above interpolation, the energy functional becomes

$$E^{pot}(\mathbf{x}) \approx E^{pot}(\{\mathbf{x}_a\}) = \int_B w(\{\mathbf{x}_a\})\, dv - \sum_{a=1}^{N} \left[\int_{B_0} \mathbf{G} N_a(\mathbf{X})\, dV - \int_{\partial B_{02}} \mathbf{T} N_a(\mathbf{X})\, dS \right] \mathbf{x}_a$$

The equilibrium state can be found as

$$E^{pot}(\mathbf{x}^{eql}) \approx E^{pot}(\{\mathbf{x}_a^{eql}\}) = \min_{\{\mathbf{x}_a\}} E^{pot}(\{\mathbf{x}_a\})$$

In the linear elasticity theory [38, 39, 64], we can assume linearity between stress and strain, the relation for the strain energy becomes:

$$\int_B w(\{\mathbf{x}_a\})\, dv = \sum_{ab} \left[\int_B C_{ijkl} N_{a,j} N_{b,l}\, dV \right] x_{ai} x_{bk}$$

where C_{ijkl} is the elasticity tensor and according to the Einstein convention i, j, k and l are summed over.

Introducing the stiffness matrix as

$$K_{aibk} = \int_{B_0} C_{ijkl} N_{a,j} N_{b,l} \, dV,$$

and the driving force vector as

$$F_{ai} = \int_{B_0} G_i N_a \, dV + \int_{\partial S_{02}} T_i N_a \, dS$$

and introducing the double indices I and J as

$$I = \{ai\}, \qquad J = \{bk\}$$

we are left with the following sum for the potential energy, which can also be written as a vector equation

$$E^{pot}(\{\mathbf{x}_a\}) = x_I K_{IJ} x_J - F_I x_I = \frac{1}{2}\mathbf{x^T K x} - \mathbf{F x}$$

The minimum of the potential energy is achieved at

$$\mathbf{x}^{eqv} = \mathbf{K}^{-1}\mathbf{F}$$

The integrals for the stiffness matrix and driving force vector in the above equations can be calculated using numerical quadrature. For each element Ω_e in the mesh, we select Q representative points $\mathbf{Y}_q$ in the element and substitute the integral

$$\int_{\Omega_e} f(\mathbf{X}) dV$$

with the sum

$$\sum_{q=1}^{Q} w_q \cdot f(\mathbf{Y}_q)$$

Q is the order of quadrature rule. The weights w_q are specific to the set $\{\mathbf{Y}_q\}$ and the way

we want the integral to be approximated. Often people use a specific function for $f(\mathbf{X})$, like the shape functions which should integrate $\int f(X)dV$ exactly over the body and so they can determine the weights.

2.3.3 From Quantum Mechanics to Lattice Statics: Atomistic Handling of a Crystalline Material Body

From a totally different prospective, lattice statics considers a material body consisting of atoms. This is a much more realistic view point for consideration of materials, and becomes the only possibility as the scale becomes smaller. Atoms interact with each other and move due to this interaction, which resolves on the larger scales to the more commonly known strains and stresses in the material.

A system of atoms can be best described with quantum mechanics [65]. Quantum theory was founded between 1923 and 1927 by contribution of many scientists. Schrödinger developed the general formalism [66, 67, 68, 69] based on the works of de Broglie [70], which attributed a wave-corpuscle duality to all microscopic objects. Dirac [71, 72, 73] further developed the formalism of Quantum theory, which was extended by works of Born [74], Heisenberg [75] and Bohr [76, 77].

Microscopic objects appear under two apparently irreconcilable aspects, the wave aspect on one hand, exhibiting the superposition property characteristic of waves, and the corpuscular aspect on the other hand, namely localized grains of energy and momentum.

Therefore a system of N particles should be described by a wave function $\Psi(\mathbf{r}_1, \ldots, \mathbf{r}_N; t)$, where r_i is the coordinate assigned to particle i, t is the time. The wave function completely defines the state of the system. In case of one particle, the intensity at a given point and at a given time of the wave function associated with that particle gives the probability of finding the particle at that point and that time.

The propagation of the wave-particle is described by the Schrödinger equation

$$i\hbar\frac{\partial}{\partial t}\Psi(\mathbf{r}_1,\ldots,\mathbf{r}_N;t) = H(\mathbf{r}_1,\ldots,\mathbf{r}_N;\frac{\hbar}{i}\frac{\partial}{\partial\mathbf{r}_1},\ldots,\frac{\hbar}{i}\frac{\partial}{\partial\mathbf{r}_N};t)\Psi(\mathbf{r}_1,\ldots,\mathbf{r}_N;t) \qquad (2.1)$$

where $\hbar$ is a Planck's constant and the function

$$H(\mathbf{r}_1,\ldots,\mathbf{r}_N;\frac{\hbar}{i}\frac{\partial}{\partial\mathbf{r}_1},\ldots,\frac{\hbar}{i}\frac{\partial}{\partial\mathbf{r}_N};t)$$

is called the Hamiltonian operator of the system.

For our purposes of considering only static systems, where the Hamiltonian H does not explicitly depend on time t, we can introduce a time independent wave function $\psi(\mathbf{r}_1,\ldots,\mathbf{r}_N)$ as

$$\Psi(\mathbf{r}_1,\ldots,\mathbf{r}_N;t) = \psi\mathbf{r}_1,\ldots,\mathbf{r}_N)\exp^{-i\frac{Et}{\hbar}}$$

then equation 2.1 becomes

$$H\psi(\mathbf{r}_1,\ldots,\mathbf{r}_N) = \left[-\frac{\hbar^2}{2m}\Delta + V(\mathbf{r}_1,\ldots,\mathbf{r}_N)\right]\psi(\mathbf{r}_1,\ldots,\mathbf{r}_N) = E\psi(\mathbf{r}_1,\ldots,\mathbf{r}_N) \qquad (2.2)$$

where Δ is the Laplace operator in particle coordinate space and V is the potential field in which the particle exists.

The solution of the eigenvalue equation 2.2 gives the eigenwave function ψ of the operator H to the eigenvalue E. E represents the stationary energy of the solution.

For more details on Quantum theory refer to [78, 79, 80].

It is very difficult to solve this problem even assuming a very simple potential form. Numerical calculations are very extensive and one can calculate systems of only a few tens to a few thousands of atoms depending on the approximations made.

To ease the problem, many calculations consider the use of effective potentials [81, 82]. Depending on the physics of the underlying systems of atoms, a potential energy function

can be introduced. It is a function of only atomic coordinates in the system, which gives by minimization the equilibrium state of the system. It is important to note here, that this function is much more physically based than a constitutive law. The parameters of the function are carefully fitted to the quantum mechanics calculations.

The principle of minimum energy can also be formulated for this case, stating that the material body will assume a configuration (meaning each atom will assume a position), consistent with the boundary conditions given, that minimizes the potential energy of the body:

$$\min E^{pot}(\mathbf{x}_1, \mathbf{x}_2, \ldots, \mathbf{x}_n)$$

Here $\mathbf{x}_i$ is the position of atom i.

After determining the equilibrium atomic coordinates and atomic inner forces, we can always determine continuum strain and stress by averaging them out, if the concept of continuum can be applied to the body or some parts of it.

The atomistic approach is much more precise and does not require a priori assumptions about the energy dependence on strain, but it is also very cumbersome and requires an enormous amount of calculations. The problem is, of course, that even a small body in everyday life constitutes many atoms (approximately the order of Avogadro's number: 1mol=$6.022 \cdot 10^{23}$ [83]), and having to follow and explicitly deal with each one of them requires an enormous amount of computer time and resources even for relatively small systems.

2.3.4 Original Local and Nonlocal Two-Dimensional Quasicontinuum Theory

The Tadmor et al. Quasicontinuum theory applies to crystals which have a systematic crystal structure in undeformed configuration. In this theory, the crystal has to be homogenic, i.e., only one atom per Bravais lattice. This means all the atoms in the crystal have to be the same kind of element and ordered in a Bravais lattice with the basis consisting of only one

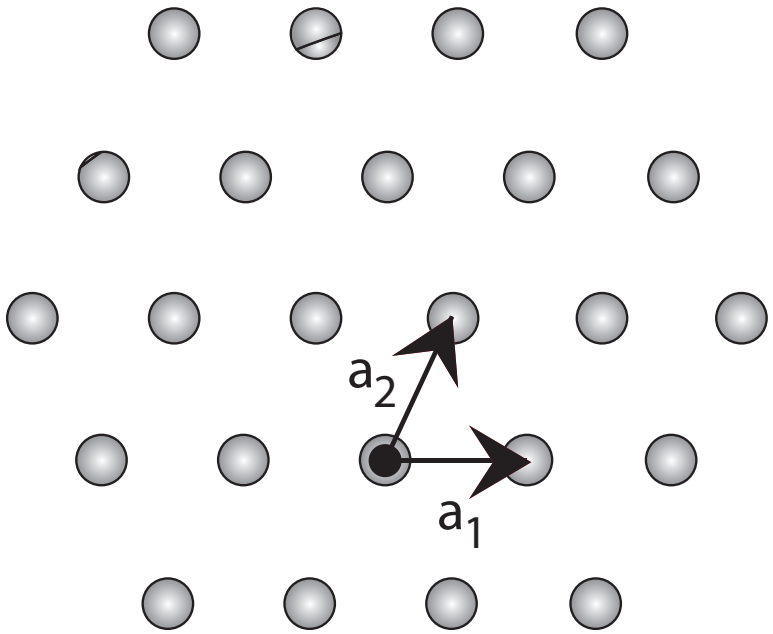

Figure 2.2: An example of a Bravais lattice.

atom.

A Bravais lattice is an infinite array of discrete points with an arrangement and orientation that appears exactly the same, from whichever of the points the array is viewed [84]. See an example of a Bravais lattice in two dimensions in Figure (2.2). A three-dimensional Bravais lattice consists of all points with position vectors $\mathbf{R}$ of the form

$$\mathbf{R} = l_1\mathbf{a}_1 + l_2\mathbf{a}_2 + l_3\mathbf{a}_3,$$

where $\mathbf{a}_1$, $\mathbf{a}_2$ and $\mathbf{a}_3$ are three linearly independent vectors (that is, not in the same plane) and l_1, l_2 and l_3 range through all integer values. The vectors $\mathbf{a}_i$ are called lattice vectors and are said to generate the lattice. Integers l_i are called lattice coordinates. The Quasicontinuum theory was originally developed for two dimensional crystals, but is not limited to it [6].

Consider a homogeneous crystal. With the lattice statics previously mentioned, the

energy of the crystal would be a function of all atoms, positions $\mathbf{x}_1, \ldots, \mathbf{x}_N$

$$E = E(\mathbf{x}_1, \mathbf{x}_2, \ldots, \mathbf{x}_N)$$

This is still pure lattice statics, leaving us with too many degrees of freedom to be able to calculate a realistic sample.

It should be noted that in atomistics we talk about coordinates of the body rather than displacements. The coordinates are the ones which the energy truly depends on. This is in contrast to continuum mechanics, where displacements from the undeformed configuration are the prime variables. Knowing the undeformed initial configuration of the atoms, it is trivial to calculate displacements from coordinates and vice versa. And the undeformed configuration is almost always known or can be determined.

What we want to do is to use the finite element approach to interpolate some of the atom coordinates or displacements based on the coordinates or displacements of some carefully chosen atoms, which we will call in the future representative atoms. There is an intuitive approach at how to choose them: in the areas with high energy density, where things might have to be considered atom by atom, i.e., atomistically, we should choose a lot of atoms as representative atoms. And in the areas with small homogeneous deformations, far away from the defects, it should be sufficient to choose a smaller number of atoms, only every 10th or 100th atom or even coarser. We do not have to be absolutely sure, a priori, how to select the atoms. The algorithm's build feature, which we refer to as adaptive mesh refinement, will correct the density of the atoms selected depending on the problem.

Those selected atoms will become nodes of the triangulation, see Figure (2.3). The triangulation will introduce a subdivision of the body with ways to interpolate the positions of an atom inside an element based on the position of the atoms to which the nodes are bounded. It is exactly the same interpolation and triangulation as in finite element method, only that we have a discretization of space rather than a continuum. It makes sense to interpolate only

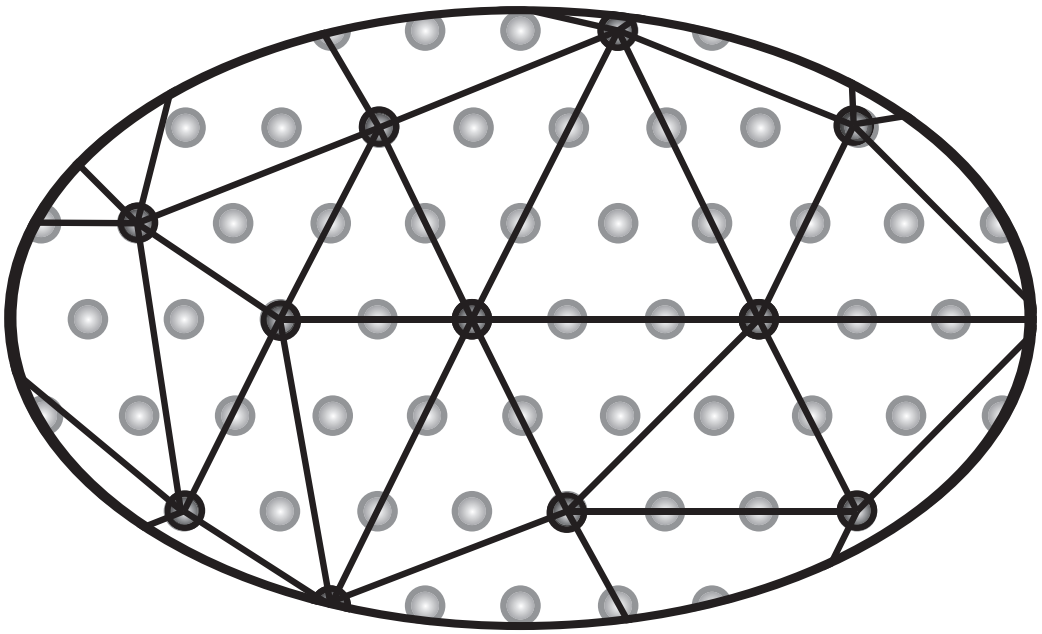

Figure 2.3: A lattice triangulation.

the positions of atoms which are uniquely defined in undeformed configuration. "Nothing", or vacuum, is located in between. One of the reasons, although not the main one, why this theory is much easier to introduce for the homogeneous crystals is that you need to know in the undeformed configuration where the atoms are located. This is much easier for a homogeneous Bravais lattice. A very simple algorithm specific to each lattice structure, plus three Bravais lattice vectors, are enough to determine the initial undeformed position of any atom in the lattice. A complicated database of initial positions of atoms is unnecessary, making calculations faster.

The same shape functions we know from finite element method will take care of interpolating positions of the atoms which are not nodes

$$x_h(X) = \sum_{a,\ nodes} N_a(X) \cdot x_h(X_a),$$

where $x_h(X_a)$ is the deformed coordinate of node a. Note that we drop the time dependence of the deformed coordinates for the simplicity of the formulas, but it can still be thought of

implicitly.

Now that many of the atoms are constrained kinematically through triangulation as discussed above, the energy becomes a true function of only the positions of representative atoms:

$$E(\{x\}) \approx E(\{x_h\}) = E(\{x_h(X_a)\}) = E(\{x_a\}).$$

With accordance with principle of minimum potential energy, the energy now needs to be minimized only with respect to the positions of representative atoms $x_h(X_a)$, reducing drammatically the number of variables in the system:

$$\min_{\{x\}} E(\{x\}) \approx \min_{\{x_a\}} E(\{x_a\}).$$

An important next step in the chain of assumptions is that the total potential energy of the crystal should have a site-wise additive decomposition

$$E(\{x\}) = \sum_i E_i,$$

where the index i goes over every lattice site. Most of effective potentials allow this decomposition.

This allows us to approximate the energy based on the representative atoms energy contribution

$$E(\{x\}) = \sum_{a=1}^{N} n_a E_a$$

with some weights n_a for each representative atom. With this expression, knowing the weights, we will be able to find the total energy of the system, summing and visiting only the representative atoms.

To minimize the energy function, we need to compute its derivatives with respect to the positions of the nodal atoms. Depending on the minimization algorithm (or root searching algorithm, since an extremum of a smooth enough function will be where all the partial

derivatives vanish) we might have to also calculate second order partial derivatives. We found that conjugate gradient method was a very fast and reliable way to solve this equation, which requires only the first order derivatives. Therefore, and also to keep things simple, we will only mention how to compute the first order derivatives of this equation.

There are two approaches used to minimize the computational effort in this formulation of Quasicontinuum: elements are split into local and non-local ones [2]. A local element "sees" the state of deformation within its own domain only, while a non-local element "sees" the deformation of other (mostly neighboring) elements as well. The local elements are used in the coarse mesh, where the crystal may be assumed to follow the Cauchy-Born rule. In the fine mesh limit, the approach used is similar to lattice statics.

2.3.4.1 Local Quasicontinuum Elements

The entire element Ω_e considered to be local has a constant homogeneous deformation inside. The deformation of the element follows the deformation gradient defined on a continuum scale $\mathbf{F}$ due to the Cauchy-Born rule [84], defining the positions of the atoms as

$$\mathbf{x}(\mathbf{l}) = \mathbf{F}\mathbf{X}(\mathbf{l})$$

The strain energy density W in the element which can be computed from atomistic coordinates becomes a function of the deformation gradient $\mathbf{F}$.

The contribution of the local element Ω_e to the driving force residual follows as

$$\left.\frac{\partial E^{pot}}{\partial x_h(X_a)}\right|_{\Omega_e,local} = \int_{\Omega_e} (P \cdot \nabla_0 N_a(X))\, dV_0$$

where $P = \partial W/\partial F$ is the Piola-Kirchhoff stress tensor and the integral is taken in the undeformed space with all the functions in it being functions of undeformed variables.

2.3.4.2 Nonlocal Quasicontinuum Elements

For the non-local element Ω_e, the deformation inside cannot be represented by a homogeneous constant deformation gradient applied and we have to explicitly account for the positions of atoms. The positions of atoms are interpolated from the nodal atoms, but need to be incorporated into atomistic calculations of energy inside the element.

The contribution of the element Ω_e to the driving force residual becomes

$$\left.\frac{\partial E^{pot}}{\partial x_h(X_a)}\right|_{\Omega_e,non-local} = \sum_{atoms\ \ in\ \ \Omega_e} f(x_h(X))N_a(X),$$

where the sum is over all atoms in the elements with undeformed positions X and the term

$$f(x_h(X)) = \left.\frac{\partial E}{\partial x}\right|_{x=x_h}$$

is the actual force on the atom at $x_h(X)$.

2.3.4.3 Total Driving Force and Quadrature Rules

The total driving force becomes

$$\frac{\partial E^{pot}}{\partial x_h(X_a)} = \sum_{\Omega_e,local} \left.\frac{\partial E^{pot}}{\partial x_h(X_a)}\right|_{\Omega_e,local} + \sum_{\Omega_e,non-local} \left.\frac{\partial E^{pot}}{\partial x_h(X_a)}\right|_{\Omega_e,non-local} + \int_{B_0} GN_a dV_0 + \int_{\partial B_{02}} \tilde{T}N_a dS_0$$

Then for every quadrature atom in the element (where the fields are sampled for numerical integration) we calculate its total energy and derivatives using the appropriate model (from homogeneous local deformation gradient in the local case and from actual displacement of every neighbor atom in the non-local case). This provides a smooth transition from atomistics to continuum in this mesh with fast computation.

Concerning the quadrature rules used in local and non-local elements, to substitute an integral over the element with a sum in local case, just take one atom and multiply with the

volume of the element. We will treat the non-local case in more detail in the discussion of the 3-dimensional Quasicontinuum in the next section, which is closer to our implementation of complex lattice Quasicontinuum.

2.3.4.4 Local/Nonlocal Criteria

Local elements are computed very quickly, while there are only as many non-local elements as needed for high energy regions with any defects. Knowing the energy derivatives (driving forces in finite elements) and the second derivative (relating to stiffness matrix in finite elements) we can find the optimum configuration.

An important feature of Quasicontinuum theory is the adaptive mesh refinement. According to a specific problem the optimal mesh is selected. After the computation of the solution with an initial mesh, a certain criterion is used to refine or coarsen the mesh and to introduce or remove local and non-local elements. And then the solution is computed again. This repeats until the mesh chosen is optimal for the given problem.

The non-local elements are only needed close to defect cores and along slip planes. The decision on locality or non-locality of the element follows the criterion which is based on the second invariant of the Lagrangian strain tensor $\mathbf{E}$

$$\begin{aligned} II_E &= \frac{1}{2}\left[\mathbf{E}:\mathbf{E} - (tr\mathbf{E})^2\right] && (2.3)\\ &= E_{12}^2 + E_{13}^2 + E_{23}^2 - (E_{11}E_{22} + E_{22}E_{33} + E_{11}E_{33}), && (2.4)\\ & && (2.5) \end{aligned}$$

where

$$\mathbf{E} = \frac{1}{2}(\mathbf{F^T F} - \mathbf{I}).$$

An element is considered non-local when

$$\sqrt{|II_E|} > \epsilon \qquad (2.6)$$

where ϵ is a strain we can choose depending on the material and problem considered.

The elements which neighbor the non-local elements that share atoms with those elements should be considered as non-local as well. There are few more small details to the criterion, which try to reduce the number of non-local elements even further, for details see [2].

2.4 Three-Dimensional Fully Nonlocal Quasicontinuum Theory by Knap and Ortiz

The transition between local and non-local elements requires introduction of ghost forces on the border nodes. Quasicontinuum was also originally developed for two dimensional models, and could not simulate phenomena of truly three dimensional origin.

Knap and Ortiz in 2001 [6] further developed the Quasicontinuum theory, applying it to three dimensions and making it fully non-local. Thus the theory became more homogeneous, in the sense that each element can be treated similarly. It did not require introduction of ghost forces. It was also better suited for capturing defects, which might get lost in the local consideration of elements.

Nevertheless this further development of Quasicontinuum theory was computationally very fast and efficient.

They introduced many improvements to the theory. We would like to mention those and also very briefly go over the formulas involved since this is the background for our work.

The theory is fully non-local. Therefore the approach is to minimize the potential energy or to find a configuration in which the driving force is zero. The driving force becomes

$$\frac{\partial E^{pot}}{\partial x_h(X_a)} = \sum_{\Omega_e, non-local} \frac{\partial E^{pot}}{\partial x_h(X_a)}\bigg|_{e,non-local} + \int_{B_0} G N_a dV_0 + \int_{\partial B_{02}} \tilde{T} N_a dS_0 = 0$$

It is not difficult to deal with the integrals involving body force and traction. They can be calculated using the same quadrature rule as for the strain energy derivative term and added

to the driving force. Therefore we will skip these terms in future equations.

Consider

$$\frac{\partial E^{pot}}{\partial x_h(X_a)} = \sum_{\Omega_e, non-local} \frac{\partial E^{pot}}{\partial x_h(X_a)}\bigg|_{e,non-local} = \sum_{all\ \ atoms} f(x_h(X))N_a(X) = 0$$

Let us call

$$f_h(X_a(l_a)) = \sum_{all\ \ atoms} f(x_h(X))N_a(X)$$

the representative force on the node a. This force can be calculated using the quadrature rule, assigning every node a carefully calculated weight $n_h(l_a)$

$$f_h(l_a) \approx \sum_{nodes\ \ b} n_h(l_b) f(x_h(X_b))N_a(X_b) = 0$$

The development takes an unexpected turn, since the energy of the system computed this way is rank-deficient. A new quadrature rule has to be introduced, using different quadrature points. The authors use a cluster $C_h(b)$ around each node b as a quadrature point, see Figure (2.4), assigning a weight $n_h(b)$ to the entire cluster. This solves the problem of rank-deficiency, if the clusters are large enough.

The representative force becomes

$$f_h(l_a) \approx \sum_{nodes\ \ b} n_h(b) \left[\sum_{X \in C(b)} f(x_h(X))N_a(X) \right] = 0$$

These are the N equations for the N unknowns of nodal coordinates, which can be easily solved with a number of numerical solvers available.

Of course, the accuracy of this summation depends on cluster width. The authors determined that a single shell of neighbors will eliminate the rank-deficiency and after including the eighth shell of neighbors in the cluster, the solution is insensitive to further cluster size increases.

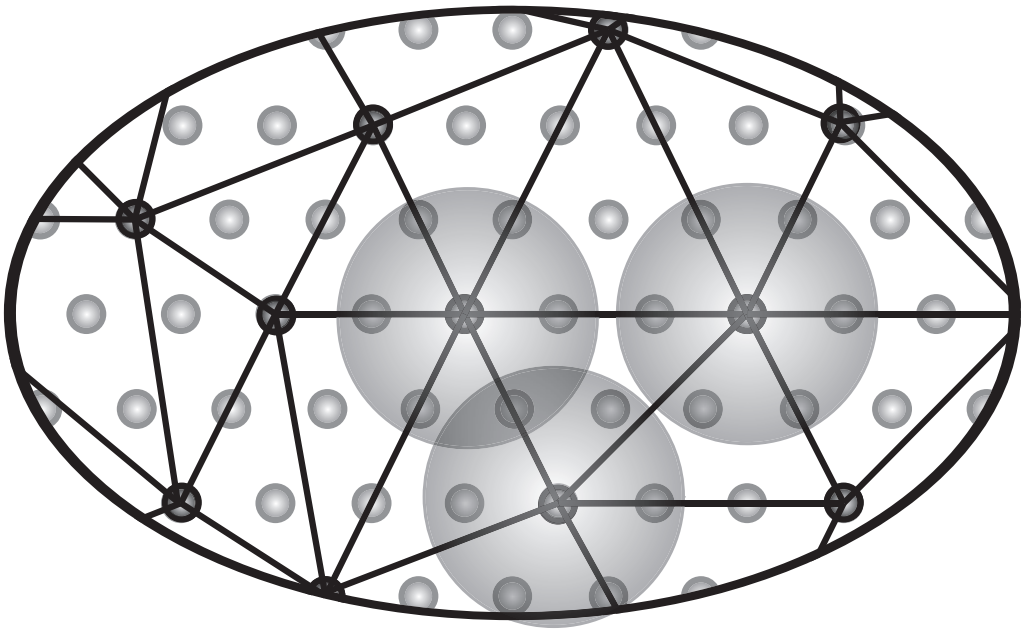

Figure 2.4: Clusters quadrature rule.

The authors investigate the accuracy and convergence characteristics of the newly proposed theory and calculate nano-indentation of a very large sample being able to follow the created and propagating dislocations.

Chapter 3

Complex Lattice Quasicontinuum

3.1 Challenges and Approaches

The reference [6] was the basis for our work and the program described in [6] was the starting point for our numerical development. Quasicontinuum allows a very good calculation of homogeneous lattices. But most crystals are "complex" in that they consist of many kinds of atoms. Most crystals have an ionic nature which automatically results in complex lattice structure (positive and negative charged ions - but the lattice has to be electrically neutral). This is the source of our motivation for developing Quasicontinuum to deal with heterogeneous or complex lattices.

One of the challenges in extending Quasicontinuum theory to complex lattices is that the theory developed previously assumes homogeneity. Another reason why Quasicontinuum is difficult to implement for complex lattices is that there is no scheme for computing the energy of the element or the cluster from a lattice which consists of many kinds of atoms. It is not possible to simply count the number of atoms to be represented. Another challenge is that Cauchy-Born rule is not valid for complex lattices, where shuffling becomes possible. The challenge is how to overcome the necessity of a homogeneity condition, as the base for interpolation and approximation.

Further, when developing the complex lattice Quasicontinuum theory, the numerical implementation must still account for the limited amount of computational memory and

time available.

For simplicity consider a crystal which consists of only two kinds of atoms. Let us call them type A and type B. One can consider it as two homogeneous Bravais lattices shifted with respect to each other, or as a Bravais lattice with a complex basis. This would be true for any number of atoms in a Bravais lattice with a complex basis.

The similarity to the homogeneous problem is that the crystal has still a periodic structure. Knowing the unit cell we can determine where all the non-deformed positions of other atoms are. This property definitely should be exploited. The difference with the homogeneous problem is that now the atoms are of different types. It is thus not immediately apparent how to interpolate atoms, how to build approximate energy and how to build representative forces. The properties of the node are dependent on whether it is an atom of type A or B.

It is possible to develop a local complex lattice Quasicontinuum[8, 9], since that would assume a uniform deformation inside one element. In this case a relation for the driving force can be derived based on the deformation gradient.

But in the non-local case this intuitive approach does not help, and maybe that is why a complex non-local Quasicontinuum theory has not been developed up to now.

One possible way is to consider the crystal as being a Bravais lattice with complex basis. Then every "site" of the crystal is the same as others and we can use interpolating and energy building schemes as in the homogeneous case, with some changes. The rule of computing the forces on so-called "sites" would be complex and require enormous computation. One of the additions we have to consider is that the so considered "site" would have internal degrees of freedom since, if the basis consists of one atom A and one atom B for example, these two atoms can move with respect to each other in each "site" differently. The number of internal degrees of freedom becomes large even with a relatively small complex basis order, resulting in enormous computational efforts.

We originally started developing complex Quasicontinuum based on this approach but

did not pursue it as we found a much simpler and faster approach.

As previously mentioned, there are a lot of challenges in developing a complex lattice Quasicontinuum. One of the challenges is to keep it simple (Ockham's Razor, see for example [85]) and computationally effective.

3.2 Newly Developed Complex Lattice Quasicontinuum Theory

Our approach was to consider a complex lattice as a union of simple Bravais lattices shifted with respect to each other. Each atom in the basis would define a sublattice. Sometimes it is possible to construct a Bravais lattice out of two or more atoms of the same kind in the basis, just a different sort of Bravais lattice. This does not by any means limit our theory. If we want to describe our theory in a few words, then our approach was to consider the sublattices as separate as possible making the theory and computational effort simpler, and reuse as much as possible the homogeneous lattice theory and the code.

In our example of two different atoms of kinds A and B, assume further that we can separate the material into just two Bravais sublattices, see Figure (3.1), to keep things simple. We will call the undeformed positions of the atoms $\mathbf{X}^A$ and $\mathbf{X}^B$, the deformed positions $\mathbf{x}^A$ and $\mathbf{x}^B$, the lattice coordinates $\mathbf{l^A}$ and $\mathbf{l^B}$, and the Bravais lattice vectors $\mathbf{a_i^A}$ and $\mathbf{a_i^B}$, $i = 1, 2, 3$ for sublattices A and B respectively. Since we again deal with Bravais lattices, the following relations hold

$$\mathbf{X}^A(\mathbf{l}) = \sum_{i=1}^{3} l_i^A \mathbf{a}_i^A$$

$$\mathbf{X}^B(\mathbf{l}) = \sum_{i=1}^{3} l_i^B \mathbf{a}_i^B$$

The potential energy E^{pot} depends upon the coordinates of all the atoms in the deformed

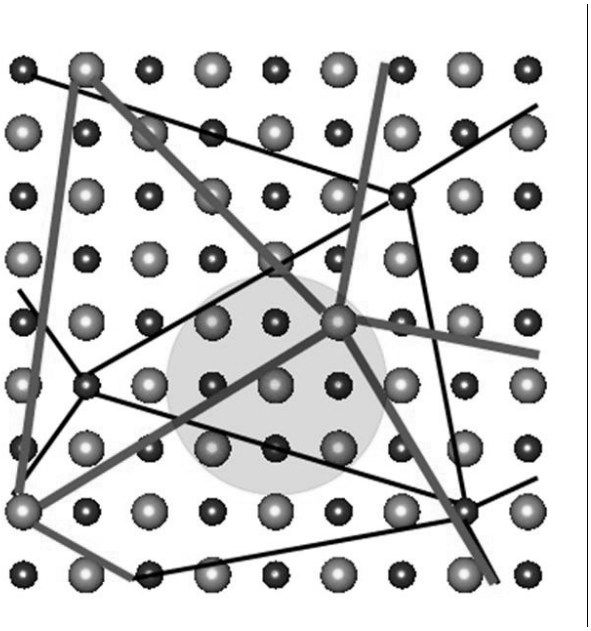

Figure 3.1: Complex Quasicontinuum of two sublattices.

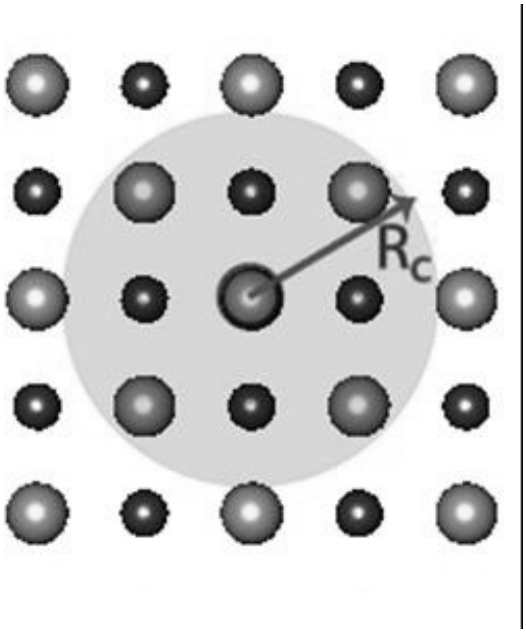

Figure 3.2: Cluster in complex Quasicontinuum of two sublattices.

configuration, all atoms in sublattice A and sublattice B.

$$E^{pot}(\{\mathbf{x}^A, \mathbf{x}^B\}) = E(\{\mathbf{x}^A, \mathbf{x}^B\}) + \Phi^{ext}(\{\mathbf{x}^A, \mathbf{x}^B)\},$$

where $\Phi^{ext}(\mathbf{x}^A, \mathbf{x}^B)$ is the work of external forces, which includes the work of body forces and traction forces and can be dealt with in the same way as the homogeneous case.

The potential energy has to be minimized with respect to all atoms coordinates to get an equilibrium configuration:

$$E^{pot}(\{\tilde{\mathbf{x}}^A, \tilde{\mathbf{x}}^B\}) = \min_{\{\mathbf{x}^A, \mathbf{x}^B\}} E^{pot}(\{\mathbf{x}^A, \mathbf{x}^B\})$$

Now we want to treat the sublattices as separately as possible. So we introduce separate triangulations of lattices A and B. Consider the sublattice A. Pick representative atoms in the sublattice A, which will become the nodes of the triangulation. The triangulation will define a shape function, which will operate on $\mathbf{X}^A$ domain. This is the normal shape function exactly as before for a pure homogeneous crystal, since it "sees" only the Bravais sublattice A. The same can be done for the B sublattice.

The deformed coordinates of the atoms can now be found as:

$$\mathbf{x}_h^A(\mathbf{X}^A) = \sum_{a,\ nodes} N_a^A(\mathbf{X}^A)\mathbf{x}_a^A(\mathbf{X}_a)$$

$$\mathbf{x}_h^B(\mathbf{X}^B) = \sum_{b,\ nodes} N_b^B(\mathbf{X}^B)\mathbf{x}_b^B(\mathbf{X}_b)$$

where a runs over all nodes in the triangulation L^A and b over L^B.

The so-constrained coordinates of the atoms are not independent variables of the problem any more. The energy minimization now runs only over representative atom coordinates,

which are independent coordinates.

$$E^{pot}(\{\tilde{\mathbf{x}_\mathbf{a}}^A, \tilde{\mathbf{x}_\mathbf{b}}^B\}) = \min_{\{\mathbf{x_a}^A, \mathbf{x_b}^B\}} E^{pot}(\{\mathbf{x_a}^A, \mathbf{x_b}^B\}) \tag{3.1}$$

Taking derivatives of this expression as before, we get the representative force on node $\mathbf{l}_a$:

$$\begin{aligned} \mathbf{f}_h(\mathbf{X}_a^A) &= \frac{\partial E^{pot}(\mathbf{x}_a^A, \mathbf{x}_b^B)}{\partial \mathbf{x}_a^A} \\ &= \sum_{all\ \ atoms} \left[\frac{\partial E^{pot}}{\partial \mathbf{x}_h^A} \frac{\partial \mathbf{x}_h^A}{\partial \mathbf{x}_a^A} + \frac{\partial E^{pot}}{\partial \mathbf{x}_h^B} \frac{\partial \mathbf{x}_h^B}{\partial \mathbf{x}_a^A} \right] \end{aligned} \tag{3.2}$$

The second term is zero because the positions of the atoms in sublattice B, $\mathbf{x}_h^B$, do not depend on the positions on the nodes in sublattice A, $\mathbf{x}_a^A$, per our construction of independent triangulations.

The representative force becomes

$$\begin{aligned} \mathbf{f}_h(\mathbf{X}_a^A) &= \sum_{all\ \ atoms} \left[\frac{\partial E^{pot}}{\partial \mathbf{x}_h^A} \frac{\partial \mathbf{x}_h^A}{\partial \mathbf{x}_a^A} \right] \\ &= \sum_{all\ \ atoms} \mathbf{f}(\mathbf{x}_h^A) N_a(\mathbf{X}^A) \end{aligned} \tag{3.3}$$

$$\begin{aligned} \mathbf{f}_h(\mathbf{X}_b^B) &= \sum_{all\ \ atoms} \left[\frac{\partial E^{pot}}{\partial \mathbf{x}_h^B} \frac{\partial \mathbf{x}_h^B}{\partial \mathbf{x}_b^B} \right] \\ &= \sum_{all\ \ atoms} \mathbf{f}(\mathbf{x}_h^B) N_b(\mathbf{X}^B) \end{aligned} \tag{3.4}$$

where $\mathbf{f}(\mathbf{x}_h^A)$ is the real atomistic force at atom at position $\mathbf{x}_h^A$. The same is true for the sublattice B. In order to find an equilibrium configuration consistent with the minimum potential energy we need to find a configuration where all the representative forces are zero.

Thus, we need to solve the following system of equations:

$$\begin{aligned} \mathbf{f}_h(\mathbf{X}_a^A) &= \sum_{all\ \ atoms} \mathbf{f}(\mathbf{x}_h^A) N_a(\mathbf{X}^A) = 0 \\ \mathbf{f}_h(\mathbf{X}_b^B) &= \sum_{all\ \ atoms} \mathbf{f}(\mathbf{x}_h^B) N_b(\mathbf{X}^B) = 0 \end{aligned} \tag{3.5}$$

Here we would like to mention a very important point. Looking at the form of equations (3.5), one can see that the lattices are still treated as independently as possible. For the representative force on node atom in lattice A we are required to take a sum over atoms in lattice A and determine for each such atom a force on itself and the shape function at it. The form is very similar to the homogeneous case. Importantly, the only difference is that the microscopic force on atom at x_A is the real microscopic force which depends on atoms around it of both type A and B. If any atom A or B would change its position, the energy of the system will also change and thus the representative forces.

This is how the lattices interact with each other, and how we get the system as whole. On the other side, we could separate A and B as much as possible. Separate triangulations make the theory and computation much easier.

There are a few other things to consider before the theory is complete. We are taking the full lattice sums here. We need a quadrature rule. If we use only node atoms as our quadrature points, it might again lead to an energy degeneration. What appropriate quadrature rule should we use?

We found it easy to use a cluster summation rule similar to the one in the homogeneous case. As before, we want simplicity and reuse of the previous theory. Therefore we take a cluster of atoms A around a node A as a quadrature point in L^A triangulation and the same for B nodes. Clusters are completely separate for different triangulations.

The quadrature weights of the clusters for the summation rule are computed separately for each sublattice and depend on the cluster size and the triangulation of the particular sublattice.

The effective forces become:

$$\begin{aligned} \mathbf{f}_h(\mathbf{X}_a^A) &\approx \sum_{all\ clusters\ s} n_s \left[\sum_{all\ atoms\ in\ cluster\ s} \mathbf{f}(\mathbf{x}_h^A) N_a(\mathbf{X}^A) \right] = 0 \\ \mathbf{f}_h(\mathbf{X}_b^B) &\approx \sum_{all\ clusters\ p} n_p \left[\sum_{all\ atoms\ in\ cluster\ p} \mathbf{f}(\mathbf{x}_h^B) N_b(\mathbf{X}^B) \right] = 0 \end{aligned} \tag{3.6}$$

After determining the equations, we need to find the solution, which will be the equilibrium configuration of the system. In the equilibrium configuration all the representative forces are zero.

We have a very effective model now for Quasicontinuum calculations. It is a very powerful and yet simple theory which can give many interesting new results.

All we need now is a rule relating the total energy of the crystal to the atomistic coordinates. The rule may be obtained from materials science or solid state physics (which obtain it from quantum mechanics calculation). It will be an input module for our theory.

The adaptive nodes selection feature of the homogeneous theory can be extended to work in the complex Quasicontinuum case as well. The nodes are selected based on the same criterion (2.6) as for the locality or nonlocality of the element. When the strain in the element exceeds some tolerance value, the element should be remeshed. The remeshing in this sense means that some extra nodes should be introduced which lie inside this element or on its surface and thus the size of this element should decrease. There are similar conditions as in the homogeneous Quasicontinuum implementation of Knap and Ortiz, but they must be applied to each Quasicontinuum sublattice independently.

A short overview of how the calculations work in complex Quasicontinuum is as follows. We need a potential dependent on atomistic coordinates as input. We triangulate, find clusters, and find weights for each sublattice. We determine the microscopic force on each atom in the cluster, depending on neighboring atoms in all sublattices. With some equation solver we determine the equlibrium position, which gives the minimum of energy, where

effective forces become zero.

Chapter 4

Numerical Implementation

4.1 Overview of the Changes Made to the Initial Program

As a basis for the numerical implementation of complex lattice Quasicontinuum, we used the program for the homogeneous Quasicontinuum by Knap and Ortiz as mentioned in [6]. This program, implemented in the C language [12], needed major structural change to allow for many instances of sublattices or Quasicontinua. On top of that many object oriented elements were introduced to the initial program. After changing the program itself, a complex Quasicontinuum program interface was designed and built in C++ [10, 11, 86]. The user of the program does not need to know any of the underlying functions of the newly designed C++/C program, the user needs only to specify material, underlying potential, lattice structure, size of the specimen and boundary conditions, and the tolerance parameter of the system.

New lattice types, materials and boundary conditions were introduced and tested in the program (allowing calculation with any number of building sublattices). Domain walls in different phases, boundaries, indentations, cracks and surface force relaxation can now be researched with the new program. All the new implementations were introduced to the program as interchangable modules, allowing with just one version of the program, with

small modifications, calculation of any of the above mentioned examples.

The initial program had as its center piece the main function, which relied on an extensive library of other functions. It called the functions to be performed one after the other. The user needed to keep track of all of those functions and the sequence in which to call them.

It is important to briefly review the main blocks of the initial program to understand the changes and extensions made. The procedure for the initial homogeneous Quasicontinuum main program was as follows:

a) Create an initial set of nodes - this constitutes part of the input to the program. The other input parameters are stored in the input file or are defined by preprocessor directives build into the code.

b) Initialize the structures to hold the instances on which to perform the simulation and store the results. The structures to be followed were initialized and used throughout the program: element list, node list, material, lattice type, shells of neighbors in the given Bravais lattice, etc.

c) Process the input, where the initial files are scanned for the data and parameters and the above-mentioned structures are filled.

d) Create a Delaunay triangulation [87] based on the initial set of nodes. It is an external module to the program, written in Fortran[88].

e) Create clusters for the quadrature rule and compute cluster weights from the consideration that the shape functions should be summed exactly by this cluster summation rule. By now all the structures necessary for calculation are set up.

f) Introduce a loop into the program which builds the core of quasistatic calculations and can be repeated as many times as desired. The load (for example the indentor load or crack opening load) changes creating the new set of boundary conditions. The solver, in this case conjugate gradient, finds the static equilibrium of the system with

the new boundary conditions and body forces. The results, the node positions, which include the interpolation positions of all atoms, the forces on the atoms and energy of the atoms, which include the information about the potential energy of the deformed body are computed and saved. As the next step, the system is remeshed due to the newly introduced deformation with the earlier mentioned adaptive nodes selection 2.6. The information holding structures have to be recalculated with the new adapted triangulation. The loop can be repeated again from beginning.

4.2 Quasicontinuum Class Design

The complex Quasicontinuum program takes care of which procedures to call and their mutual dependencies in different body deformation configurations. It summarized the inner parts of the simulations into the program, giving the user a simple way to control the running process.

A C++ class Quasicontinuum was introduced and builds the core of the new complex Quasicontinuum program. It includes the following members: lattice, element list, node list, indentor and material structures, inherited from the homogeneous program design. The new design introduced the following members as well: neighbor shell class, relative displacement to the absolute coordinate system vector, polarization vector, load step size, and names of the input and restart files. There are many more members which are help members to the design and implemented functions which are kept private. The reason some members were left as structures is for compatibility with the underlying C code. These structures were modified by adding constructors, destructors and some other functions as for example output functions when called from the C++ part of the code. This way the structures are classes, initialized properly from C++ code, and still behave like structures from C code providing compatibility [10].

A large number of functions to control the processing and representation of the simulation

were introduced as methods in the class Quasicontinuum. Just to mention some of them: compute solution, get polarization, compute forces and energy, increment loading, output results, many help functions to deal with coupling of Quasicontinua with each other to find the neighbors in the neighboring Quasicontinua to find their contribution to force and energy on the atom, remesh, print forces and energy, print mesh, print all atoms, change nodes positions, indent corner, shift tetragonal phase, shift rhombohedral phase, shift into domain wall initial position, load crack and many other functions which assist with the above functions and also control input and output, loading and processing.

The constructor in the Quasicontinuum class takes care of all the processes requiring initializing the data, reading input files, filling in the members and other preprocess data. All the above mentioned steps a) - e) corresponding to the homogeneous Quasicontinuum initializing are taken care of from user's side by just creating an instance of the Quasicontinuum class. In this case many changes have had to be made to the design and implementation of the complex Quasicontinuum code relative to the homogeneous Quasicontinuum code. Each instance initiated is part of the entire complex lattice and the code needs not only to be able to have many (as many as needed) similar instances but also to determine how this sublattice relates to the whole complex lattice and also to other Quasicontinuum sublattices. The implementation of these changes is discussed in more detail in the following section 4.5.

Let us mention some details of the simulation mechanism. To build an instance of the class a user needs to specify the following: a set of initial nodes for the triangulation with the material type (which will determine the potential type from the database to use), lattice type, relative displacement of the Quasicontinua with respect to each other, the maximal number of threads to use for multiprocessing, whether or not to use the restart file to start the computation from where the previous one stopped, the initial configuration the user wants to choose and whether it should be tetragonal or rhombohedral bulk phase or specific domain wall. The user of the program needs also to specify the loading and, if applicable, the indentor parameter and number of steps of the quasistatic loading and tolerance for

the solver and triangulation mesher. Then the user can specify different ways of output to process and present the data. For example, printing the atomistic displacement along specific line across the domain wall, a three dimensional polarization vector for the crack surface under loading, or a profile of atoms along specified region, forces and energies, finding and extracting dislocations, etc. The user can also determine what kind of data needs to be saved and whether or not the restart data for possible future rerunning of the simulation starting from the point stopped should be produced.

After creating instances of a Quasicontinuum class with the constructor, the user calls the compute function, where the complex lattice conjugate gradient is evolved and finishes upon finding an equilibrium configuration of the body in the given tolerance range. Other solvers can be implemented as interchangable modules as well, but conjugate gradient proved to be the best for this application because of its fast convergency and simplicity.

The next step is to process and save results. And here the user is provided with many helpful functions concerning how to represent results and save them. The results of the calculation include a huge amount of data. If the simulation included a sample consisting out of millions of atoms, the results of the computation will be 3 degrees of freedom for each atom, plus 3 dimensional force on each atom, plus its energy contribution to the total potential energy. The implemented functions allow fine control of the simulated process with chosen boundary conditions and body forces, and many functions which, immediately after receiving the calculated equilibrium condition, can process the results in any form suited.

4.3 Conjugate Gradient Class Design

The version of the solver method used is the preconditioned nonlinear conjugate gradient method with Secant and Polak-Ribiere, which is described in the reference [89]. Since the derivatives of the energy function are specified as analytical formulas in the program, the precision of the results is further enhanced. It results in a solution of a very large system

of non-linear equations keeping the non-linearity feature. Because the solver needs to have reading and modifying access to every one of the Quasicontinuum class instances, it was decided to implement it as a stand alone C++ class closely interacting with the underlying complex Quasicontinuum code.

The members of the class specified from the input are a set of Quasicontinuum instances, solution tolerance value and the maximum number of iterations performed if the solution has not yet been found. Many other private members are in the class which help with the conjugate gradient iterations.

The methods include, among others: compute forces, fill neighbor lists, destroy neighbor lists, update indentor, compute energy. These methods take the current configuration of all Quasicontinua together simultaneously and perform the needed operation on each of the Quasicontinua. The method update position sets the configuration in each Quasicontinuum as needed in the process of finding the solution. The main part of the class is constituted of the methods which perform the conjugate gradient iterations.

The most important function in the class is the compute solution function, which starts, governs and finishes the entire conjugate gradient solution. The user only needs to produce an instance of a Conjugate Gradient class with the constructor giving it a set of vectors of Quasicontinua to build the complex lattice and then call the Conjugate Gradient to solve the problem with the compute solution function. After the function finishes successfully, the instanced Quasicontinua will be in the equilibrium configuration.

We would like to mention here that the solver implementation is interchangeable. If another solver is looked upon, it can be implemented in very similar way from the outside interface. Then the user can specify which solver class should solve the given problem.

4.4 Mesh Generation

A new mesh generation technique, responsible for the initial set of representative atoms or nodes of the triangulation was designed. It serves as a good example of how the object oriented structure of C++ can compact and simplify things. The inheritance property of C++ was used. A purely virtual base class Mesh with the common functions for any set of nodes was designed. The class is called Mesh according to the generate mesh function of the homogeneous Quasicontinuum C code, but it generates only the nodes of the mesh for the input. A Delaunay mesh is generated based on these nodes as initialization part of the program later on.

The members of this class are the nodes array, output filename, material, lattice and other help members. The constructor, destructor, and the algorithm function which specifies which nodes to choose, are not implemented in this base class leaving it up to the derived classes. Obviously the algorithm which chooses the nodes depends on the specific problem. One method which is implemented is the output function, because once nodes are selected and specified they can be written in the standard form to a file which later constitutes the input to the main complex Quasicontinuum program.

This class is the parent class for specific meshes and can have many further derivations. Every other mesh is derived from this class. Every lattice type has to have its own algorithm to select the nodes. The mesh for indentation has atomistic resolution directly under the indenter, uniformly growing coarser and coarser in all three directions away from the indenter, for an example see Figure (4.1). The mesh for crack simulation for plain stress has atomistic resolution near crack tip, growing coarser in two dimensions away from the tip, for an example see Figure (4.2). The mesh for domain wall calculations has atomistic resolution at the domain wall becoming uniformly coarser away in one direction perpendicular to the wall plane, for an example see Figure (4.3).

The size of the atomistic region, the rate of becoming coarser in each direction, the

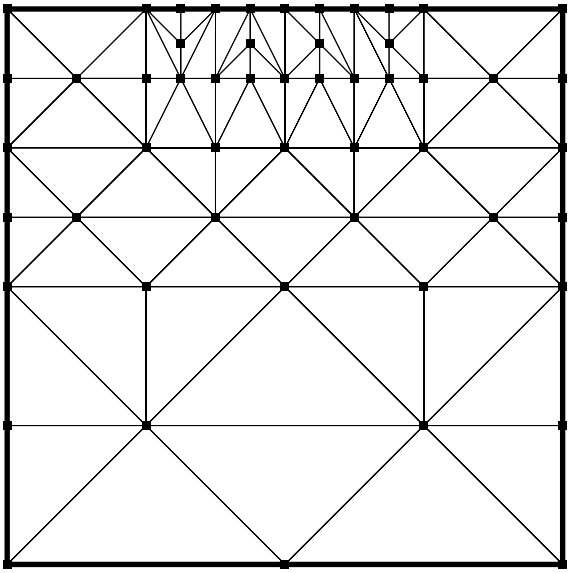

Figure 4.1: An example of indentation mesh.

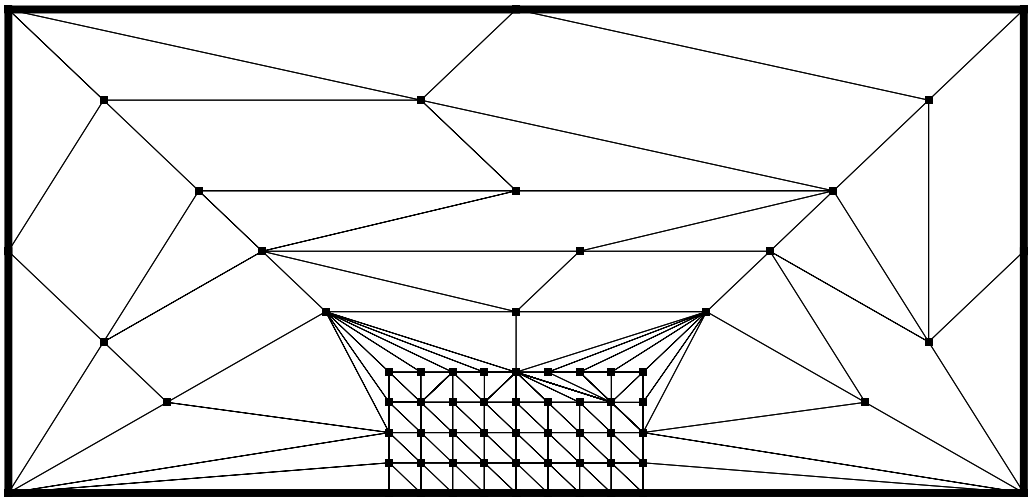

Figure 4.2: An example of crack mesh.

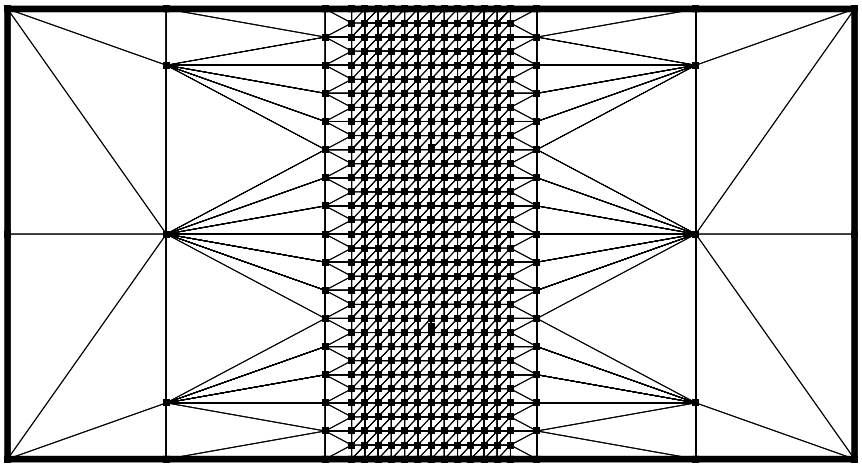

Figure 4.3: An example of domain wall mesh.

size and boundary conditions of the mesh are controlled by the program input parameters, which are also members of the specific derived class. The most challenging part of mesh generation is to find an algorithm which, depending on different lattice types, sizes and other parameters, produces a smooth mesh which is also not too fine and not too coarse.

4.5 Coupling of the Quasicontinua

There are two main aspects in coupling the underlying instances of Quasicontinua together. First, since every Quasicontinuum exists in its own coordinate system, we must bring the Quasicontinua together in the right way in the absolute coordinate system. The second important aspect is the actual implementation of the microscopic neighbors and forces of one particular Quasicontinuum taken among all its other Quasicontinuum neighbors.

From the way the code is designed and the performance and optimization goals, it is important that every Quasicontinuum instance, which represents a Quasicontinuum sublattice, includes the site with lattice coordinates $(0, 0, 0)$. Let us take a closer look at the reasons.

To define a lattice (different types of Bravais lattice) in a suitable way for computation, it is not always best to define three Bravais lattice vectors, see Figure (2.2), and a point of the lattice. Although such a lattice will be well defined because of the translational invariance of the Bravais lattice, it is not necessarily best to use in computational simulations. For example an fcc lattice can be represented more intrinsically if it is represented as a fcc cube rather than a parallelepiped, which is built by the three Bravais lattice vectors. In case of an fcc cube, an algorithm is necessary to determine which sites in the cube belong to the lattice. This is easier to do if the $(0,0,0)$ lattice is considered lattice occupied. Another reason lies in the calculations of the shells of neighbors. To build shells of neighbors, used for the calculations of clusters around each node and also for the calculations of each cluster site neighbors, it is important again that the $(0,0,0)$ site is occupied and is the center of the calculated shells of neighbors.

Therefore each sublattice has to have an atom at the origin in its own coordinate system. To make different Quasicontinua "live" in different coordinate spaces is no problem for the algorithm, since to the decoupling of the underlying Quasicontinua as described in previous chapter, the coordinate system of one Quasicontinuum can be completely independent of others for nodes, elements and even clusters around the nodes.

A parameter high in the implementation level is introduced to represent a relative displacement of each Quasicontinuum coordinate system to the absolute chosen coordinate system. One of the underlying Quasicontinua coordinate systems can be chosen as being absolute. Knowing these relative shifts, we can calculate the relative displacement of one Quasicontinuum with respect to another.

Another and probably most important challenge in coupling the Quasicontinua instances together in the complex Quasicontinuum code is to make sure that one Quasicontinuum "knows" its neighbors of the other Quasicontinua types at a particular site. Due to the design this information is required at the lowest level of the code implementation. The Quasicontinua exist separately as long as possible, the triangulations and the clusters are

being determined completely separately. The cluster which belongs to the a node in the Quasicontinuum A consists out of only A atoms. To numerically solve the equations (3.6), we need to determine the real smacroscopic force on each A atom in this cluster. And that is the first time when we need to know the real neighbors of each atom: in Quasicontinuum A, Quasicontinuum B, Quasicontinuum C, etc., in some radius. Knowing the neighbors of an atom in a sufficiently large radius will give a good approximation to the real microscopic force and energy of the atom in the examples we consider as mentioned earlier.

The way the implemention was made, all the neighbor lists of the Quasicontinua are calculated and filled in by the C++ part of the code which has access to all the Quasicontinua class instances. It uses a complicated but yet efficient algorithm to find the neighbors in the certain cutoff radius. The description of this neighbor finding algorithm is rather technical and would require an explanation of details of the underlying code, so is being left out here. When the C++ compute force function is being called by the C++ class conjugate gradient solver, the neighbors have been already computed and stored and can be efficently used for the force and energy calculations.

Due to the large number of functions which needed to be changed, due to the required C and C++ compatibility throughout the code, and due to the efficiency requirement on the code, the design and technical implementation of the force and energy calculations and neighbor search turned out to be a challenging task in the complex Quasicontinuum program.

4.6 Scaling of the Code

Let us consider scaling of the code with the number of Quasicontinua instances, and different values of other parameters, as a measure of computational efficiency of the designed algorithm and its implementation. There are two scalings to consider: computational runtime and the memory allocated by a run of the program.

Many computational efficiency features are similar to the homogeneous Quasicontinuum

program since we consider the Quasicontinua independently for the large part of the computation. This includes similar scaling of runtime and convergence with cluster size and lumping cutoff. In the complex Quasicontinuum case the runtime has to be multiplied by the number of Quasicontinua instances. Energy deficiency disappears as in the homogeneous case with just the nearest neighbor cluster for the quadrature summation.

Most of the runtime is spent calculating the forces on and energies of the atoms in the cluster and, if the atoms moved more than a tolerance parameter, recalculating the neighbors of these atoms. This scales with the number of Quasicontinua involved. If we consider a single Quasicontinuum then the force calculations should take the same order amount of time as in homogeneous case, because this scales with the number of neighbors. In the complex Quasicontinuum case, it can take slightly more time because of the need to access different neighbor lists for different neighbors and possibly having to call a different function to compute the analytical form of force and energy.

The required memory use of the program is much larger than for a single Quasicontinuum. This is easily understandable, because the instances of many Quasicontinua would require as many times more memory than a single one. Most of the memory is used by the neighbor lists of each of the cluster atoms. In the case of 10 Quasicontinua, as in simulating of a perovskite lattice, each such atom would have 10 lists of neighbors, formed from its own atoms and 9 other Quasicontinua atoms. If the cutoff radius is large as required, for example, for Coulombic iteration calculations, then these lists can take a large amount of computer memory.

Nevertheless, with a high degree of optimization many examples can be calculated easily using a personal computer. In the case where larger numbers of sublattice Quasicontinua are involved with large cutoff radiuses, a realistically large example can be calculated only by using a supercomputer, considering available memory and the speed of calculations.

4.7 Optimizations

Many optimizations were introduced into the code to make it more efficient. Since the goal of the algorithm and the implementation is to be able to calculate the largest possible samples, every optimization was vital to the performance. After all the optimizations, the performance of the code increased greatly, making it now close to the performance of the homogeneous Quasicontinuum code.

As mentioned before, the neighbor list setup and force and energy calculations take most of the running time of the program. It is important that nothing redundant is performed during it. Some nodes are fixed and are not allowed to move due to the selected boundary conditions. The calculation of the force on these nodes is not necessary and therefore the setup of neighbor lists is also not necessary. The complex Quasicontinuum program identifies which nodes to fill the neighbor lists for and which not. The program also identifies which nodes to compute the force on and on which can be skipped. The integrity of the program has been preserved with this optimization and thoroughly tested.

This optimization is especially helpful in the simulation of cases with large boundaries due to the sample size and the long reaching potential. This improved the performance of calculations in the ferroelectrics phenomena.

Another important optimization we would like to mention is the introduced force tolerance on each atom. As customary in molecular dynamics simulations, the calculated equilibrium configuration can still have a force on the atoms of some order of tolerance. Since many of the potentials which can be used in complex Quasicontinuum simulations come from molecular dynamics simulations, an algorithm has been introduced into the program which only relaxes the positions of the atoms when the force on them has not reached the tolerance range specified. This way the error introduced from molecular dynamics simulations does not pollute the computational space.

Many optimization features which were in the original homogeneous Quasicontinuum

code have been extended and implemented in the complex Quasicontinuum code. The following features we would like to mention here. The neighbor lists of the atoms in the cluster are being refilled only when the deformation around an atom has reached a specific tolerance value. This saves significant computational time. The element site cache, described in detail in [6], which keeps the assignments of particular sites to elements, is working in the complex version as well, making the computation run faster. Multithreading is working and is the single most important thing responsible for being able to calculate larger samples relatively fast.

Another very important feature which is working in the complex Quasicontinuum code is the adaptive remeshing algorithm, which gives us a backcoupling method, allowing for optimal use of computational resources.

Chapter 5

Potentials for Ferroelectrics

5.1 Goddard et al. Potential for $BaTiO_3$

A potential which has been extensively studied for this work is the polarizable reactive force field potential for Barium Titanate $BaTiO_3$ developed by Goddard, Zhang et al. ([26]) The potential takes its origin in the paper by Rappe and Goddard [90] and since then has been developed and applied to many different ionic systems. We consider here only the relevant $BaTiO_3$ potential, which has been kindly provided to us by Goddard group.

For a system of N atoms, a particular configuration is determined by the atom coordinates $\mathbf{r}_i$, $i = 1, \ldots, N$. Given the types of atoms, these are the only input for the model, which allows us to find the energy of the system.

The total energy E of the system consists of two terms:

$$E^{total}(\{\mathbf{r}_i\}) = E^{elec}(\{\mathbf{r}_i\}) + E^{vdW}(\{\mathbf{r}_i\}) + E^{corr}(\{\mathbf{r}_i\}) \tag{5.1}$$

where E^{elec} is the largest term, representing the contribution to the energy from all electrostatic interactions between the atoms. In this model the same atom core and shell interact electrostatically. Thereby the shells (S) and cores (C) of the atoms are considered separately, as gaussian charge distributions. E^{vdW} is the short ranged van der Waals energy. E^{corr} is the correction energy term which describes the interaction between the core and shell of the

same atom and is modeled by an anharmonic spring potential. We do not consider this term as discussed in section 7.1.2. Each term in the equation (5.1) represents a sum over pairwise interactions.

An important feature of this model which distinguishes it from other shell models is that the shell charges are variable. They are subject to the constraint that the sum of all shell charges is equal and opposite to the sum of all core charges, giving an overall neutral system. The relative displacements of the shells with respect to their cores are also variable. These displacements are small in general and give small corrections to the total energy.

E^{vdW} is the van der Waals interaction potential. It comes into play through the dipole moment between the atoms, induced dynamically in the shells. At large distances the induced dipole moment leads to an attractive fast decaying potential. At small distances between the atoms, the Pauli principle becomes relevant, leading to strong repulsion between the electrons and therefore the atoms. E^{vdW} also represents this repulsion. The force derived from the E^{vdW} potential is considered to act on the cores of the atoms.

The equilibrium of charges and displacements of the shells and cores (the variables of the problem) is achieved when the free enthalpy is minimized, or, equivalently, the chemical potential of all atoms becomes the same. The system is solved self-consistently using the conditions which arise from the Born-Oppenheimer rule. The Born-Oppenheimer rule states that the electrons (and thus the shells) will be always in configuration with the minimum potential energy with respect to the current core configuration.

The solution gives us the shell charges and core and shell displacements. Then we can calculate the forces as following:

$$\mathbf{F}_i^C = -\frac{\partial E^{total}}{\partial \mathbf{r}_i^C}$$

The force on the shells should be zero per the Born-Oppenheimer rule.

This potential accurately describes the atomic interaction and polarizability in $BaTiO_3$, equation of states, the cubic-tetragonal energy difference as a function of volume in a wide

pressure range, energy as a function of atomic displacements and cubic-tetragonal phase transition. The temperature of this transition, determined through molecular dynamic simulations with this potential, is found to be very close to the experimental value. Simulations with other potentials tend to give smaller than the experimental transition temperatures. This model can also correctly describe ab initio charge distributions, Born effective charges and dielectric properties of $BaTiO_3$.

5.1.1 Electrostatic Part of the Potential

Let Q_i^C, Q_i^S be the core and the shell charge of the atom i. The shell charges have to obey the constraint

$$\sum_{i=1}^{i=N} Q_i^S = Q^{total} = \sum_{i=1}^{i=N} Q_i^C$$

Let $\mathbf{r}_i^C$ and $\mathbf{r}_i^S$ be the coordinates of the core and the shell i, respectively.

Assume the charge distribution in core i

$$\rho_i^C(\mathbf{r}) = Q_i^n \cdot \delta(\mathbf{r} - \mathbf{r}_i^C) + (Q_i^C - Q_i^n) \left(\frac{\eta_i^C}{\pi}\right)^{3/2} \exp(-\eta_i^C \cdot |\mathbf{r} - \mathbf{r}_i^C|^2) \tag{5.2}$$

where Q_i^n counts for δ-function-like charge distribution (used mostly for small nuclei atoms) and η_i^C characterizes the width of the gaussian bell, taken from ab initio calculations. For the $BaTiO_3$ molecule all Q_i^n are set to zero.

Charge distribution in the shell i is

$$\rho_i^S(\mathbf{r}) = Q_i^S \left(\frac{\eta_i^S}{\pi}\right)^{3/2} \exp(-\eta_i^S \cdot |\mathbf{r} - \mathbf{r}_i^S|^2) \tag{5.3}$$

From the formulas (5.2) and (5.3) the electrostatic interaction between two different charge

Element	$\chi_i,\ [V]$	$J_i,\ [\frac{V}{e}]$	$Q_i^C,\ [e]$	$\frac{1}{2\sqrt{\eta_i^C}},\ [\mathring{A}]$	$\frac{1}{2\sqrt{\eta_i^S}},\ [\mathring{A}]$
Ba	-5.0992	12.7457	2	0.1632	0.8021
Ti	2.0369	11.3415	4	0.4255	0.5404
O	9.3877	15.9439	2	0.2618	0.4238

Table 5.1: Parameters of the electrostatic potential in Goddard et al. potential.

distributions i and j (core or shell, $i \neq j$) which are $\mathbf{r}_{ij}$ distance apart is

$$E^{elec,int}(\mathbf{r}_{ij}, Q_i^{C,S}, Q_j^{C,S}) = \frac{\mathrm{erf}\left(\sqrt{\frac{\eta_i \eta_j}{\eta_i+\eta_j}} \cdot |\mathbf{r}_{ij}|\right)}{|\mathbf{r}_{ij}|} Q_i^{C,S} Q_j^{C,S} \tag{5.4}$$

It represents a shielded Coulomb interaction.

The energy of the electrostatic interaction in the atom i itself is:

$$E^{elec,self}(Q_i^S, Q_i^C) = E_{i0} + \chi_i \cdot (Q_i^S + Q_i^C) + \frac{1}{2} J_i \cdot (Q_i^S + Q_i^C)^2$$

where $Q_i^S + Q_i^C$ is the charge of the atom ($Q_i^S < 0$), χ_i is electronegativity and J_i is the idempotential of the atom i. Both quantities depend only on the type of atom and are calculated as the rest of the parameters of this model from ab initio quantum mechanics calculations. The parameters for the electrostatic part of the potential are given in the Table 5.1. The energy term $E^{elec,self}$ implicitly includes shell or core self-interactions and their dependence on Q_i^S.

The complete electrostatic interaction E^{elec} consists of the sum of all $E^{elec,int}$ and $E^{elec,self}$.

5.1.2 Van der Waals Potential

The van der Waals interaction potential is described through different forms of potentials for interactions between different atoms. The Morse potential is used to describe the interaction

Atom	Atom	Potential	D, $[eV]$	A	R, $[\AA]$	P, $[\AA]$,	M
Oxygen	Oxygen	Morse	0.0905	7.1579	3.9975		
Titanium	Barium	Morse	0.9777	7.8754	3.3868		
Oxygen	Barium	Pauli				2.5841	6.2615
Oxygen	Titanium	Pauli				1.6163	8.4430

Table 5.2: Van der Waal potential parameters for Goddard et al. model.

between Oxygen-Oxygen and Titanium-Barium pairs

$$E^{Morse}(r_{ij}) = D\left(\left(\exp\left(\frac{1}{2}A(1-\frac{|\mathbf{r}_{ij}|}{R})\right)-1\right)^2-1\right) \tag{5.5}$$

where $\mathbf{r}_{ij}$ is the distance between the cores i and j.

For the pairs Oxygen-Titanium and Oxygen-Barium the interaction is modeled by the Pauli potential. It is a pure repulsion term in this model.

$$E^{Pauli}(r_{ij}) = (r_{ij}/P)^{-M}. \tag{5.6}$$

The parameters for the potential for the formulas (5.5) and (5.6) can be found in the Table 5.2.

5.2 Sepliarsky et al. Potential for $PbTiO_3$

Another shell model potential, which has been developed specifically for ferroelectrics, is the Sepliarsky, Cohen et al. potential ([28] and [91]). The version of this potential which has been designed for $PbTiO_3$ was used in this work. The Cohen group kindly provided us with the parameters of the potential.

As in the other shell potentials in this potential, each atom is split into two charged entities: a massive core and a massless shell. In this model the shell charges are not transferrable, they are fixed. This is an advantage for the Quasicontinuum implementation. The

core and the shell can move independently of each other. There are three components of the potential: Coulombic, short ranged and self potentials:

$$E^{total}(\{\mathbf{r}_i\}) = E^{Coulomb}(\{\mathbf{r}_i\}) + E^{ShortRange}(\{\mathbf{r}_i\}) + E^{Self}(\{\mathbf{r}_i\})$$

The parameters for this model have been carefully selected to reproduce DFT-LDA results for $PbTiO_3$. The model reproduces many of the features of the phonon dispersion curves [92], the effective charges, the behavior of the energy as function of the soft mode displacement, and the sequence of phases as a function of volume. The modeled behavior of $PbTiO_3$ with temperature is in qualitative agreement with experiment with a lower transition temperature than the experimental value.

5.2.1 Coulombic Potential

Both core and shell are represented by point charges. The energy contribution from two charged entities Q_i and Q_j located at the positions $\mathbf{r}_i$ and $\mathbf{r}_j$, respectively, becomes

$$E_{ij}^{Coulomb} = \frac{Q_1 Q_2}{|\mathbf{r}_i - \mathbf{r}_j|} \tag{5.7}$$

For typical distances between different atoms this representation is close to the Gaussian distributed representation from equation (5.4) with the typical values for η_i and $\mathbf{r}_{ij}$. It would be different for the same atom core and shell Coulombic interaction, but in the Sepliarsky et al. model the same atom core and shell do not interact electrostatically. This improves the stability of the entire structure, allows simple reversing of polarization and minimizing the energy of the structure independent on the direction of initially selected shifts. The shell and core charges selected in this model are given in the Table 5.3.

Atoms	Core Charges, [e]	Shell Charges, [e]
Pb	4.9580	-2.7850
Ti	8.8200	-5.1580
O	0.5630	-2.5080

Table 5.3: Coulombic charges in Sepliarsky et al. potential.

5.2.2 Short Range Potential

The non-electrostatic (commonly referred to as the short ranged) potential between atoms is considered to be applied at the shells of the atoms. This is a different approach than the Goddard et al. potential, but more common in the theories of shell models. The short range part of the potential is similar to the van der Waals part of the Goddard et al. potential.

Two different forms of short range interaction are considered. Most atoms interact through the Rydberg potential

$$\begin{aligned} E_{ij}^{Rydberg}(r) &= (A + Br)\exp(-\frac{r}{R}), \\ r &= |\mathbf{r}_i - \mathbf{r}_j| \end{aligned} \tag{5.8}$$

This includes pairwise interaction for the Lead-Titanium, Oxygen-Lead and Oxygen-Titanium pairs.

The Oxygen atoms interact through the Buckingham potential

$$\begin{aligned} E_{ij}^{Buckingham}(r) &= A\exp(-\frac{r}{R} + \frac{C}{r^6}), \\ r &= |\mathbf{r}_i - \mathbf{r}_j| \end{aligned} \tag{5.9}$$

The atoms of Lead and Titanium do not interact with the same species atoms.

The parameters for the formulas (5.8) and (5.9) can be found in the Table 5.4.

Atom	Atom	Potential	$A,\ [eV]$	$B,\ [eV/\mathring{A}]$	$C,\ [\mathring{A}^6 eV]$	$R,\ [\mathring{A}]$
Pb	Ti	Rydberg	0.096	-12.5665		2.420131
Pb	O	Rydberg	6766.270	127.7793		0.273805
Ti	O	Rydberg	1130.010	-160.8363		0.359723
O	O	Buckingham	3634.861		331.6058	0.314424

Table 5.4: Short range parameters in Sepliarsky et al. potential.

Atoms	$C_2,\ [eV/\mathring{A}^2]$	$C_4,\ [eV/\mathring{A}^4]$
Pb	119.48	17968.50
Ti	1428.59	36411.00
O	23.29	4514.70

Table 5.5: Self interaction parameters in Sepliarsky et al. potential.

5.2.3 Self Potential

There is a self energy interaction between the same atom core and shell, modeled by the anharmonic spring potential.

$$\begin{aligned} E_{ij}^{self}(r) &= C_2\frac{r^2}{2} + C_4\frac{r^4}{24}, \\ r &= |\mathbf{r}_i - \mathbf{r}_j|. \end{aligned} \tag{5.10}$$

Table 5.5 gives the values for the harmonic C_2 and anharmonic C_4 self coupling constants for the equation (5.10).

Chapter 6

Ewald and Wolf Summation Rules for Electrostatic Systems

6.1 Madelung Problem and Summation Rules

It is a well known problem in computations involving the Coulomb potential, that the pairwise r^{-1} Coulomb interaction summation is only conditionally converging. This means that this interaction is not only very long ranged, but also the result of the fact that the summation depends on the order the interaction pairwise terms are considered and summed. These facts make direct summation unhelpful and even impossible for numerical computation.

Many summation methods have been developed which, with some mathematical "tricks" and manipulations, allow for faster convergence of the Coulomb pairwise sum ([93], [29], [94], [95], [96], [97], [98], [99]).

The most famous of the summation algorithms, and the most widely used in molecular dynamics simulations, is the Ewald summation method [93]. In many cases this method gives good results, but it is computationally expensive and it induces an artificial periodicity on the considered system. Because of this, the method is not optimal for the examples considered in this work: large non-periodic systems with defects.

On the other hand Wolf's method of spherically truncated, pairwise r^{-1} summation [29] turned out to be of great help in our calculations with its fast convergence and ability to

perform near defects and interfaces.

This chapter is devoted to description and quick analysis of Wolf's method and its comparison with the well known Ewald method.

Let us consider a classic Madelung problem [100] of calculating the Coulomb potential of a charged system of N particles.

$$E = \frac{1}{2}\sum_{i=1}^{N}\sum_{i\neq i=1}^{N}\frac{Q_i Q_j}{r_{ij}}, \qquad r_{ij} = |\mathbf{r}_i - \mathbf{r}_j|, \tag{6.1}$$

where Q_i is the particle i charge located at the coordinate $\mathbf{r}_i$.

6.2 Ewald Summation Method

The Ewald method multiplies each term of the equation (6.1) by

$$1 = \mathrm{erfc}(\alpha r_{ij}) + \mathrm{erf}(\alpha r_{ij}) \tag{6.2}$$

Then the energy is split into two terms

$$E = \frac{1}{2}\sum_{i=1}^{N}\sum_{j\neq i=1}^{N}\sum_{\mathbf{n}=0}^{\infty}\frac{Q_i Q_j}{|\mathbf{r}_{ij}+\mathbf{n}|}\left[\mathrm{erfc}(\alpha|\mathbf{r}_{ij}+\mathbf{n}|) + \mathrm{erf}(\alpha|\mathbf{r}_{ij}+\mathbf{n}|)\right], \tag{6.3}$$

where $\mathbf{n} = (n_1, n_2, n_3)$ allows for summation over the entire lattice. After taking a Fourier transformation of the second term, we can write the summation as

$$E = E_{\mathbf{r}} + E_{\mathbf{k}}. \tag{6.4}$$

Introducing the charge structure factor $Q(\mathbf{k})$ as the square of the Fourier transform of

the charge density $\sigma(\mathbf{k})$

$$Q(\mathbf{k}) = \sigma(\mathbf{k})\sigma^*(\mathbf{k}) = \int\int d^3\mathbf{r}d^3\mathbf{r}'\sigma(\mathbf{r})\sigma(\mathbf{r}')\exp[i\mathbf{k}\cdot(\mathbf{r}-\mathbf{r}')]$$

we can present the term $E_\mathbf{k}$ in equation (6.4) as

$$\begin{aligned} E_\mathbf{k} &= \frac{2\pi}{3V}\left(\sum_{i=1}^{N} Q_i\mathbf{r}_i\right)^2 \\ &+ \frac{2\pi}{V}\sum_{\mathbf{k}\neq 0}^{\infty}\frac{\exp(-k^2/4\alpha^2)}{k^2}Q(\mathbf{k}) \end{aligned} \tag{6.5}$$

where V is the volume of the sample.

The two terms in equation (6.4) are fast converging: the term $E_\mathbf{r}$ in the real lattice space and the term $E_\mathbf{k}$ in the reciprocal lattice space. The computational efficiency of this algorithm is $O(N^2)$.

The main drawback of Ewald for our calculations is that it implies periodicity or it makes a system under consideration artificially periodic. This is not a problem for the small periodic systems considered in molecular dynamics simulations, but not for large aperiodic systems. If any defects are introduced to the system, for example an interface, the Ewald method has to be modified [95] making the method mathematically and computationally very complex.

6.3 Wolf Summation Method, Overview

There are some important physical observations which led to the development of the Wolf et al. [29] summation rule. First, there is solid theoretical and numerical evidence ([94], [101], [102]) that the effective Coulomb potential in fluids and solids is rather short ranged. Second, the non-convergence of pairwise direct sums in equation (6.1) in three dimensions [103] is mostly a consequence of totally charged systems as shells of neighbors over which summation is performed. Therefore the sum (6.1) has to be perfomed in a way which ensures

a neutrally charged environment for each ion.

These observations led to the development of the Wolf et al. method, which can be summarized as follows (for more detail see [29]).

a) The system to sum over should be neutrally charged to ensure fast convergence of the sum. Since the shells of neighbors of a certain cutoff radius r_c are almost never neutral, the charge contained inside the sphere should be neutralized. The neutralizing charge $-\delta Q_i(r_c)$ of the amount equal to the charge inside the sphere but the opposite sign should be considered located at the sphere surface at r_c. The energy contribution from the neutralizing charge becomes

$$E^{\text{neutr}}(r_c) = -\frac{1}{2}\sum_{i=1}^{N}\frac{Q_i \Delta Q_i(r_c)}{r_c}$$

$$\Delta Q_i(r_c) = \sum_{j=1, r_{ij}<r_c}^{N} Q_j$$

b) After some calculations, the expression for the total energy becomes equivalent to the pairwise summation of the shifted Coulomb potential plus self energy for each ion.

$$E(r_c) = \frac{1}{2}\sum_{i=1}^{N}\sum_{j\neq j(r_{ij}<r_c)} V^C_{\text{shift}}(r_{ij}) - \frac{1}{2r_c}\sum_{i=1}^{N} Q_i^2 \tag{6.6}$$

The shifted Coulomb potential is introduced as

$$V^C_{\text{shift}}(r_{ij}) = Q_i Q_j\left(\frac{1}{r_{ij}} - \frac{1}{r_c}\right) = \frac{Q_i Q_j}{r_{ij}} - \lim_{r_{ij}\to r_c}\frac{Q_i Q_j}{r_{ij}}$$

The Wolf summation rule may be stopped at the expression (6.6) by substituting the energy in (6.1) with the energy in (6.6). This gives good results in many applied problems.

c) The satisfactory cutoff radius r_c can be made even smaller and the convergence of the

method can be improved more especially near defects and interfaces by damping the Coulomb potential. The damping term is chosen to be $\mathrm{erfc}(\alpha r_{ij})$ with α as a damping parameter. This form allows for a close comparision with the Ewald formula. The final form for the Madelung energy becomes

$$E(r_c) = \frac{1}{2}\sum_{i=1}^{N}\sum_{j\neq j(r_{ij}<r_c)} V^C_{\mathrm{shift}}(r_{ij}) - E_{\mathrm{self}}, \tag{6.7}$$

where

$$V^C_{\mathrm{shift}}(r_{ij}) = \frac{Q_iQ_j\mathrm{erfc}(\alpha r_{ij})}{r_{ij}} - \lim_{r_{ij}\to r_c}\left\{\frac{Q_iQ_j\mathrm{erfc}(\alpha r_{ij})}{r_{ij}}\right\} \tag{6.8}$$

and

$$E_{\mathrm{self}} = \left(\frac{\mathrm{erfc}(\alpha r_c)}{2r_c} + \frac{\alpha}{\pi^{1/2}}\right)\sum_{i=1}^{N} Q_i^2$$

The authors of the paper [29] apply the method to NaCl, MgO crystals, MgO melt, free surfaces and symmetric tilts in MgO, and get excellent results. The calculated Madelung energy is very close to the energy calculated with more complex methods and can be made as close as needed to the exact value by adjusting the parameters of the model.

6.4 Calculation of Forces in Wolf's Method

The forces on the ions need to be calculated before taking the limit in equation (6.8). As the authors mention, the first derivative of $V^C_{\mathrm{shift}}(r_{ij})$, and hence the associated forces and stresses, are smoothly approaching zero at the cutoff radius r_c. Thus this type of truncation preserves the functional form of the original, unshifted pair potential and the forms of its derivatives.

The expression for the α component of the force on the ion i then becomes

$$\begin{aligned} F_{i\alpha}(r_c) &= -\frac{\partial E}{\partial r_{i\alpha}} \\ &= -\sum_{j\neq i(r_{ij}<r_c)} \frac{dV^C_{\text{shift}}(r_{ij})}{dr_{ij}} \frac{r_i j\alpha}{r_{ij}} = \sum_{j\neq i(r_{ij}<r_c)} f_{ij\alpha}, \end{aligned} \tag{6.9}$$

where

$$\begin{aligned} f_{ij\alpha} &= \sum_{j\neq i(r_{ij}<r_c)} Q_i Q_j \left\{ \left(\frac{\text{erfc}(\alpha r_{ij})}{r_{ij}^2} + \frac{2\alpha}{\pi^{1/2}} \frac{\exp(-\alpha^2 r_{ij}^2)}{r_{ij}} \right) \frac{r_{ij\alpha}}{r_{ij}} \right. \\ &- \left. \left(\frac{\text{erfc}(\alpha r_c)}{r_c^2} + \frac{2\alpha}{\pi^{1/2}} \frac{\exp(-\alpha^2 r_c^2)}{r_c} \right) \frac{r_{ij\alpha}}{r_c}\bigg|_{r_{ij}=r_c} \right\} \end{aligned} \tag{6.10}$$

6.5 Convergence and Error Analysis of Wolf's method

After some calculations, one can show that the Madelung energies per ion of charged and charge-neutralized systems are given by

$$\begin{aligned} \frac{E_{\text{charged}}(r_c)}{N} &= \frac{E_{\text{Madelung}}(r_c \to \infty)}{N} \\ &- \frac{2}{\pi N} \int_0^\infty dk [Q(\mathbf{k}) - 1] \cdot \cos(k r_c), \end{aligned} \tag{6.11}$$

$$\begin{aligned} \frac{E_{\text{charge-neutralized}}(r_c)}{N} &= \frac{E_{\text{Madelung}}(r_c \to \infty)}{N} \\ &- \frac{2}{\pi N r_c} \int_0^\infty dk Q(\mathbf{k}) \cdot \frac{\sin(k r_c)}{k}. \end{aligned} \tag{6.12}$$

Both energies oscillate about the true Madelung energy. But if the energy of the charged system is not necessary convergent with $r_c \to \infty$, the energy of the charge-neutralized system converges at least as r_c^{-1}.

This analysis has been done without considering damping of the Coulomb potential. Considering damping after some complex calculations, it can be shown that the Madelung

energy in Wolf's summation converges to the true value as r_c^{-3}.

6.6 Wolf and Ewald Comparison

If we add and subtract a self term corresponding to $\mathbf{n} = 0$ to the Ewald sum, we can split the direct and reciprocal lattice sums as follows

$$\begin{aligned} E_{\mathbf{r}} &= \frac{1}{2}\sum_{i=1}^{N}\sum_{j\neq i=1}^{N}\sum_{\mathbf{n}=0}^{\infty}\frac{Q_iQ_j\mathrm{erfc}(\alpha|\mathbf{r}_{ij}+\mathbf{n}|)}{|\mathbf{r}_{ij}+\mathbf{n}|} \qquad (6.13)\\ &- \frac{\alpha}{\pi^{1/2}}\sum_{i=1}^{N}Q_i^2, \\ E_{\mathbf{k}} &= \frac{1}{2}\sum_{i=1}^{N}\sum_{j=1}^{N}\sum_{\mathbf{n}=0}^{\infty}\frac{Q_iQ_j\mathrm{erf}(\alpha|\mathbf{r}_{ij}+\mathbf{n}|)}{|\mathbf{r}_{ij}+\mathbf{n}|} \qquad (6.14) \end{aligned}$$

the term $E_{\mathbf{k}}$ will represent only a small correction to the term $E_{\mathbf{r}}$.

In the limit of $r_c \to \infty$ $E_{\mathbf{k}}$ in equation (6.14) is the limit of (6.7), the energy calculated with Wolf's method. The reciprocal part of the Ewald energy in equation (6.14) is what is being left out in Wolf summation. As $r_c \to \infty$, this is the error that Wolf's summation is introducing. This error increases with increasing damping α and becomes zero in the undamped Wolf method.

The authors analyze the error term analytically and numerically and suggest that $\alpha \leq 1.5/a$, where a is a lattice constant, gives a very small error. The necessary cutoff radius becomes smaller with larger α and for $\alpha = 1.5/a$ already $r_c = 1.5a$ accurately determines the Madelung energy.

Another difference between Ewald and Wolf summation rules is that the Ewald method implies periodicity of the system, Wolf does not. Also important, the Ewald sum is unshifted, i.e., not neutralized, but Wolf is neutralized.

Chapter 7

Study of 180 Degree Domain Wall in $BaTiO_3$ Performed Using Goddard et al. Potential

7.1 Setup of the Problem

7.1.1 $BaTiO_3$ and Its Properties

Barium Titanate $BaTiO_3$ is the most widely researched ferroelectric. The main reason for this is that it is a common lead-free ferroelectric which is in a stable tetragonal phase at room temperature and that it also has a simple crystallographic structure for theoretical investigations. It was the first perovskites discovered [104]. A good overview of the properties of $BaTiO_3$ can be found in [105] and [7].

$BaTiO_3$ is very widely used in electromechanical actuators, sensor applications, capacitor dielectrics, in photo-galvanic devices, as a photo-refractive material, and in memory devices [7], [106], [107], [108], [109], [110], [13].

Barium Titanate has been extensively studied theoretically and experimentally since the discovery of its ferroelectric properties, yet there are still many questions unanswered and for many years in debate. For theoretical investigations much research has been on phenomenological continuum scale using the Landau-Ginzburg model which started in the papers of Devonshire [111] and [112].

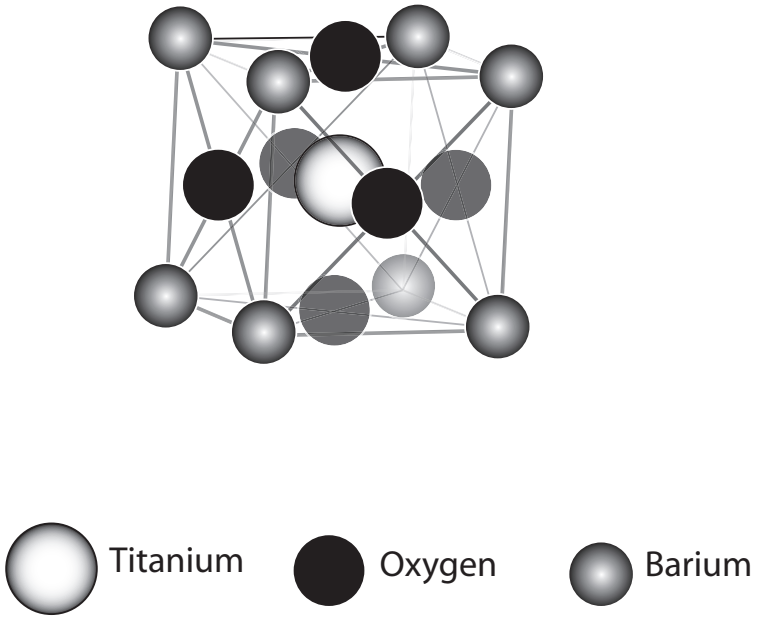

Figure 7.1: $BaTiO_3$ unit cell.

$BaTiO_3$ has a perovskite structure with a commonly chosen unit cell having one Titanium atom in the center, four Barium atoms in the corners and six Oxygen atoms at the center of the faces [113]. It is an fcc derived structure, geometrically considered the unit cell is a cube which then gets distorted depending on the surrounding temperature and pressure. A $BaTiO_3$ unit cell is shown in the picture 7.1. Above the Curie Temperature, $T = 393K$ Barium Titanate is paraelectric and does not exhibit spontaneous or permanent polarization. The material has a cubic unit cell structure and is in cubic non-ferroelectic phase.

At $T = 393K$ and below this temperature under normal pressure Barium Titanate becomes ferroelectric - it shows spontaneous and permanent polarization. Lowering the temperature, $BaTiO_3$ enters different phases: from cubic phase to tetragonal, from tetragonal to orthorhombic, from orthorhombic to rhombohedral. All these material phases are ferroelectric phases.

The transition from cubic to tetragonal phase happens at $T = 393K$. The crystal in tetragonal state can exhibit six polarization directions, equivalent to $< 100 >$. At $T = 278K$ Barium Titanate switches into orthorhombic phase with twelve different polarization direc-

tions, equivalent to $< 110 >$. Finally at $T = 183K$ and below the crystal is in rhombohedral phase with eight polarization directions equivalent to $< 111 >$ [114], [7]. The unit cell, see the Figure 7.1, is distorted along the polarization direction, but the shifts are so small that the Figure 7.1 would not change much to the naked eye.

We are primarily interested in the tetragonal phase of $BaTiO_3$ as this is the phase it attains at room temperature. Two kinds of domain walls are possible in this phase: 90^0 and 180^0 walls [115], [114].

7.1.2 Notes on the Potential

The potential by Goddard et al., described in the section 5.1, was used for the investigations in this chapter. This potential has been primarily designed for molecular dynamics simulations where symmetries of the problem could be easily introduced and made part of the simulation. Therefore, the potential exhibits stable behavior with imposed symmetries, as for example a rhombohedral symmetry when rhombohedral phase is considered. But the potential is not locally stable without any imposed symmetries, when three degrees of freedom of all the atoms minus translational and rotational degrees of the entire specimen are considered. It does not necessary present a problem in molecular dynamics simulations, but it is not optimal for our calculations. We want to research a truly realistic sample with realistic boundary conditions without introducing any unnecessary symmetries or periodicity into the considered problem.

The solution for us in this case was to slightly modify the potential to make it locally stable for many degrees of freedom (when waiving the symmetry) or at least stable in the degrees of freedom in the considered examples. We found a desired version of the potential by considering the movements of cores and shells as one entity. This eliminated the very high magnitude Columbic force between same shell and core, which made it numerically difficult to deal with the potential, and also made the potential stable in the space of the available degrees of freedom in the examples considered. Otherwise the parameters of the potential

and lattice constants were kept the same.

The permanent spontaneous polarization in a Barium Titanate specimen is still available, since the atoms themselves become ions and their sublattices can shift with respect to each other creating a polarization moment. The sum of the core and shell charges of one atom is not neutral due to the parameters used in the potential, where the electron charge is considered to be distributed among all atoms.

Polarization in the tetragonal phase of the original Goddard et al. potential is $-0.94e\mathring{A}$, the same potential without consideration of shell core displacement gives the polarization of $-0.61e\mathring{A}$. After equilibration of the bulk tetragonal phase for the constrained potential, the polarization becomes $-1.21e\mathring{A}$. Thus our potential overestimates the bulk polarization by $-0.27e\mathring{A}$, which corresponds to 22% of its value.

This modification allows the potential in the bulk tetragonal phase to become stable for many degrees of freedom of atomic movement. The potential becomes stable for the necessary degrees of freedom in the examples considered: for the 180 degree wall example, any movements of all atoms in the polarization direction; and for the crack example, any movement of all atoms in the polarization direction and perpendicular to the crack.

We would like to note that the Goddard et al. potential is already an approximation to quantum mechanics calculations. Charges and core shell shifts change so much in different shell models for $BaTiO_3$ (compare for example [27] and [116]), even in the different versions of the same models, that it seems that the actual charges and shifts in models can be changed substantially to fit quantum mechanics calculations.

7.1.3 Implementation of $BaTiO_3$ in Complex Lattice Quasicontinuum Theory

The $BaTiO_3$ is modeled by five sublattices Ba, Ti, Ox, Oy, Oz. Each of the sublattices has a simple cubic (or tetragonal in tetragonal phase) structure. A decomposition of the unit

cell is shown in the Figure 7.2 in perspective.

It would have been possible to separate the unit cell into four Bravais lattices, taking any two out of three of the Oxygens in the unit cell to build one Bravais lattice. That would require introducing an extra lattice type into the program with the consequence of writing extra functions for the lattice and shell handling. To minimize computational effort and also to keep a simpler concept, we decided on splitting the $BaTiO_3$ unit cell into five sublattices. This gives us five separate Quasicontinua instances in the program which interact through microscopic forces.

A new lattice type and a new potential type were introduced to the program. The appropriate functions and extensions of the existing functions were introduced throughout the program.

7.1.4 Equilibration of the Potential

Having modified the potential, the equilibrium bulk tetragonal phase needed to be found. We used the conjugate gradient method within the Quasicontinuum program to find a bulk configuration with the minimal potential energy or zero forces on all the atoms.

A relatively small sample, sufficient to justify a bulk assumption in the middle of it, was introduced. The atoms in the sample are interacting with the potential the energy of which needs to be minimized. The sample was allowed to relax under the action of the forces, with conditions such that the shifts of the atoms can be simultaneously minimized. It is quite possible to minimize the lattice constants with the same approach, but the lattice constants were left the same as in the original core shell displaced configuration to assure the maximum compatibility.

The stable bulk tetragonal configuration was found after few iterations. Its stability was justified in the following tests. One of the atomic coordinates was perturbed in a small positive or negative amount and the entire system was allowed to relax. The system converged into the original initial configuration in each test, proving the stability of the local

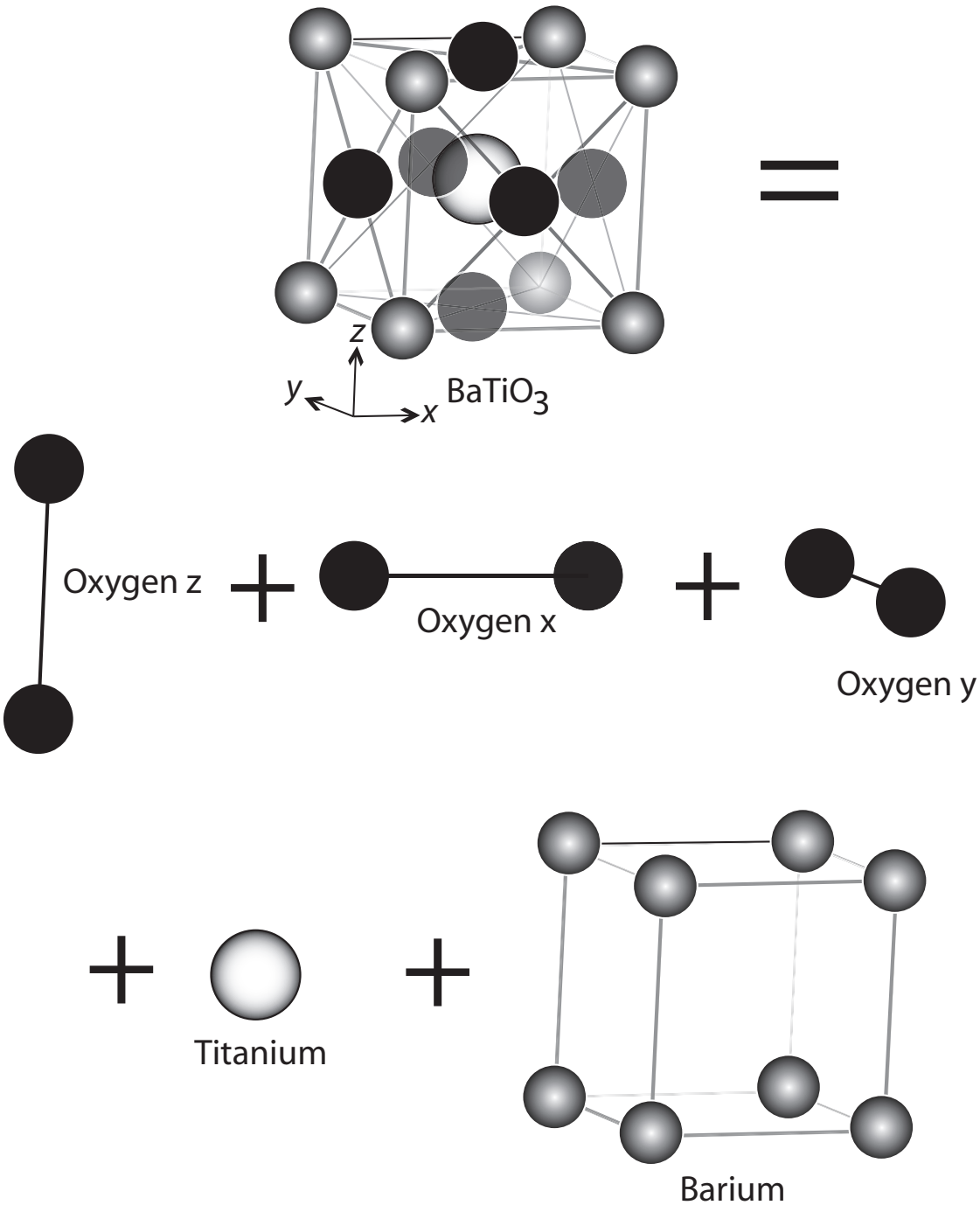

Figure 7.2: $BaTiO_3$ unit cell decomposition into 5 sublattices.

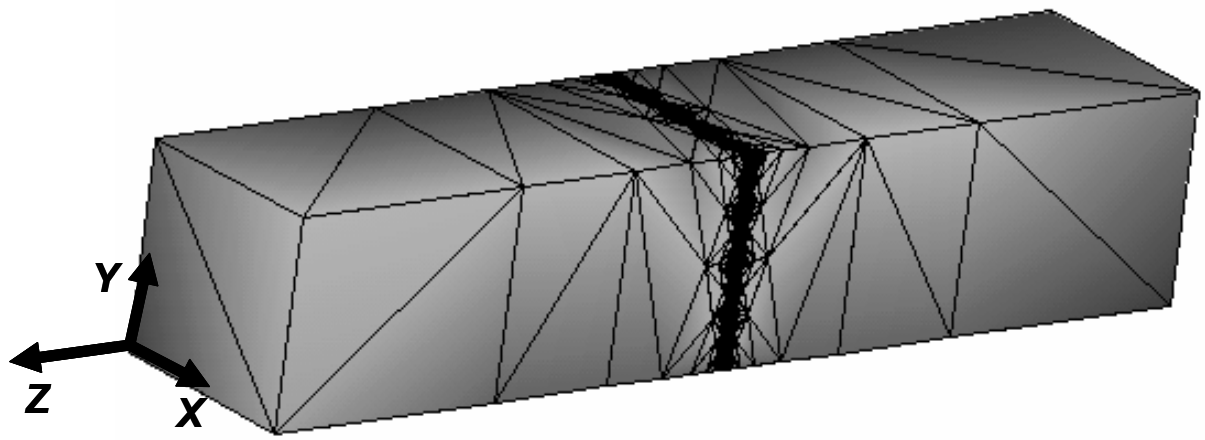

Figure 7.3: Mesh for the 180 degree domain in $BaTiO_3$ wall calculations.

minima found.

The Wolf's summation described in Chapter 6 without damping was used for evaluation of the electrostatic part of atomic energies and forces. Tests performed on Wolf's summation verified the use of this summation method and determined the sufficient cutoff radius for the summation of the electrostatic interaction. The energy and force values summed with the cutoff radius of $12\mathring{A}$ and larger differed from the limit values by less than 0.01%. The $12\mathring{A}$ length corresponds to about three lengths of the unit cell. We researched the behavior of the summation around this cutoff radius number and found smooth behavior not affected by the border of the third unit cell. Thus we decided to choose this value for the setup of the domain wall calculations, as it is convenient to have this value as a multiple of a unit cell length, as will be clear below.

7.1.5 Initial Triangulation and Positions of Atoms

The sample is in tetragonal phase with non-periodic boundary conditions. The size is 65 unit cells in X direction, 65 unit cells in Y direction and 513 unit cells in Z direction, see the Figure 7.3.

The wall is in $Z = 0$ plane, perpendicular to the Z axis. The atoms on the right side of the wall, i.e., $Z > 0$ are in the pure tetragonal domain with positive polarization, and on the left side of the wall, i.e., $Z < 0$ are in the domain with negative polarization. The polarization is along X direction. This builds the 180 degree domain wall between the domains. This is a domain wall with no net polarization on the domain wall surface, which has lower energy than a domain wall with net charge, and which is also most observed in the experiments ([117], [118], [119], [120], [121]).

We also choose to model only the Barium centered wall as it is the wall which has the lower energy than Titanium centered wall and is stable ([36], [119]). There have been some studies about the energies of domain walls and we will compare them with the energy values calculated with complex Quasicontinuum theory.

The resolution at the wall is atomistic where the nine unit cells adjacent to the wall are considered atomistically. The fine atomistic resolution at the wall smoothly gradates to coarser and coarser resolution further away from the wall. The smoothness of the final results and the calculated atomistically small thickness of the wall justifies the selected size of the atomistic region and the selected initial triangulation.

As previously mentioned, the energies and forces calculated with Wolf's summation rule, attain their true value (with small error) at the cutoff radius of $12\mathring{A}$ or approximately the length of three unit cells. Therefore every atom at least three unit cells deep from the surface of the specimen will not feel the existence of the boundary near it. The outer three unit cells will feel the boundary effects and therefore need to be fixed during the calculations to ensure the proper boundary conditions. The outer cells need to be fixed in the position corresponding to the equilibrium polarization, positive polarization on the right side ($Z > 0$), negative polarization on the left side ($Z < 0$). Thus the atoms inside the specimen will behave as they were embedded in the bulk homogeneous infinitely large polarization domain, but different domains on each side of the domain wall.

The initial positions of the atoms correspond to a homogeneous tetragonal phase equilib-

rium polarization which abruptly changes signs at $Z = 0$. This corresponds to an infinitely sharp domain wall. The atoms at the wall itself, at $Z = 0$, which correspond to Barium and Oxygen Oz Quasicontinua, are not shifted into up or down polarization.

All of the atoms inside the specimen (inside the surface layer) are allowed to move in the X direction, parallel to the polarization, in order to find the equilibrium configuration with given boundary conditions on the surface layer. Thus the equilibrium found will be the equilibrium 180 degree domain wall configuration. It will be surrounded on both sides of the wall with large domains with no periodicity involved. These are much more realistic conditions than previously researched in other molecular dynamic simulation works.

7.2 Results

The results of the study are the equilibrium configuration of 10,837,125 atoms constituting two large domains of opposite polarization with a wall between them. This three-dimensional result needs to be presented in a simpler form to be clearly understood. In the following we will extract the needed information and research the physical aspects of the domain wall and also complex Quasicontinuum theory performance.

The number above is the total number of atoms in the sample, with most of the atoms positions interpolated with the Quasicontinuum mechanism. The actual number of atoms which is followed by the solver is much smaller, approximately 190,000.

7.2.1 Atomic Coordinates Profile

As a first step, we will plot atomic profiles, i.e., coordinates of atoms on a line perpendicular to the wall. Since the coordinates of the atoms shift to form a polarization, the profiles give us a good idea of how fast the polarization is switching at the wall. The polarization is in X direction, the wall is in $Z = 0$ plane perpendicular to the Z axis. Therefore the X coordinates of the atoms versus their Z coordinates are plotted in Figure 7.4. The coordinates are in

units of Angstroms. The unit cell selected is in the middle of the considered specimen, with the lattice coordinates $l_1 = 0$ and $l_2 = 0$. These atoms are the least affected by the presence of boundaries (we will later study the validity of the bulk assumption in the considered simulation).

Far away from the wall the shifts of the atoms with respect to a non-polarized tetragonal state are equal in magnitude and opposite in sign at the two ends. This builds the opposite polarization domains at the two sides of the specimen divided by the wall. The switch of the displacement happens very rapidly, but the presence of the wall has a long ranging effect, the "tail" of the polarization change is long and flattens out slowly further away from the wall.

The results are smooth going through the different resolutions of the mesh, which justifies the selected resolution of the triangulation.

The profiles of the Barium and Titanium atoms peak in the same direction before switching into opposite direction, a property which cannot be seen in small samples, as those samples do not allocate enough space for such phenomena.

Figure 7.5 is a zoomed view of the wall using the coordinate profiles of Figure 7.4. Here we can determine more clearly that most of the polarization switching occurs in the 2-3 unit cells adjacent to the wall (on one side). This makes the thickness of the wall approximately 4-6 unit cells, which is 1.5-2.5 nm.

These values lie within the upper limits of the wall thickness found by experimental measurements, see [31] and [30]. In the experiments by [31] an upper bound of 5 nm was found, where in the experiments by [30] the smallest domain wall measured was 8 nm wide. It should be noted that it remains difficult to resolve experimentally 180 degree walls at the level of atomistics. Only recently, progress was made with 90 degree domain walls in $BaTiO_3$ and $PbTiO_3$ ([122], [123], [124]) which exhibit an easier target to measure.

Our values are in very good agreement with continuum simulations based on the Landau-Ginzburg theory [33] which estimate the thickness to be 0.5-2 nm. There is also good

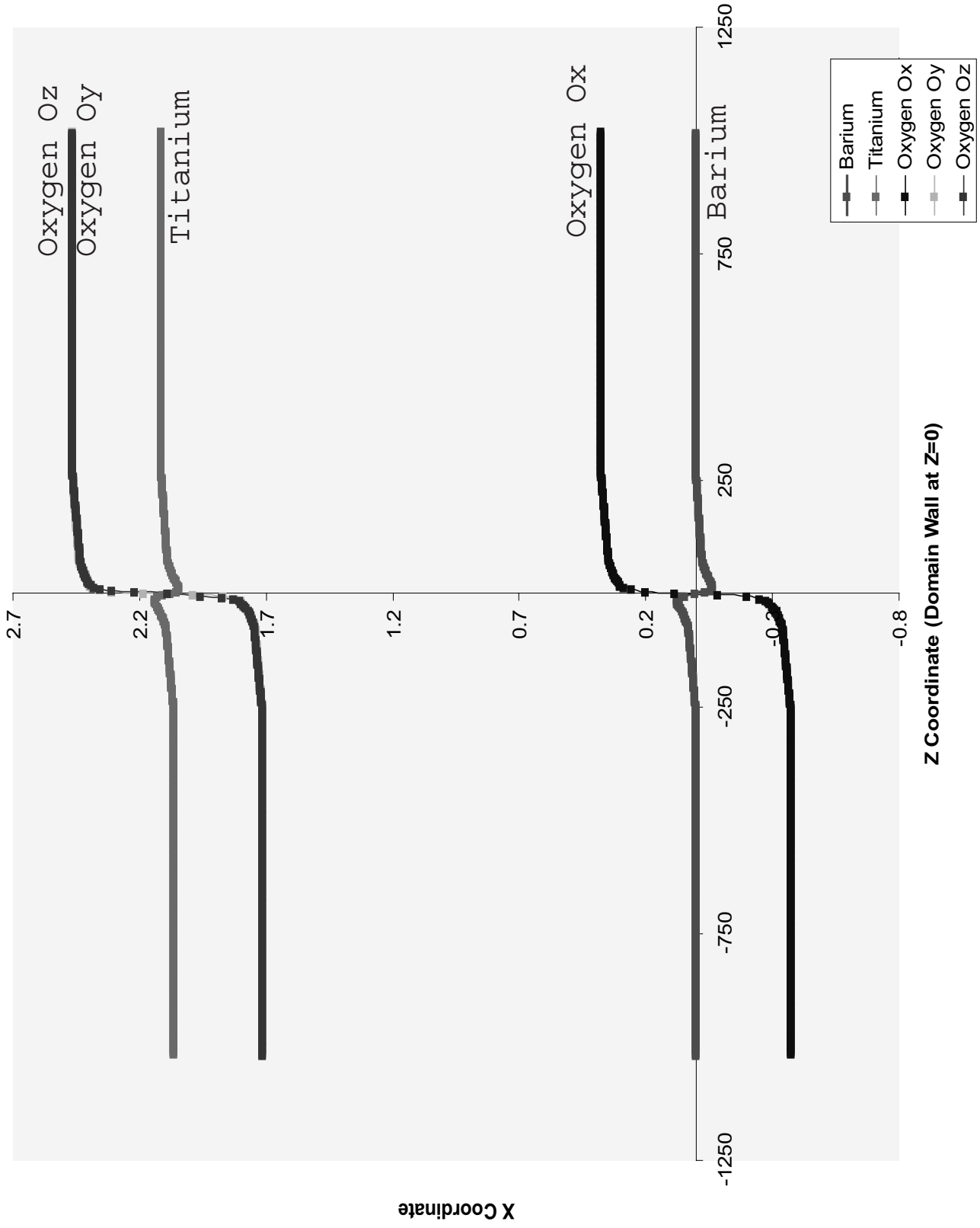

Figure 7.4: Profiles of atoms across the domain wall.

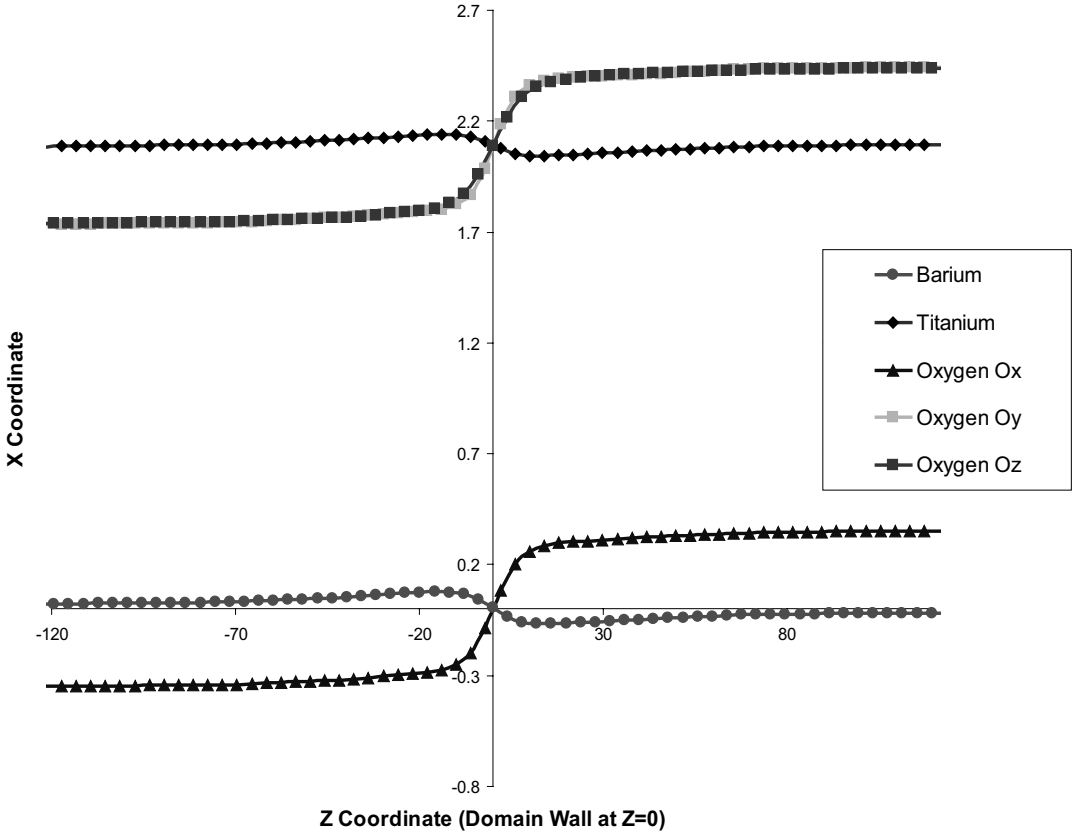

Figure 7.5: Coordinate of atoms closer to the domain wall.

agreement with the ab initio molecular dynamics simulation in [32], which involved a much smaller sample with periodically based domain walls and estimated the average wall thickness to be 0.56 nm.

According to our calculations and results in the Figure 7.4, even if most of the change in polarization happens very close to the domain wall itself, the presence of the domain wall is noticable far away from the wall. A long, smooth "tail" of the polarization switching is noticable even 12 nm away from the wall in one direction. This is understandable, because the long ranging effects of the Coulombic interactions spread the presence of the defects far away into the body of the sample.

These results call into question the validity of modeling domain walls using specimens consisting of only 10-100 atom supercells with periodic boundary conditions, as is common in ab initio and other molecular dynamic calculations. Even if the values of energy in those samples are a good approximation, the modeling approximates only the actual deformation near the wall.

These results also pose the question of how we should define the domain wall width when it posseses long ranging effects? Should it be defined as when the polarization has returned to its 60%, 90% or 99% of the normal bulk tetragonal polarization?

7.2.2 Wall Energy

We calculated the energy of the wall to be 353 mJ/m^2. Experiments by Merz [121] estimate the energy to be 10 mJ/m^2 and the experiments by Fousek et al. [125] estimate the energy at 3 mJ/m^2. Theoretical calculations by Bulaevskii [126] estimate the energy at 10.5 mJ/m^2 using a Landau-Ginzburg based continuum model and Lawless [119] estimated it at 1.52 mJ/m^2 using a point-dipole microscopic phenomenological model. Relatively recently, Padilla et al. calculated the wall energy to be 16 mJ/m^2 using first principles effective Hamiltonian calculations [32].

The experimental results available are near a phase transition. Also, the domain walls

in experiments are likely to be not defect free and boundary conditions not idealized as we assume in our work. The results from phenomenological theories required phenomenological input and relied on many assumptions. The ab initio calculation by [32] is probably the most reliable one to compare with our results. The results from [32] change with the size of the supercell (and our sample is much larger than the supercell used in the reference) and with temperature. In our work, we assumed zero temperature during our calculations and that might have led to overestimating the energy. The potential we use, as any shell potential, is designed to approximate the ab initio calculations, and our calculations of energy are only as good as the potential itself. We are confident that our energy calculations give a very good approximation of the value of energy, as good as the molecular dynamic simulations with the same potential under the same boundary conditions would give, if those simulations were able to simulate as many atoms as in our sample.

7.2.3 Bulk Assumption Justification

We would like to address the topic about how the boundary conditions and presence of the surfaces influence the results of our study. The surface will influence the behavior of the atoms just below it. But many tens of unit cells inside the sample, away from the surface, are no longer affected by it as our study shows. The results of our study are shown in Figure 7.6. Shown are coordinate profiles for the OxygenX atoms, which look as almost one line.

The X coordinate versus the Z coordinate of the atoms are shown for the following unit cells

$$(l_x = 0, \quad l_y = 0)$$
$$(l_x = 1, \quad l_y = 0)$$
$$(l_x = -1, \quad l_y = 0)$$
$$(l_x = 3, \quad l_y = 0)$$
$$(l_x = 5, \quad l_y = 0)$$
$$(l_x = 0, \quad l_y = -1)$$
$$(l_x = 0, \quad l_y = 1)$$
$$(l_x = 0, \quad l_y = 3)$$
$$(l_x = 0, \quad l_y = 5)$$
$$(l_x = 0, \quad l_y = 10)$$

For ease of comparison, the coordinates are adjusted by rigidly shifting them by a certain value. As one can see, all ten plots are almost exactly the same. Even 10 unit cells away from the central Z axis, the atoms are in the same equilibrium state as on the axis itself. This proves that, other than for some surface layers, the bulk assumption is well justified in the sample.

7.3 Conclusion

We applied complex lattice Quasicontinuum theory to study a 180 degree domain wall. We are able to simulate, concurrently, approximately 11 million atoms without imposing periodic boundary conditions. We verify that the conditions of our simulations correspond to large bulk homogeneous domains at each side of the wall. We find that the domain wall thickness lies in the range of 4-6 unit cells or 1.5-2.5 nm, where most of the polarization switching

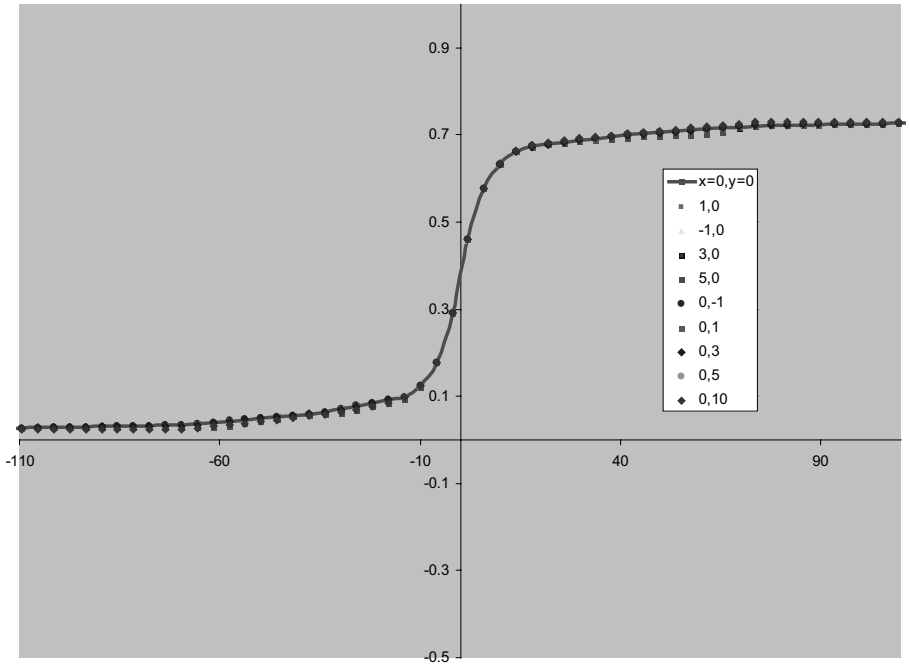

Figure 7.6: To the justification of bulk conditions in our study.

occurs. We also see long range effects arising from the presence of the wall which were not seen in the previous molecular dynamics simulations. Our predictions of the domain wall thickness lie within the range of experimental calculations and are also in very good agreement with theoretical and numerical calculations. Since the wall thickness is so atomistically thin, the question arises if it is possible to model the wall using phenomenological approaches. On the other hand, ab initio molecular dynamics simulations which can model the configuration of the wall with great precision close to the wall entirely miss the long range effects we found, due to the use of small samples with periodic boundary conditions.

Chapter 8

Crack in Initially Tetragonal Phase $BaTiO_3$ Specimen Using Goddard et al. Potential

The complex lattice Quasicontinuum theory is able to handle much more than static problems. Static problems, especially if they show a high degree of symmetry, can be handled by many other theories (for example molecular dynamics or lattice statics). Quasicontinuum theory does not require, and does not need to assume, any symmetries or periodicity in the problems it studies. Moreover, it can handle dynamic problems quasistatically with dynamic multiscale resolution with adaptive mesh selection (discussed above at section 3.2).

As an example of a challenging problem to model, we studied a crack in $BaTiO_3$ tetragonal phase specimen.

This simulation should be primarily viewed as an example of Quasicontinuum theory application. The results obtained should be considered as preliminary, as there are still many difficulties in determining the appropriate boundary conditions and triangulation of the specimens for the simulation, complicated by the facts of atomistical consideration of a traditionally continuum problem and employment of long ranging electrostatic potential.

8.1 Motivation

Ferroelectric materials, especially $BaTiO_3$, are currently widely used in actuators and sensors. These devices often operate under harsh mechanical and electrical conditions where the brittle crystalline ferroelectrics can fracture [127]. Therefore it is very important to understand how those materials fracture in order to build reliable and efficient devices.

Modeling of cracks and fracture in ferroelectrics is very complicated, as an initially homogeneous ferroelectric polarization becomes subjected to a highly non-uniform load, disturbing the very fine balance of electrostatic and elastic properties which lead to ferroelectricity. Very high electrical and mechanical non-linearities occur at the crack tips in these materials.

There has been a great deal of experimentation involving cracks in ferroelectrics under different experimental setups, see [128], [129], [130], [131], [132], [133], [35], [134], [135], [136], [137], [138], [139]. These experiments have observed that fracture in ferroelectrics is a coupled electromechanical process, and most of the experiments measured a toughening effect believed to be due to domain switching in front of the crack tip. Although they give very interesting results on crack propagation and fracture properties, these experiments have not had the precision necessary to capture effects atomistically close to crack tips.

It is still very hard to conduct precise fracture experiments, especially on a small scale in perovskite ferroelectrics. They are very brittle materials and cracks are usually introduced through fast indentation resulting in fracture of the specimen, with no control over the initial crack. Also, it is very hard to produce a defect free specimen of the size required to conduct crack experiments, and the initial fracturing through indentation is likely to introduce many unwanted defects into the specimen.

Our simulations can shed some light on what processes are happening at a crack tip and how the ferroelectricity of the material influences the mechanical fracture properties of the material.

There has been some theoretical and numerical research involving cracks in ferroelectrics,

see [34], [140], [141], [142], [143]. This research has been done on a continuum scale using phenomenological constitutive relations. It has emphasized the dependence of fracture parameters on domain switching under fracture stress. These continuum studies cannot predict atomistic behavior at the crack tip. Moreover it is very difficult to determine the correct parameters for the constitutive relations from available experiments. The Quasicontinuum model can derive the input parameters used in continuum modeling directly from atomistics.

8.2 Setup

We consider a pure tetragonal phase $BaTiO_3$ specimen. The specimen has a tetragonal shape which represents half of the original cracked specimen, see Figure 8.1. The $BaTiO_3$ potential and the Quasicontinuum configuration for $BaTiO_3$ are the same as described in the previous chapter, see section 7.1. We model only half of the specimen ending with the line of symmetry lying through the crack tip. The static, not yet propagating, crack has this line, see Figure 8.1 as the symmetry line. Thus we only need to model half of the actual size of the specimen, reducing the computational effort by half. It also allows us to use an optimal mesh, because the deformed body position of the half of the loaded crack is convex. Our simulations are by no means restricted to simulations of half of a crack. We can simulate the entire crack if needed as, for example, we would need for a dynamic crack to allow non-symmetric crack propagation.

The loading belongs to mode I, see Figure 8.1. The study was under plain stress to simulate the behavior of thin films.

The boundary was kept fixed at the calculated value of the induced opening displacement, to assure the correct loading of the specimen. The entire specimen was subjected to the initial opening displacements of the mode I loading. Afterward, all but small number of surface atoms were allowed to relax into the equilibrium configuration.

The surfaces not including the crack were fixed to three unit cell layers as in the domain

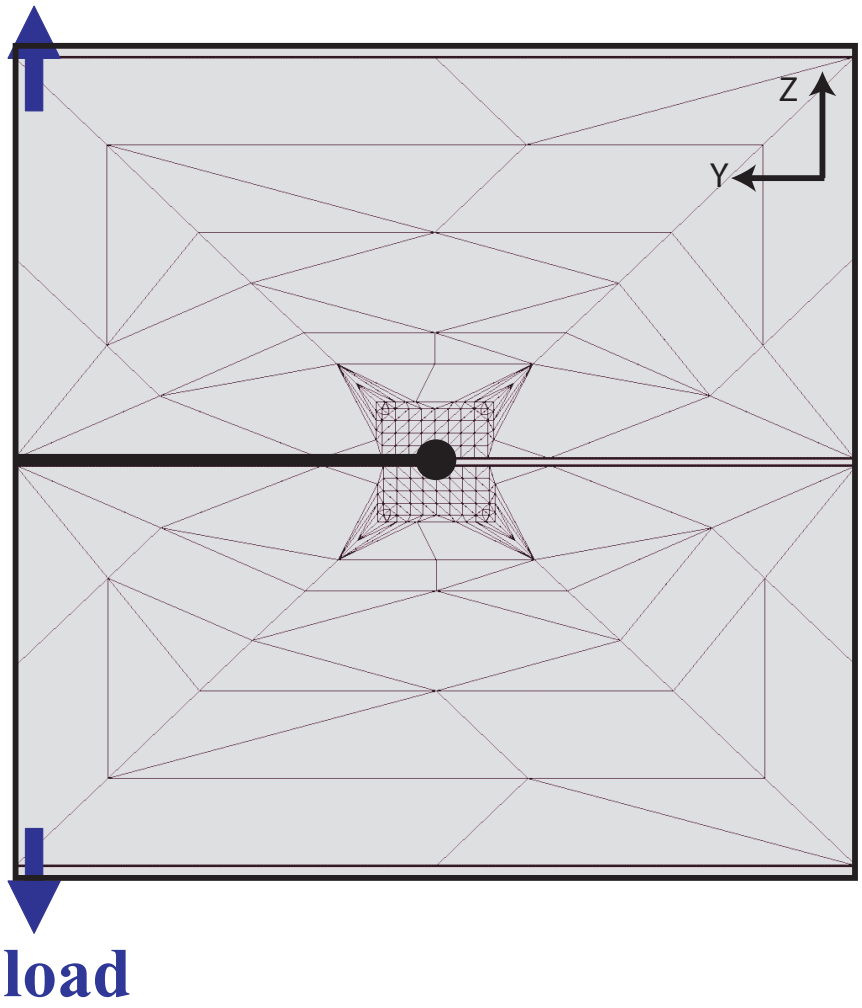

Figure 8.1: Crack calculations setup.

wall example, see Chapter 7. The surface including the crack was fixed to only one unit cell layer to allow for the equilibration process very close to the crack tip itself - the area we are most interested in. The other two layers close to the surface are in equilibrium when there is no loading on the specimen, in order to suppress free surface artifacts.

The crack opening displacements are of the following form [144] :

$$\begin{aligned} u_x &= \frac{K_I}{2\mu}\sqrt{\frac{r}{2\pi}}\cos\left(\frac{\theta}{2}\right)\left[k-1+2\sin^2\left(\frac{\theta}{2}\right)\right] \\ u_y &= \frac{K_I}{2\mu}\sqrt{\frac{r}{2\pi}}\sin\left(\frac{\theta}{2}\right)\left[k+1-2\cos^2\left(\frac{\theta}{2}\right)\right] \end{aligned} \tag{8.1}$$

where the x axis is along the crack, the y axis perpendicular to it, θ is the angle of the point (x,y) with the x axis, r the distance of this point from origin and k is of the form:

$$k = \frac{3-\nu}{1+\nu}$$

We choose Poisson ratio ν to be 0.5 assuming incompressibility. We also incorporate the shear modulus μ and the stress intensity factor K_I into one loading parameter, which we control.

These values of elastic constants are only an approximation of the exact values for $BaTiO_3$. The actual values are of tensorial nature. The elastic properties of the $BaTiO_3$ tetragonal phase pure crystal, which belongs to 4mm point group symmetry, have been determined in experiments in [15], [145], [146] and [147]. Knowing the values of the elasticity modulus tensor C_{ijkl} from the above references, we can determine the mode I crack opening displacements and strains for the pure tetragonal $BaTiO_3$ crystal.

But this data is likely not usable in our calculations. The values of elastic constants strongly depend on the underlying interaction. Since the potential we are using is an approximation to this interaction, we need to determine elasticity properties based directly on

this interaction by evaluating ([148] and [58]):

$$C_{ijkl} = \frac{1}{V}\left[\frac{\partial^2 E(V,\epsilon)}{\partial \epsilon_{ij}\epsilon_{kl}}\right]_{\epsilon=0}$$

where ϵ is the strain tensor, E the total energy of the periodic crystal corresponding to strain ϵ and volume V is the volume of the unstrained crystal. For more details see [149] and for an example see [150]. Subjecting the crystal to some strain and determining its energy based on the potential we are using will give us the components of C_{ijkl} we need to describe mode I crack loading of the crystal. Calculations of the actual tensors goes beyond the scope of this work. Here an approximation of these values was used. As the results of the calculations show, the selected values should be very close to the real ones, because the forces and deformation from the loading in equation 8.1 result only around the crack tip as expected.

The sample used in the simulation was chosen to be 33x65x11 unit cells (as mentioned before, this represents half of the actual size). Eleven unit cells is the thickness of the specimen and the plane perpendicular to the crack plane has originally a square cross-section of 65 unit cells. Thus, our simulation considers 117,975 atoms (or an original specimen of 235,950 atoms, when considering the entire specimen).

8.3 Results

8.3.1 Quasistatic Crack Loading and Adaptive Atom Selection

Three quasistatic loading steps were performed. The initial load and the loading steps were carefully selected to be small enough to justify the quasistatic assumption but to be large enough to show change in the specimen due to loading. The loading step measured in units of displacements (see equation 8.1) was 0.001 Angstroms.

After each loading step, the equilibrium state with the load was found with the solver and

adaptive mesh refinement was performed. Figure 8.2 shows three successive triangulations or meshes: one initial triangulation (Mesh I), and three after loading, successful equilibration and mesh adaption (Mesh II, Mesh III and Mesh IV). The mesh adaptation is shown on one mesh out of five Quasicontinua as an example, and the other meshes are adapted in a very similar way. We can see an increase of the size of the finer resolution atomistic region near the crack tip due to the increasing crack load. The region further away from the crack tip remains the same resolution as we increase the load. This refinement at the crack tip is what should be expected from a crack example if it was a continuum calculation. That is the same here because the deformation energy is high at the tip. This refinement also justifies our approximation of the elastic constants for $BaTiO_3$. Another point which we would like to mention here is that this example demonstrates that adaptive atom selection is working in the implementation of complex lattice Quasicontinuum, and is able to perform even in such complicated systems as a crack in Barium Titanate under load.

8.3.2 Polarization Switching due to Loading

A large amount of experimental data on cracks in ferroelectrics suggest that the connection between elasticity and polarization in those materials is very explicit. Polarization greatly affects the conditions in which cracks will propagate. Domain switching in front of a crack tip increases fracture toughness in ferroelectrics. This domain switching is not well understood as it introduces regions of great electrical and mechanical non-linearity in the material and is therefore very difficult to describe within the usual continuum approaches. Quasicontinuum can give an atomistic insight into the process of domain switching at the crack tip and help to recover the parameters needed for continuum models.

We indeed observe a change in polarization due to the loading in the crack specimen; the change occurs due to the boundary conditions of crack loading, not as an assumption as in many models. The simulation poses a challenge as the loading is highly non-uniform, and because the initial polarization is homogeneous, it is not easily predictable how the crack

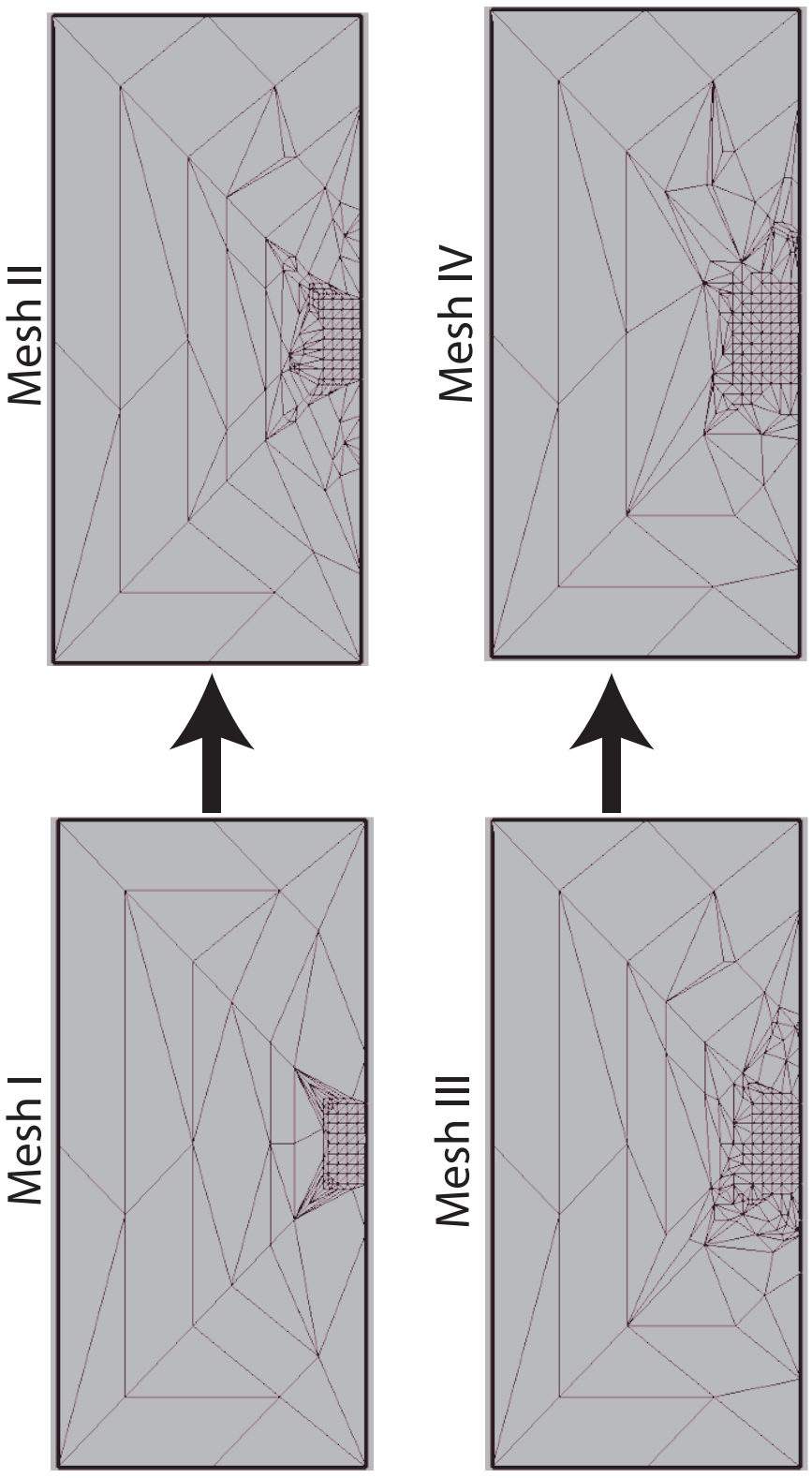

Figure 8.2: Adaptive mesh refinement in crack calculations.

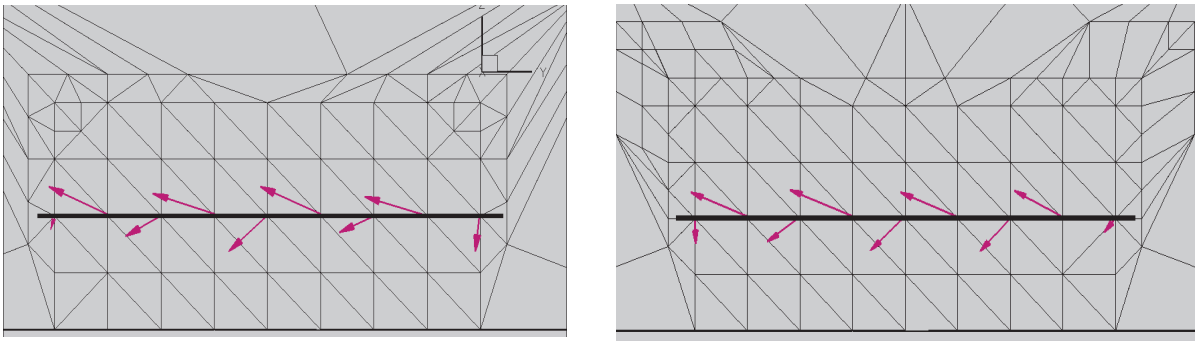

Figure 8.3: Polarization changes after the first two loading steps.

loading will influence polarization.

The change in polarization grows with increasing load. See Figure 8.3 for the polarization changes after the first and the second load, indicated along one line. The originally homogeneous polarization in Y direction (see Figure 8.1), obtains positive and negative Z components and grows generally in magnitude. Though the change is not uniform, a pattern starts building. To show this we indicate the polarization along one line in Figure 8.3, parallel to the Y axis and the crack line. The Z coordinate of the polarization alternates between the same amount but opposite sign, and the Y coordinate remains approximately the same along this line. It appears that the crack loading influences the sample such that at the crack tip a very small and thin domain starts building in place of the original homogeneous polarization. The magnitude of the polarization vector becomes larger than the original pure tetragonal polarization, and grows and becomes more distinct as the load increases.

The polarization after the third loading step, which is the final step of the simulation is shown in the Figure 8.4. Figure 8.4 shows the area around the crack tip (on a similar scale as in the previous picture). The crack tip itself is indicated with a circle. The vectors of polarization are shown for each unit cell. The location of the base of the vector is the location of the Barium atom in this unit cell. In the Figure 8.4 we can see this pattern: thin, small domains with 180 degree and 90 degree orientation to each other. This pattern propagates further into the specimen with increasing load.

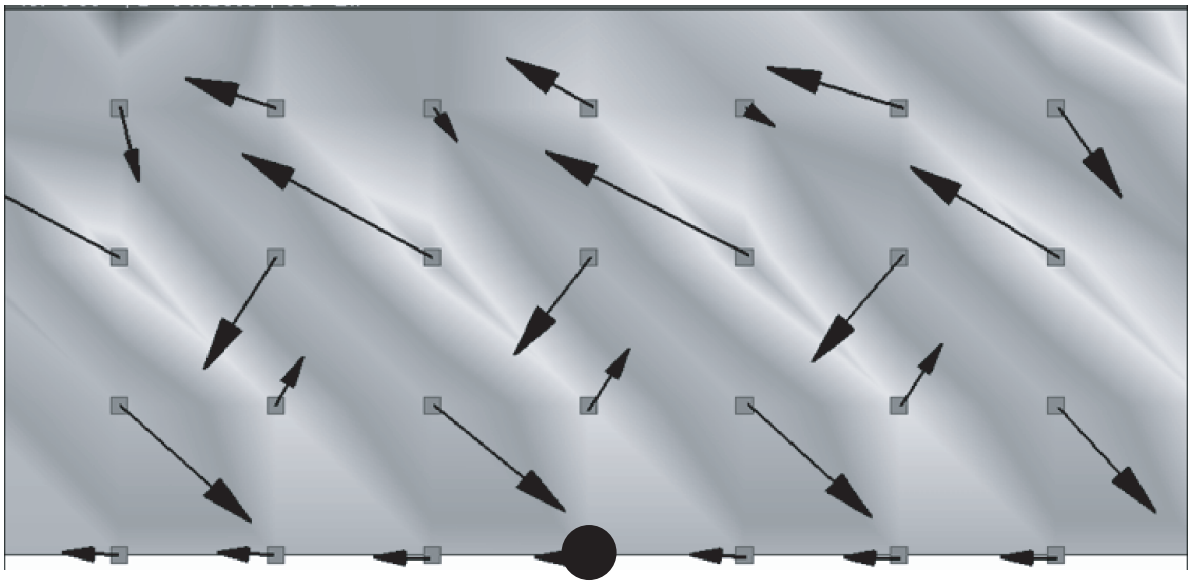

Figure 8.4: Polarization after the final load equilibration.

The polarization is known to depend on the unit cell chosen and the method of calculation. We will explain here the method we used to calculate the polarization. The unit cell chosen is the same as in Figure 7.1. The following atoms belong to the unit cell (length is in the units of the lattice constants):

$$\begin{array}{ll} \text{Ba} & (0,0,0) \\ \text{Ti} & (1/2,1/2,1/2) \\ \text{Ox} & (0,1/2,1/2) \\ \text{Oy} & (1/2,0,1/2) \\ \text{Oz} & (1/2,1/2,0) \end{array} \tag{8.2}$$

If the atoms in the unit cell are chosen to be at the exact location in equation 8.2 we have a structure we will call "symmetric tetragonal structure" throughout this work. This structure does not produce a net polarization because it is symmetric. Knowing this fact and also the

fact that the total charge of the unit cell is zero, we calculate the polarization P in any other configuration as

$$P = \sum_{all\ ions\ i\ in\ the\ unit\ cell} Q_i \cdot \delta \mathbf{d}_i, \tag{8.3}$$

where $\delta \mathbf{d}_i$ is the shift of the ion i with respect to its position in the symmetrical tetragonal structure and Q_i is the charge of ion i.

Back to our results, the tetragonal phase of $BaTiO_3$ is characterized by shifts from the symmetrical tetragonal structure, which result in the net polarization of the specimen. The initial homogeneous tetragonal polarization prior to the loading can still be seen at the lower end of Figure 8.4 since, as mentioned before, this one unit cell surface layer has been constrained during the simulation.

The rest of the unit cell polarization vectors around the crack tip can be seen in this Figure. They were calculated using equation 8.3. The Z component of the polarization becomes significant, after being zero before loading, and alternates between positive and negative values. The Y component of the polarization becomes alternating too, in some areas reversing orientation.

The pattern is relatively small, smaller than typical domain sizes. Larger specimens and larger loads would be needed to simulate something on the order of typically observed domains. But even in a smaller sample we are able to notice domain initiations and polarization patterns around the crack tip.

8.4 Conclusions

We were able to perform quasistatic loading of the crack in a tetragonal phase $BaTiO_3$ sample. We were able to find the right boundary conditions to make the simulations possible. The adaptive atom selection feature has been tested on this example and we see mesh

refinement at the crack tip with increasing load.

We observe a systematic polarization pattern building around the crack tip: initiation of domain layers and 90 and 180 degree domain walls. The pattern grows and becomes more distinct with growing crack load.

Polarization changes calculated from first principles atomistic based approaches explain the observed changes of fracture toughness in ferroelectrics which is attributed to domain switching in front of crack tips.

Chapter 9

Study of 180 Degree Domain Wall in $PbTiO_3$ Performed Using Sepliarsky et al. Potential

9.1 180 Degree Domain Wall Setup

9.1.1 $PbTiO_3$ and Its Properties

Another notable member of ferroelectric perovskite family is Lead Titanate, $PbTiO_3$. The structure of the $PbTiO_3$ unit cell is shown in Figure 9.1. It is similar to the structure of $BaTiO_3$ but with a Lead atom instead of a Barium atom.

In contrast to $BaTiO_3$ which has a complicated dynamic behavior, $PbTiO_3$ exhibits a classical displacive [151] ferroelectric transition [7] (although we should mention that the debate about whether the transition in $BaTiO_3$, and even in $PbTiO_3$, is of displacive or order-disorder [152] type is still ongoing [153], [154]).

Above the temperature of 765K under normal pressure, $PbTiO_3$ is in a cubic phase, which is paraelectric and does not possess a permanent polarization. Below 765K the material is in tetragonal ferroelectric phase. This phase extends to zero temperature. Six orientations of spontaneous polarizations, equivalent to (001) direction are possible in this phase.

The differences in behavior of $BaTiO_3$ and $PbTiO_3$ are attributed to their different electronic structures. The Pb $6s$ and O $2p$ states are strongly hybridized, whereas the Ba ion is

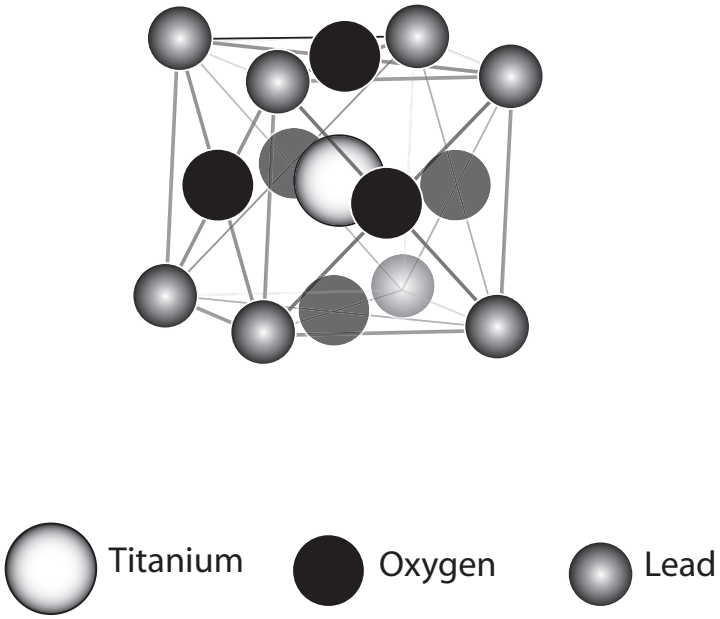

Figure 9.1: Unit cell of $PbTiO_3$ crystal.

essentially fully ionic [154].

The experimental lattice constants in the tetragonal structure of $PbTiO_3$ are

$$a = b = 3.89\mathring{A} \qquad c = 4.15\mathring{A}$$

The ratio $c/a = 1.065$ is large compared to other perovskite ferroelectrics.

The electronic structure of periodic bulk $PbTiO_3$ crystal has been widely investigated, see for example [155], [154], [156], [157], [158], [159] and the references therein. Many efforts have been made in the above papers to explain the origin of ferroelectricity in $PbTiO_3$.

Lead Titanate has been widely used for its piezoelectric and dielectric properties, and widely researched both experimentally and theoretically, but a lot of problems still remain poorly understood.

Element	Core Shift [$\AA$]	Shell Shift [$\AA$]
Pb	0.	0.08261
Ti	0.185696	0.207230
Ox	0.455471	0.577244
Oy	0.552925	0.535008
Oz	0.552925	0.535008

Table 9.1: The tetragonal phase shifts of cores and shells in $PbTiO_3$ in Sepliarsky et al. potential

9.1.2 Notes on the Potential

The shell model potential by Sepliarsky et al., described in detail in Chapter 5, was used for the calculations. The same group very kindly gave us the equilibrium data for the bulk tetragonal phase, the lattice constants and the shifts of the ions. The lattice constants corresponding to bulk tetragonal $PbTiO_3$ phase with this potential are

$$a = b = 3.9053\AA \qquad c = 4.1514\AA$$

These values are very close to the experimental values.

The potential treats cores and shells for each atom separately and so we introduced ten different independent Quasicontinua into our program (corresponding to each core and shell sublattice). The shifts from the tetragonal symmetrical structure for the bulk tetragonal polarization in this potential are shown in Table 9.1.

The investigation of the potential[160] revealed that the full Hessian does not possess only positive eigenvalues, required for the full stability of the potential. The Hessian considered is a symmetric 30x30 matrix with the fields being the second derivatives of the energy of the periodic crystal with respect to the three coordinates of all ten ions in the unit cell. We encountered this fact on all possible shell potentials for ferroelectric perovskites we

considered, as they are only stable with imposed constraints such as lattice symmetry.

However the potential is stable if movement is restrained to only one direction - the polarization direction. This direction is the most interesting and relevant to study, as the shifts in this direction give rise to constant polarization. The Hessian in this case reduces to a 10x10 dimension with possession of all positive eigenvalues [160]. This is already a very high number of stable eigenvalues, as we discovered reviewing and considering other shell potentials.

As the next step, we considered the range of the potential. We considered the Coulombic and non-Coulombic part of the potential separately. The Coulombic part of the potential was evaluated with the Wolf et al. [29] summation rule, described in detail in Chapter 6. After considering the convergence of the Madelung energies and forces of the ions in the pure tetragonal phase with respect to the cutoff radius, we found out that in this system we need to use the full version of Wolf's summation including a small damping of the electrostatic potential. We also found that we would need to use a longer cutoff radius for Wolf's electrostatic summation than in the $BaTiO_3$ calculations. We attribute the need to damp and the longer cutoff radius to the fact that in this case the system is composed of ions, with some of the ions being very close to each other (the core and shell of the same atom). This introduces a numerical electrostatic instability into the system which becomes of longer range. We determined that the following damping parameter α and the cutoff radius r_c are optimal for our numerical investigations

$$\alpha = 0.2 \qquad r_c = 16\mathring{A}$$

A very interesting feature of this potential is that the non-electrostatic part of it is very long ranged. This part is often called short ranged interaction, as it would have decayed much faster than the electrostatic interaction if we would not have used Wolf's summation rule for it. To avoid confusion, we will refer to this short ranged interaction as a non-Coulombic or

non-electrostatic interaction.

The Lead-Titanium non-electrostatic interaction, bounded to the shells of the atoms, is very long ranged. The optimal cutoff radius for this interaction, enough to evaluate the summed value of the energy or the force (with precision, which is considered to be zero in this potential) is approximately 10 unit cells or about $40\mathring{A}$. This value for the cutoff radius for each Lead or Titanium atom would require considerable memory and runtime for our simulations, significantly lowering the size of the sample we can study.

Therefore we decided to use a smaller cutoff radius and also introduce some optimizations into the program. We modified the program to allow different cutoff radiuses for the Coulombic and non-Coulombic interaction summations. This allowed us to be able to use the optimal cutoff parameter for each ion. Only the non-electrostatic interaction summation for the Lead and Titanium shells was carried out with a large cutoff radius. All other interactions had a smaller cutoff radius, which was specifically chosen for the particular type of interaction of the particular ion. The cutoff radius of the interaction of the non-electrostatic Lead and Titanium shells was taken to be $30\mathring{A}$ after careful research, as a compromise between precision of summation and computational efficiency.

It is important to mention that this potential is taken from molecular dynamics. There it is the practice to consider values of $0.005eV$ and below to be negligible or to be "zero". This contrasts with other potentials we have been working with, where it is relatively easy to determine the equilibrium configuration with any meaningful precision. It is theoretically possible for this $PbTiO_3$ potential as well, but due to the complexity of the potential and the crystal system itself, it would require too much computational time and effort. Thus the equilibrium configuration we inherit from molecular dynamics is an equilibrium configuration in the precision where $0.005eV$ equals "zero" for the forces and is not necessarily an equilibrium if at a greater precision.

We introduced a feature into the program, to consider atoms with a force of equal to or smaller than $0.005eV$ to be in an equilibrium state, and as long as they are in that state,

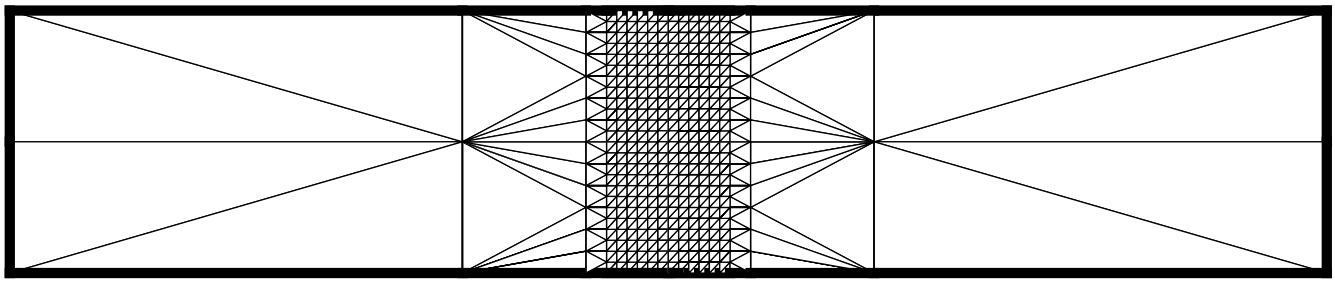

Figure 9.2: Mesh used for 180 degree domain wall calculations.

we choose not to equilibrate them as part of the general conjugate gradient procedure. We simulated the domain wall in $PbTiO_3$ with and without this feature and found out that for this particular potential the results are better with this feature turned off. This allows the conjugate gradient solver to find the solution much faster. This also probably indicates that the equilibrium given to us from molecular dynamics is very close to the real equilibrium state, at least in the range of the equilibration we consider. But this feature might be very useful in considering other potentials for complicated systems if those potentials are taken from molecular dynamics to correspond to molecular dynamics assumptions.

9.1.3 Initial Triangulation and Positions of Atoms

Figure 9.2 shows the mesh considered in the domain wall example calculations. The size of the sample is 25x25x129 unit cells with simultaneous consideration of more than 400,000 atoms. The atomistic resolution of the mesh near the wall is 13 unit cells with the mesh gradating continuously to a coarser resolution further away from the wall. The polarization, and thus all the shift of ions from symmetric tetragonal structure, are in X direction. The wall is perpendicular to the Z axis and is in the $Z = 0$ plane.

Our simulation is at zero temperature. $PbTiO_3$ is in ferroelectric tetragonal phase at zero Kelvin temperature in nature, so we simulate the physically correct state of the crystal. We could consider finite temperature, adding random motion controlled by a random number

generator to each ion or explicitly introducing entropy into the model, but so far this is beyond the scope of this work. Extension of non-local Quasicontinuum to account for finite temperature is in progress in Professor Ortiz's group [161].

We allow the movement of all ions only in the polarization direction, which is X direction in our sample. As mentioned the potential is proved to be stable under these considerations. Also many theoretical [162], [163] and experimental [164] investigations suggest that polarizations at 180 degree domain walls have only one component (in the bulk polarization direction) and the changes in polarization are also restricted to that direction. Huang et al. [165] refines this statements by investigating Ising (only one polarization component) and Bloch (two polarization components with a rotating polarization vector). They find that in ferroelectric perovskites in contrast to uniaxial ferroelectrics, both Ising and Bloch type walls are possible, but the Ising walls have lower energy and therefore are observed more often.

We subject the simulation sample to initial displacements corresponding to the positive bulk tetragonal phase polarization in the part of the sample with $Z < 0$ and to the negative bulk tetragonal phase polarization in the part with $Z > 0$. Effectively, the initial configuration corresponds to a 180 degree domain wall with zero thickness between two bulk tetragonal phase domains of opposite polarization.

All atoms in the sample, other than the surface atoms, were allowed to relax into the equilibrium configuration, which was found with the conjugate gradient solver simultaneously considering all atoms in the sample. The 9 surface unit cells were kept at fixed bulk polarization displacements to suppress surface effects and to simulate bulk domains boundary conditions. This large amount was necessary due to the large range of the non-Coulombic interaction in the sample.

The boundary conditions included an offset between the two opposite polarization domains. The offset calculated with this specific version of the potential interaction to minimize the total energy of the sample was kindly provided to us by Arash Yavari, Caltech. This fea-

ture is observed in some other ab initio molecular dynamics simulations [36] and is strongly interaction dependent. We must note here that there are also theoretical and numerical calculations which do not consider an offset between the domains, although this degree of freedom logically should be included in the search for the minimization of the energy.

9.2 Results

The results of the calculation are the three dimensional coordinates of all the atoms in the sample. To visualize the important features of the results we plot, as in the case of the $BaTiO_3$ domain wall, the atomic coordinate profiles across the domain wall for all ions. In Figure 9.3 we plot the coordinate profiles of atoms in the middle of the specimen, cutting across the wall. For all atoms in the unit cells on the line $l_x = 0$, $l_y = 0$ and l_z variable we plot the X versus Z coordinates in the units of Angstroms. As we can see from this picture, the change from plus to minus shifts in the coordinates, which also indicates the switch from positive to negative polarization, happens very fast. Almost all the switching happens in 1-3 unit cells adjacent to the wall, or together 4-6 unit cells total. This gives a wall thickness of approximately 1 nm-2.5 nm.

It is very important to mention here that the range that the potential reaches is huge and the atoms near the wall definitely are affected by atoms far away from the wall, 7-8 unit cells away from them. Thus the very rapid change of the atomic coordinates at the wall from positive to negative values is definitely a feature of the potential. This is intrinsic to the potential and not to the cutoff radius we chose. We believe that this is a feature which should be attributed to the electrostatic interaction of the atoms. The nature of the electrostatic interaction between ions in ferroelectrics crystals makes the transition from positive to negative polarization at the domain wall very rapid, and thus the domain wall thickness atomistically small. For comparison, magnetic walls in ferromagnetic materials, where the ferromagnetism is due to spin coupling, are much wider.

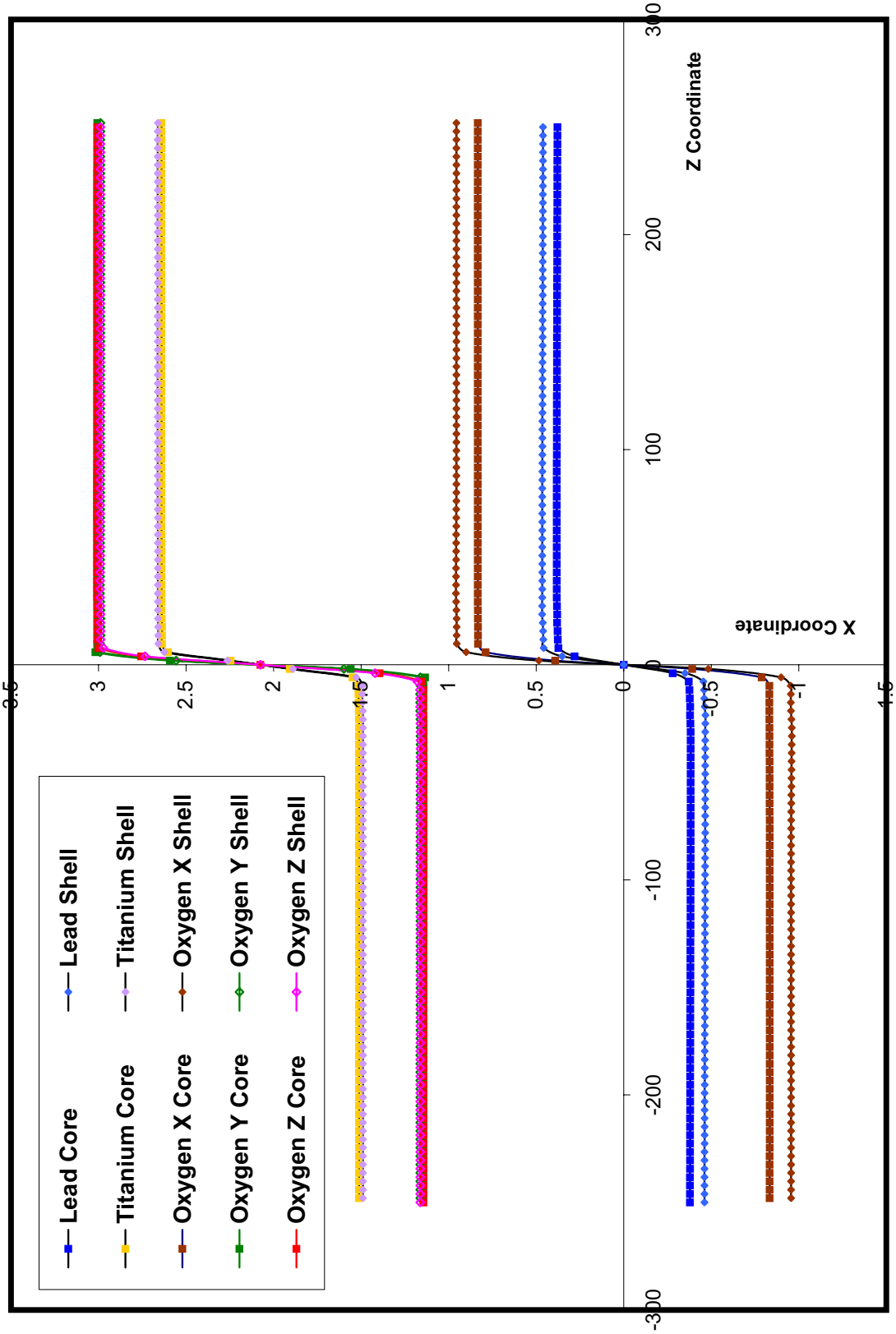

Figure 9.3: Atomic profiles of 180 degree wall in $PbTiO_3$.

Even if most of the switching happens very fast, we observe long "tails" of the wall. The state of bulk polarization does not return for at least thirty unit cells, or approximately twelve nanometers, away from the wall in our calculations. That corresponds to the precision in our simulations, the actual "tail" can be very well much longer.

Here we must again raise the question about how to define the thickness of the domain wall. At what percentage of the return of bulk polarization should the wall be said to end? This is the reason we specify only a range for the wall thickness: 1 nm-2.5 nm, which corresponds approximately to a 70-95% return to the bulk pure tetragonal phase value.

Our calculated wall thickness is in very good agreement with the recent ab initio calculations of domain walls by Meyer and Vanderbilt in [36]. The authors investigated 180 degree domain walls in tetragonal $PbTiO_3$ using a first-principles planewave pseudopotential method based on density-functional theory [166] within the local-density approximation [167]. The pseudopotentials used were of Vanderbilt-ultrasoft type [168] with the semicore Pb $5d$ and Ti $3s$ and $3p$ states explicitly treated as valence states. The authors use supercells of material with periodic boundary conditions, and thus periodic domains and domain walls between them. The supercells investigated contained 30, 40 or 50 atoms in them (domains between walls were 3, 4 or 5 unit cells respectively). These samples are much smaller than the samples in our simulations.

As one of the results, the authors found that polarization at the domain wall changes for the most part in less than two lattice constants, which is consistent with our calculations. But their results could not reveal the long "tails" resulting from the presence of the domain wall which we can see in our calculations. Their specimen, which is very small with induced periodicity of domains in it, does not allow the polarization to relax fully. Thus their results give a good approximation at the domain wall, but not further away from it.

Another interesting result which Meyer and Vanderbilt find in their paper is that, from two possible 180 degree domain wall structures (Lead centered and Titanium centered), the Lead centered structure is a stable one with lower wall energy. We use this fact in our work

by modeling the Lead centered domain wall.

The ab initio study by Pöykkö and Chadi [118] revealed the 180 degree domain walls in $PbTiO_3$ to be extremely narrow with a width of only about two lattice constants. The study was performed using DFT with LDA approach and periodic supercells consisting of total 6, 8 or 10 unit cells.

Our calculations are also consistent with the experimental investigations [37], where the width of the 180 degree wall in $PbTiO_3$ crystals is determined to be of the order of few lattice constants.

Continuum calculations of domain walls based on Landau-Ginzburg model [33] also predict an atomistic thickness of domain walls in perovskites. But the phenomenological continuum description of domain walls which can account for long ranging effects of the wall are questionable in modeling of thin atomistic thicknesses.

Figures 9.4, 9.5, 9.6 and 9.7 represent a zoomed in view of Figure 9.3 close to the wall, showing separate atoms.

Figure 9.4 shows the Lead Core and Shell atomistic profiles at the wall. From this plot we can see that there is a spatial offset of the both domains with respect to each other of $0.3784 \cdot 2\mathring{A}$. We also notice that the coordinates of the atoms at the wall in this case do not monotonely change from a negative to positive position, there is a slight kink in the negative direction before they change polarity. A symmetric kink into the positive direction can be seen at the opposite side of the wall as well.

Figure 9.5 shows the coordinate profiles for the Titanium atoms at the wall, tracking cores and shells separately. Figure 9.6 shows the coordinate profiles for the Oxygen X core and shells. Here we would like to point out the smooth but highly non-linear transition from one side to another.

The Oxygen Y and Oxygen Z atoms are plotted together in Figure 9.7 because of similar behavior in the bulk (the polarization is in X direction). In the plot we observe that, as expected, they are rapidly converging to the same values further away from the wall, where

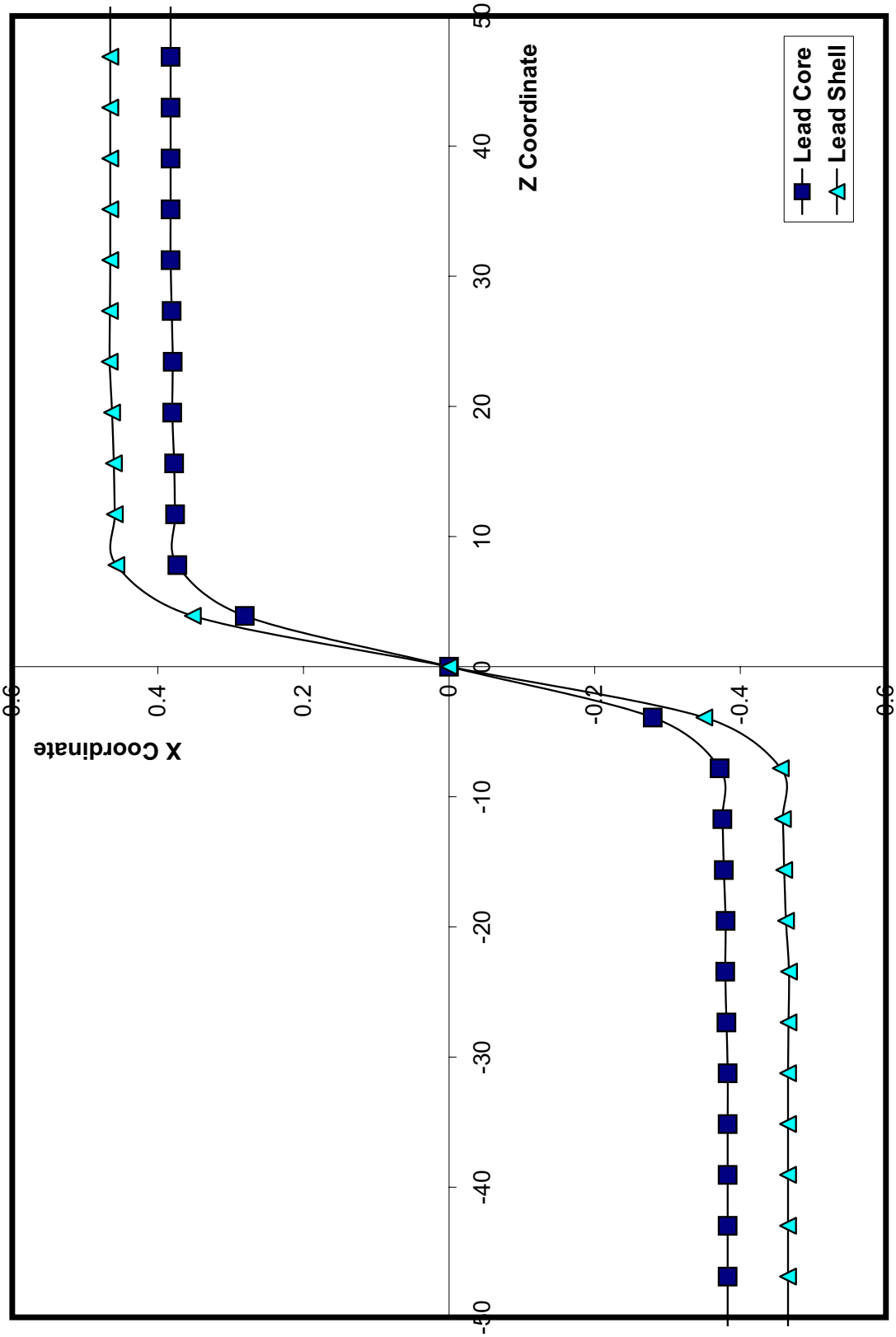

Figure 9.4: Lead core and shell coordinate profiles closer to the wall.

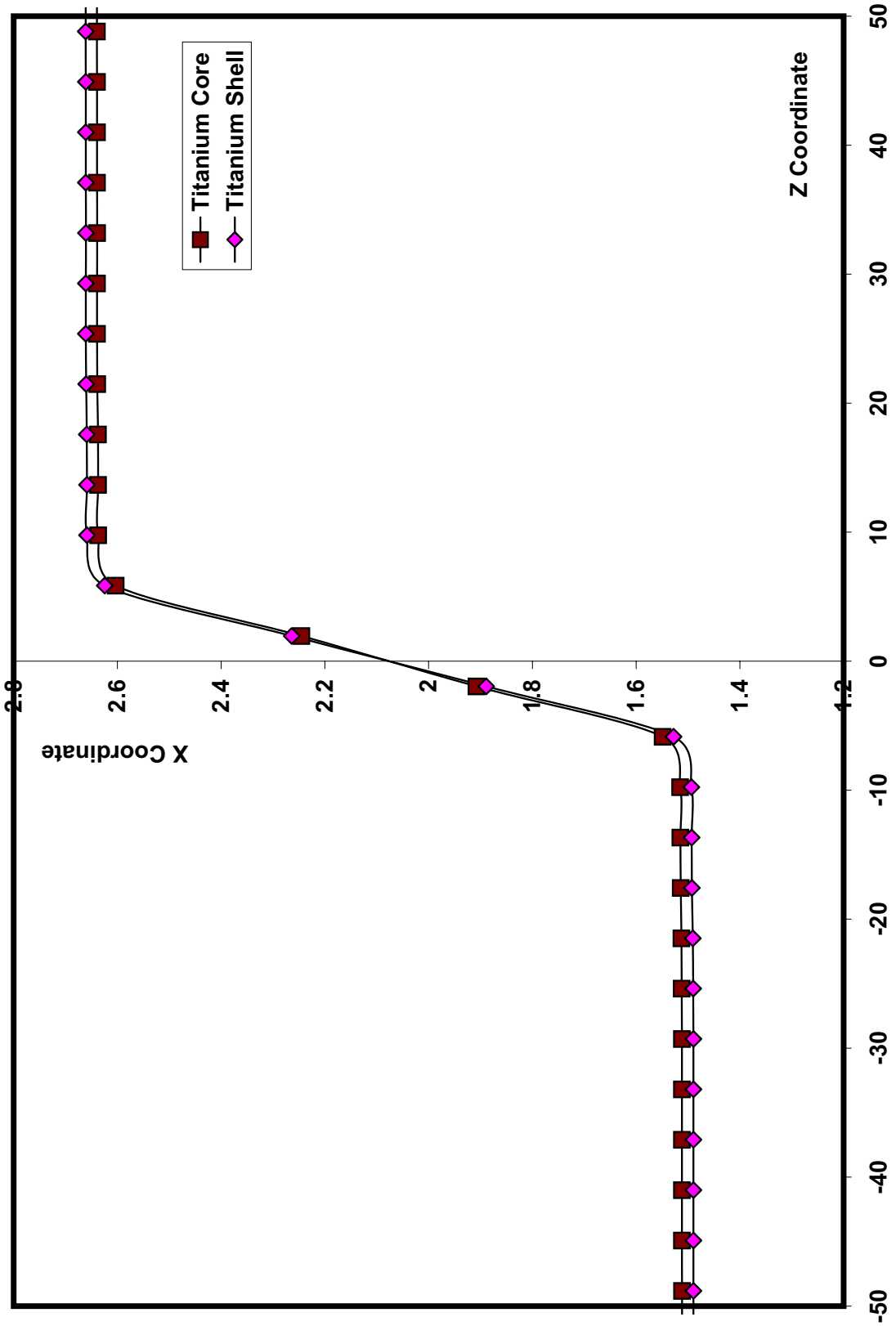

Figure 9.5: Titanium core and shell coordinate profiles closer to the wall.

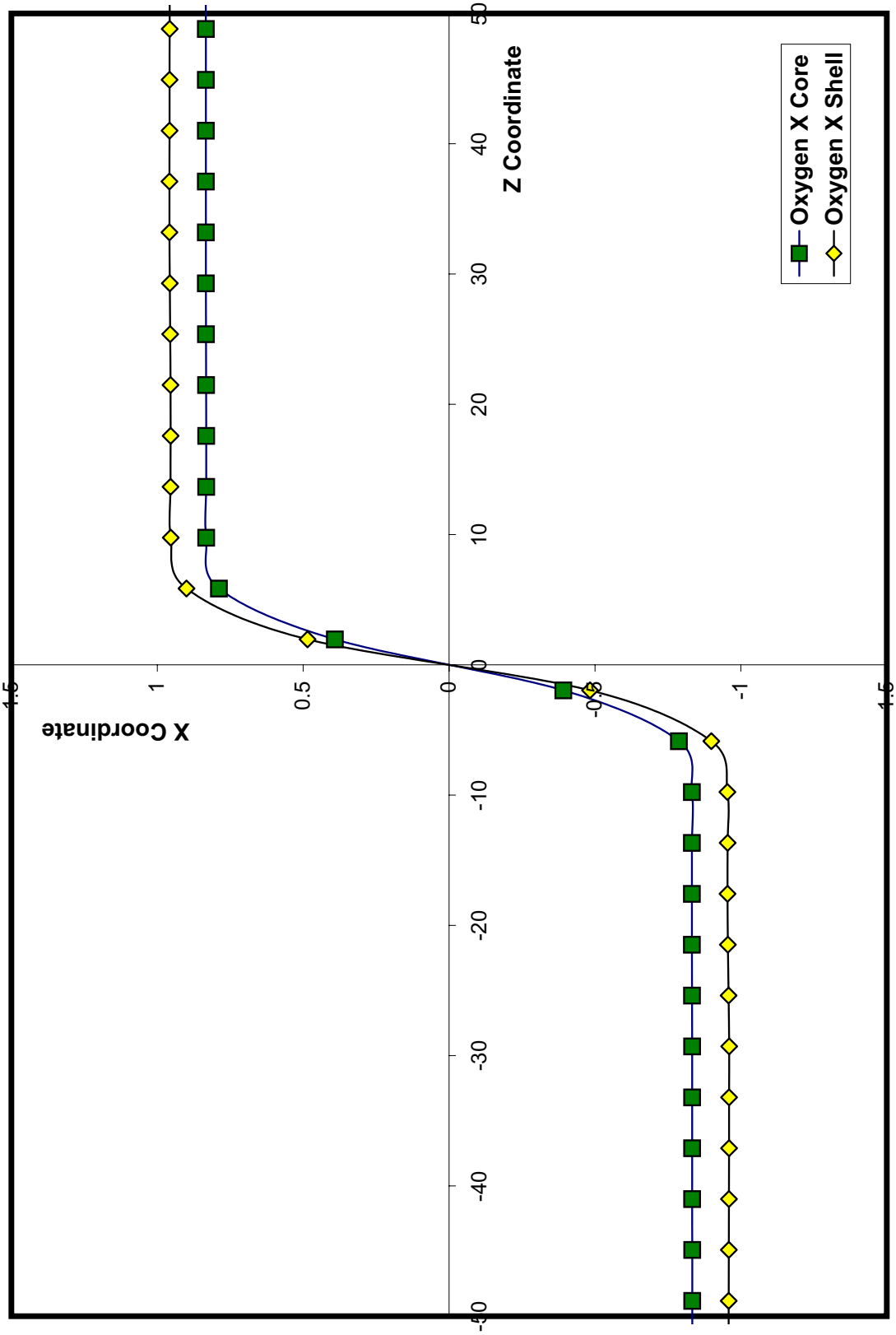

Figure 9.6: Oxygen X core and shell coordinate profiles closer to the wall.

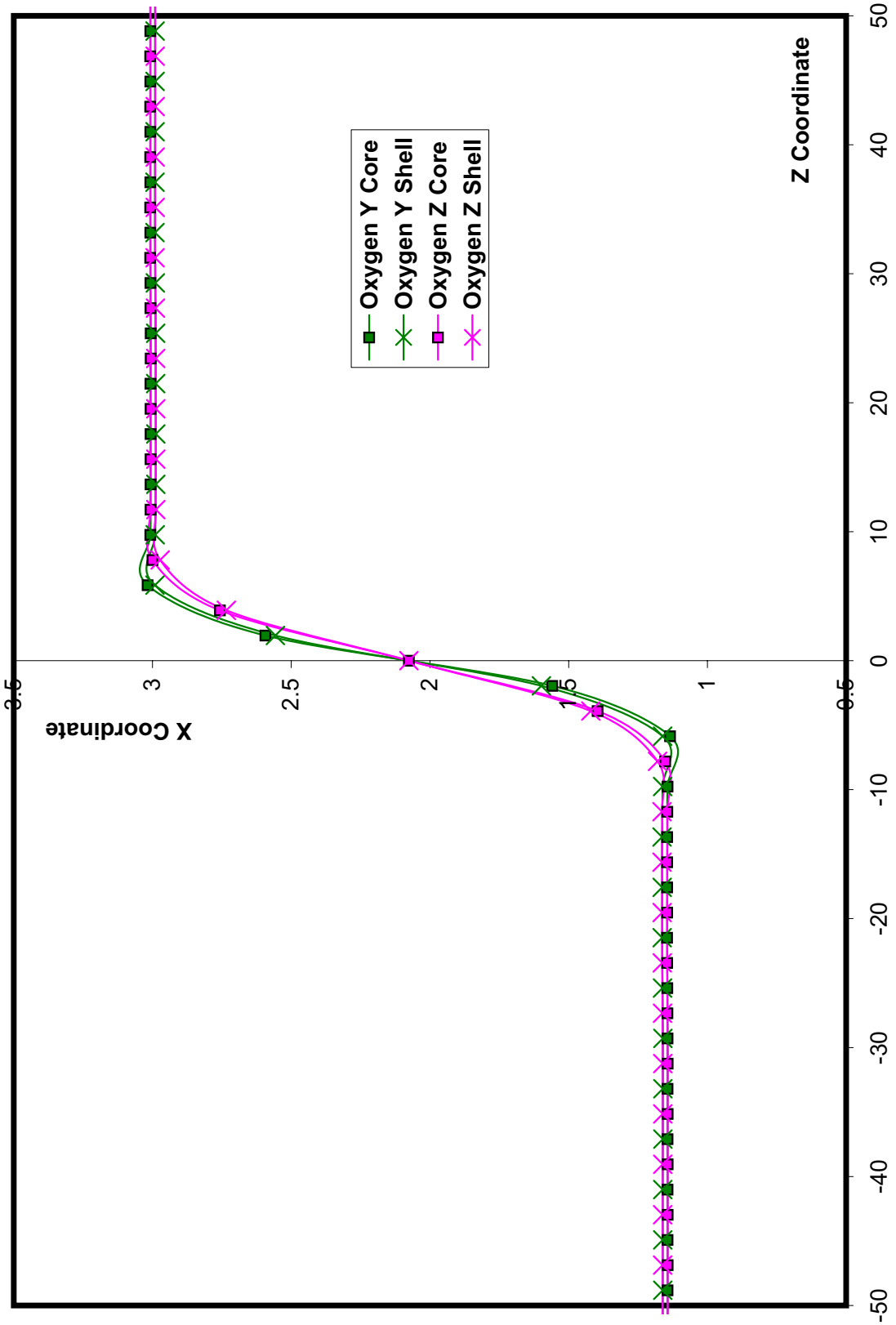

Figure 9.7: Oxygen Y and Oxygen Z core and shell coordinate profiles closer to the wall.

polarization is close to the bulk conditions. Closer to the wall, as Oxygen Z atoms lie directly at the wall and Oxygen Y atoms are further away we observe that the symmetry breaks slightly. It is interesting to notice that here, as in the Lead profiles, Oxygen Y atoms experience a slight kink before transition into the opposite direction, but Oxygen Z atoms do not. These Oxygen atoms have their shells bound much closer to the cores than Oxygen X atoms. Polarizability of Oxygen X atoms is closely related to the phenomena of ferroelectricity in perovskites [111], [169].

In Figure 9.8 we plot the polarization of the unit cells across the wall. Polarization is computed with the same method as mentioned in Chapter 7. The plot shows the polarization value versus the number of the unit cell. Here we can see that the polarization is mostly in its bulk value in all unit cells besides the 3-6 unit cells adjacent to the wall.

9.3 Conclusions

Using the complex lattice Quasicontinuum formulation, we calculated an equilibrium configuration of a 180 degree domain wall in $PbTiO_3$. We used the Sepliarsky et al. potential designed for tetragonal phase $PbTiO_3$.

We were able to simultaneously consider over 400,000 atoms with the Quasicontinuum approach, too large for a possible molecular dynamics atomistics simulation with the same potential, as the non-electrostatic part of the potential is very long reaching.

Our calculations showed that most polarization switching happens in the 2-6 unit cells adjacent to the wall, giving an approximate wall thickness of 1 nm-2.5 nm. This is consistent with recent ab initio calculations and experimental results. In contrast to the ab initio calculations, we were able to consider much larger regions around the domain wall and were able to see long ranging effects from the presence of the wall. We observed a long "tail" of polarization adjustments originating from the wall, extending far into the bulk of the domains.

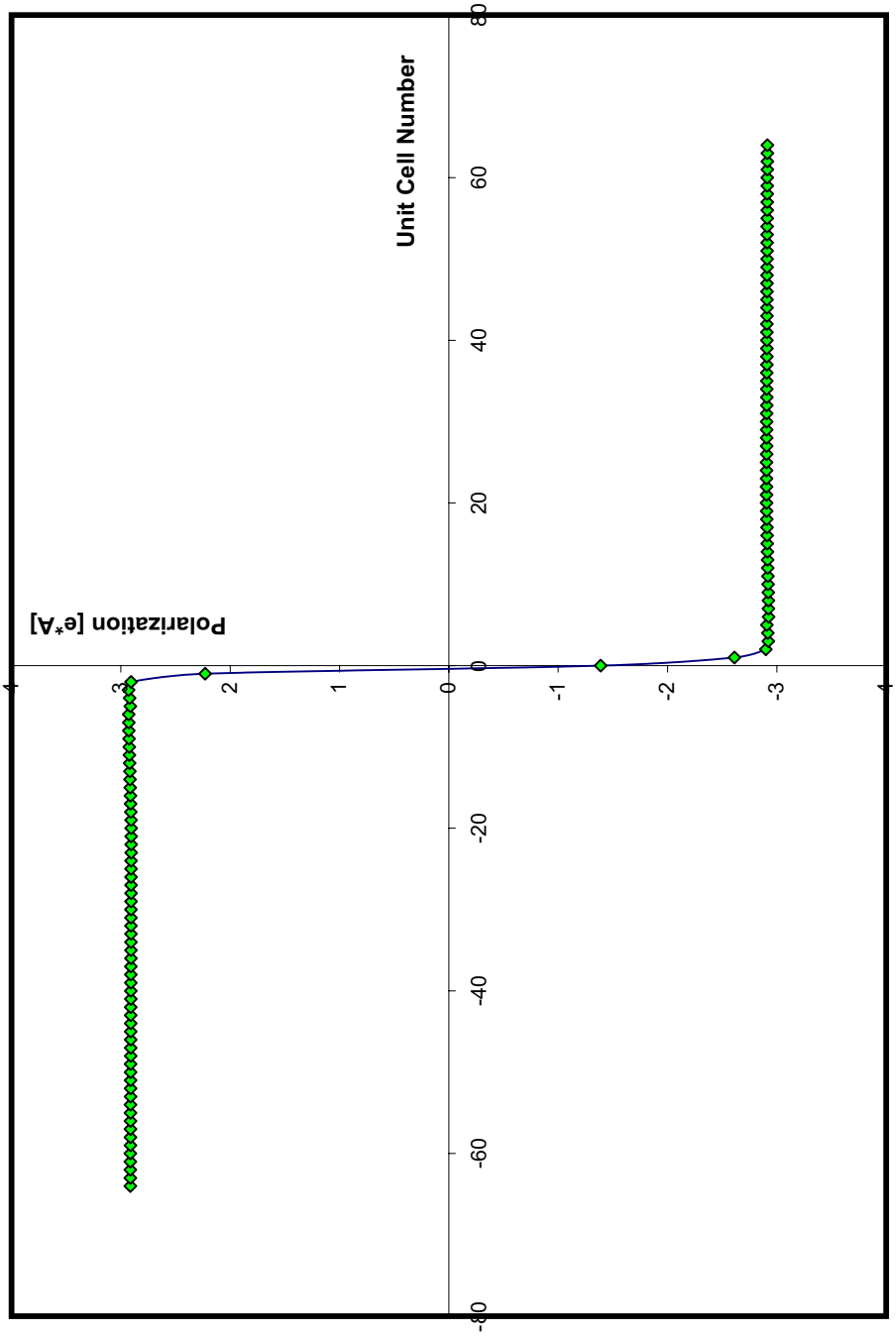

Figure 9.8: Polarization profile of 180 degree wall in $PbTiO_3$.

Chapter 10

Study of 180 Degree Domain Wall Step in $PbTiO_3$ with Sepliarsky et al. Potential

10.1 Motivation

Ferroelectrics are widely used in actuators for many applications. Commercial PZT ceramics do not exhibit an observable electromechanical coupling effect because ceramics are constituted of many domains with random polarization directions such that the average polarization is approximately zero. These samples of ceramics are subjected to a poling process in a strong external electric field to reorient the domains and to create the macroscopically observable electromechanical coupling. This switching of the domains happens due to domain wall movement. Domains contribute to the dielectric, piezoelectric, ferroelectric and elastic properties of the materials by reversible domain wall motions under small electric fields and by irreversible domain wall motions, nucleation and propagation of new domains under stronger electric fields [170], [171], [172], [173], [174]. Thus it is extremely important to fully understand the phenomena of domain switching and domain wall movements to understand ferroelectricity and to design new applications.

It is a well known fact that for most ferroelectrics polarization reversal under the application of an external electrical field of opposite direction proceeds through the sidewise

motion of 180 degree domain walls. Already with Landau-Ginzburg continuum-based energy considerations, the continuum motion of the wall as one unit had been excluded many decades ago [121], [175], [33]. A physical model which appears to explain the experimental results, in particular the velocity of polarization switching and the value of activation electric field [176], [177], [178], [179], was introduced: the nucleation model. This model states that domain wall motion is caused by the nucleation and subsequent growth of reversed small step-like domains on the existing 180 degree wall.

The initial considerations of the nucleation model were introduced by Anderson in 1953 [180], and further developed by Drougard [181] and Abe [182]. The milestone paper which developed and analyzed the model in great detail was published by Miller and Weinreich in 1960 [183]. Their model could explain some experimental data, especially the wall velocity in some electric field ranges, but had to make many simplified assumptions about the process [184].

Since then the model has been further developed, improved and refined. Hayashi [184] worked on the kinetics of domain wall motion analytically and numerically. He was able to derive an expression for the velocity of domain wall in terms of nucleation rate and the sideways growth velocity of the nuclei. He distinguished between two different mechanisms of domain wall propagation depending on the strength of the switching electric field: creation of two-dimensional nuclei at low field strength and one-dimensional nuclei at high fields strength. At low field strength the model predicted the wall velocity and thus the switching rate to be exponentially dependent on the field strength. At high field strength the wall velocity follows a power law as dependent on the field strength.

A somewhat similar continuum approach was used by Sidorkin [185] in investigating domain wall movements and the interactions of domain walls with defects. He determined factors controlling domain wall boundary displacements and bending: lattice potential relief, the original lattice effects, and the long-range electric and elastic fields. He calculated the value of the activation field, separating the regime of creation of only a few nuclei from the

regime of creation of many nuclei. He determined the form and the energy of the critical nuclei corresponding to this separation. He described the mechanism of interaction between domain walls and defects (see also [186]). Many such interactions with charged or elastic defects create a bending of the domain wall with resulting net bounded charges at the flexed surfaces. The actual bending should occur with dislocations and steps appearing at the wall.

Wang and Xiao [187] used a continuum theory to investigate the movement of 180 degree domains in ferroelectrics, and in particular in $BaTiO_3$, as a dynamic process, taking into consideration induced electric and magnetic fields.

A lattice model based on a model of crystal growth by Kolmogorov and Avrami ([188], [189], [190], [191]) was introduced by Ishibashi et al. [192] and [193]. This model follows a polarization vector at each lattice space and can describe polarization switching as influenced by size and surface effects in ferroelectric thin films. The presence of small nuclei is assumed to initiate the switching. Wang and Smith [194] further develop the Ishibashi lattice model to simulate one-dimensional ferroelectric films with a non-ferroelectric boundary. They observe polarization switching as a domain wall propagates in steps from the boundary of the film.

From recent experimental investigations on domain wall movements we would like to mention a paper by Tybell et al. [195] which investigates ferroelectric switching and domain wall dynamics using atom force microscopy (AFM) on monocrystalline $Pb(Zr_{0.2}Ti_{0.8})O_3$ thin films. They used a conductive AFM tip to modify the domain structure. The domains were polarized by application of a voltage pulse across the ferroelectric film, between the AFM tip and the substrate. The size of the domains was then measured by piezoelectric microscopy as a function of pulse duration and amplitude. They also determined the effective activation energy which first creates a nucleus of a new domain larger than the thickness of the system. This data suggests a two-step growth mechanism for domains, in which initial nucleation directly under the AFM tip is followed by domain wall propagation. They observe in their experiments that the domain wall can be pinned by defects, surface effects and an intrinsic periodic pinning potential. They suggest that domain wall movement in ferroelectric thin

films is a creep process, which is a consequence of competition between the elastic energy of the propagating wall and a pinning potential.

Another paper, by Jia and Urban [196], discussed the results of experiments making atomistic resolution measurements of 90 degree domain walls in $BaTiO_3$ thin films using high-resolution imaging at negative spherical aberration of the objective lens in an aberration-corrected transmission electron microscope. These fascinating images reveal, among other things, deformations of the walls due to defects.

The experimental investigations by Ohgami et al. [197] were performed on ferroelectric TGS using atomic force microscopy. They observed evolution of the topography of the surface of the sample. Among other things, they followed the evolution and migration of steps on the domain walls.

To summarize, domain wall step nucleation and propagation plays a very important role in the ferroelectric switching process, which is itself a very important and widely exploited property of ferroelectrics. Continuum theories must make assumptions about the structure, energy and dynamics of domain wall steps to model the switching process, and the parameters of the model are often fit to the experimental data. As mentioned in [198], the governing equations are homogeneous. They do not explicitly depend on position and do not normally give rise to heterogeneous nucleation of new domains. So, the equations need to be modified. A first approach is to add a noise term to the equation, to get domain nucleation. A second approach is to introduce small nuclei at random chosen positions. A third approach is to modify the energy in small, arbitrarily chosen, regions such that the polarization switching is energetically easier in this regions.

Even more detailed microscopically oriented models like lattice models [194] and effective Hamiltonian derived continuum constitutive model [199] simulations still have to introduce initial small steps and domain nuclei to simulate a realistic switching process, otherwise the simulated switching will be homogeneous.

Quasicontinuum studies can bring much of the needed atomistic investigation into study

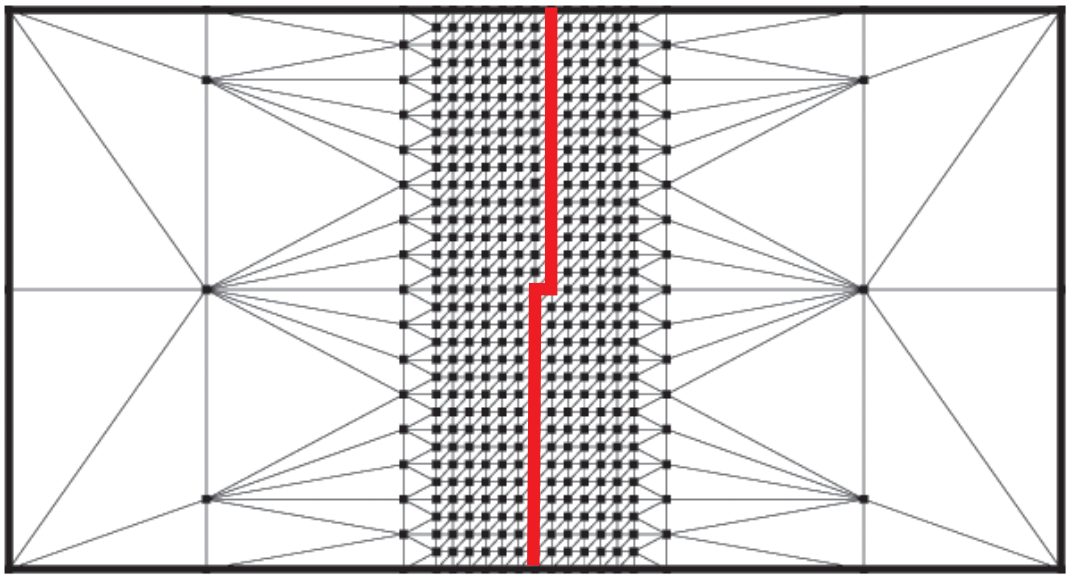

Figure 10.1: Mesh for step calculations in $PbTiO_3$.

of domain wall dynamics and polarization switching problems, while still keeping long-range effects in consideration. We can model the structure and energy of the domain wall boundary and its movement, and not only provide atomistic level insights into the phenomena but also give larger scale simulations the correct mechanisms and parameters for modeling. We first investigate an equilibrium configuration of a step on a 180 degree wall boundary. This is a very important phenomenon to consider as the nucleation of steps is the start of the process of domain movement.

10.2 180 Degree Domain Wall Step Setup and Results

The mesh used for our step calculations is shown in Figure 10.1. The sample chosen for the calculations has dimensions of 33x25x65 unit cells, corresponding to approximately 300,000 atoms. The region of atomistic resolution has 33 unit cells in X direction, 25 unit cells in Y direction. A larger atomistic part in X direction than we used in our wall calculations was introduced since we expected the range of the effects of the step to be relatively large. The wall is perpendicular to the Z direction and this direction has 13 unit cells in atomistic

resolution slowly gradating to coarser resolution further away from the wall.

The step was introduced in the wall at the $X = 0$ and $Z = 0$ location, propagating with the same form in the Y direction. These boundary conditions are chosen to correspond to an infinitely long step on an infinite domain wall between two infinite domains of opposite polarization. The newly created domain boundary is shown in Figure 10.1. The equation for this domain boundary became:

$$(z = 0,\ x < 0) \quad \text{and} \quad (z = \text{STEP},\ x >= 0), \tag{10.1}$$

where x and z are the deformed coordinates of ions (cores and shells) in the symmetric tetragonal structure and STEP is the arbitrary step size in units of lattice parameters or unit cells. This boundary separates two domains with opposite polarization, and the step in the middle of this boundary connects two 180 degree domain walls which are shifted with respect to each other.

These domain walls are Lead centered, this is the stable type as we mentioned in the previous chapter. The ions directly at the boundary of the step in the Figure 10.1 are Lead and Oxygen Z core and shells in the vertical part of the boundary and Lead and Oxygen X core and shells in the small horizontal part of the boundary. In the following calculations we used a step size (STEP) of one unit cell.

We again use the Sepliarsky et al. potential for $PbTiO_3$. The bulk properties of the potential are discussed in the previous chapter. We use the Wolf summation rule with the damping coefficient $\alpha = 0.2$. The electrostatic cutoff radius is set to be $16\mathring{A}$, and the non-electrostatic cutoff radius is set to be $30\mathring{A}$. The parameters of the calculations are similar to the ones used in the previous chapter on domain wall calculations.

The potential is stable in the bulk tetragonal phase only if the movement of ions is constrained to the polarization direction [160]. For our first simulation we constrain the movements of all ions only to the X direction, which is the polarization direction.

The ions are brought into their initial positions, corresponding to the bulk tetragonal phase displacements, building the negative bulk polarization on the right side of the boundary and the positive bulk polarization on the left side of the boundary. The ions directly at the boundary (Lead, Oxygen Z and a few Oxygen X cores and shells directly at the step) are not shifted. All but the surface atoms are allowed to relax in order to find the equilibrium configuration. After some initial simulations we also fixed the atoms directly at the wall, because the potential is highly non-convex and is displaced out of the small convexity area by even the very small change in configuration, required for the initial configuration of the step simulation. Fixing the surface atoms allows the required convexity of the potential in the small area around the initial configuration and the convergence of the simulation. As we restrict the simulations to the polarization direction, we do not expect the constraint of fixing these atoms to affect our results.

The results of this calculation (where the movements of ions is restricted to the polarization direction) are shown in Figure 10.2. A zoom into Figure 10.2 closer to the step is shown in Figure 10.3. The vectors at each node indicate the polarization of the unit cell at those locations (only the Figure 10.3 shows the vector plot). Contour regions are shown corresponding to the X coordinate of the polarization for both Figures.

We observe the bulk tetragonal polarization far away from the domain wall surface, which is indicated by the solid red color on the left part of the sample (positive bulk polarization) and the solid blue color on the right part of the sample (negative bulk polarization). The change happens in only a few (2-6) unit cells adjacent to the wall but far away from the step. This is the same equilibrium condition as in our simulations of a plane 180 degree domain wall in the previous chapter. But it is interesting that the step influences areas further away than the plane 180 degree wall. By comparison, the effects of the step are still quite noticable within a diameter of 8-14 unit cells at the step.

A very interesting feature of our results is that the specimen relaxes in such a way to minimize the net bounded polarization charge on the domain interface. Near the step,

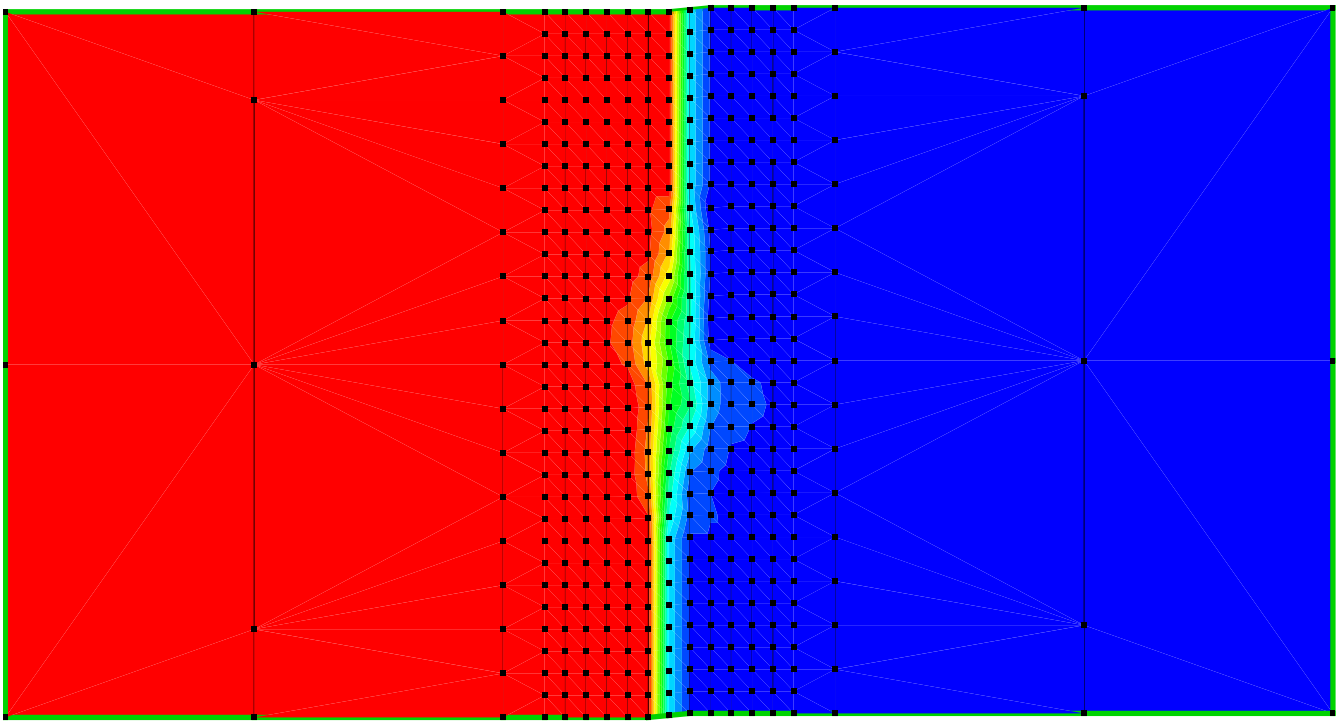

Figure 10.2: Polarization at the step after equilibration (only polarization direction relaxation).

where this interface is horizontal, the X component of the polarization which is normal to the surface at this location vanishes.

These simulations should be considered as a one-dimensional projection of the actual two-dimensional equilibration process at such a step. It is somewhat difficult to imagine a full picture looking at the projection. Therefore we assembled a very similar calculation, but allowed the atoms to relax in two dimensions: in X polarization direction and in Z direction, which is perpendicular to the wall. There should not be any Y direction relaxation as the step and the domain walls extend into infinite Y direction at least in the abstraction of the simulations.

A somewhat unexpected result was that the two-dimensional simulation was able to converge and give an equilibrium configuration even if the bulk tetragonal phase is not absolutely stable in these displacement spaces. But with the limited initial displacements

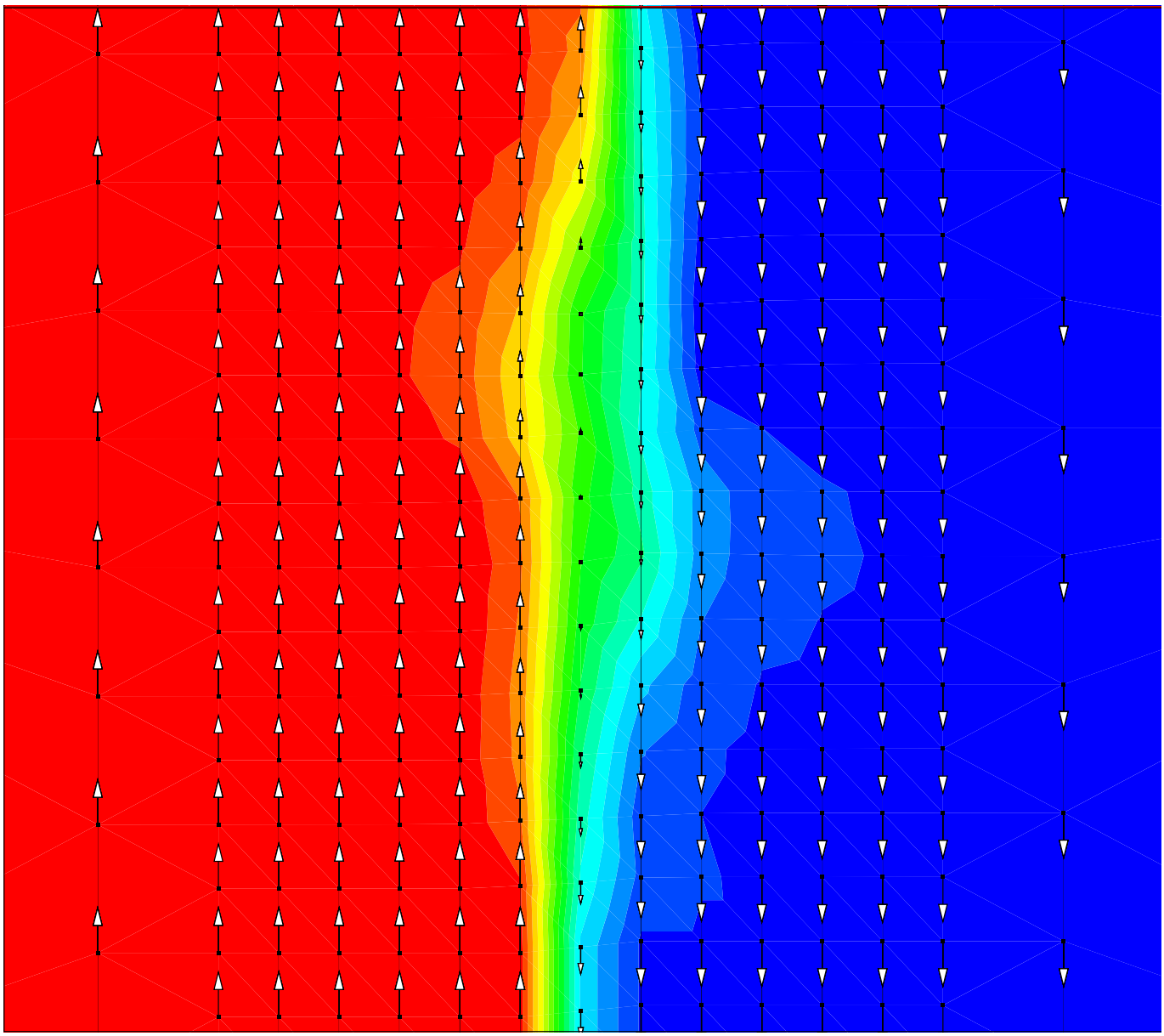

Figure 10.3: Polarization at the step after equilibration, close view (only polarization direction relaxation).

of this particular problem, the two-dimensional step computed with the Sepliarsky et al. potential constitutes a stable problem, where a stable equilibrium configuration can be found. This configuration is shown in Figure 10.4.

In this picture we can see the vectors corresponding to the polarizations of the unit cells and the contour of the polarization X coordinate. Here we can see a large region influenced by the presence of the step. The diameter of the region is 8-14 unit cells. We can also easily see that the system equilibrium configuration tends to smooth out the step and also to smooth out the change of the polarization of the step, making it divergence free as much as possible and thus minimizing the bounded polarization charge at the interface. If we were to allow the boundary unit cells to relax as well, the step would likely disappear because the smooth plane domain interface with no surface charges is an energetically preferred interface between two domains in the absence of defects and external electric or elastic fields [185], [186]. We induce step formation by specifying the boundary conditions at the surface of the sample by two domain walls shifted with respect to each other.

The Figure 10.5 shows the same plot as in Figure 10.4 but with contour levels of Z coordinate of the polarization. We see that the originally zero Z coordinate through entire sample changes signs at the step in a symmetrical pattern. The rest of the sample remains with zero Z direction polarization. The influence of the step defect can be approximated by this plot to be at least 10 unit cells in diameter.

These results are enabled by very detailed modeling at an atomistic resolution (at the vicinity of the step, the continuum part of the Quasicontinuum introduces only some corrections originating from long ranging effects) and are not taken into account by ad hoc adjustments to the model and its parameters as is often the case in continuum calculations. This model does not have any fitting parameters (other than some numerical parameters, sufficient cutoff radiuses and damping potentials, and a fine enough resolution at the defects) which needed to be matched to the experimental results. Instead, it is based entirely on ab initio calculations of atomistic scale interaction within the sample.

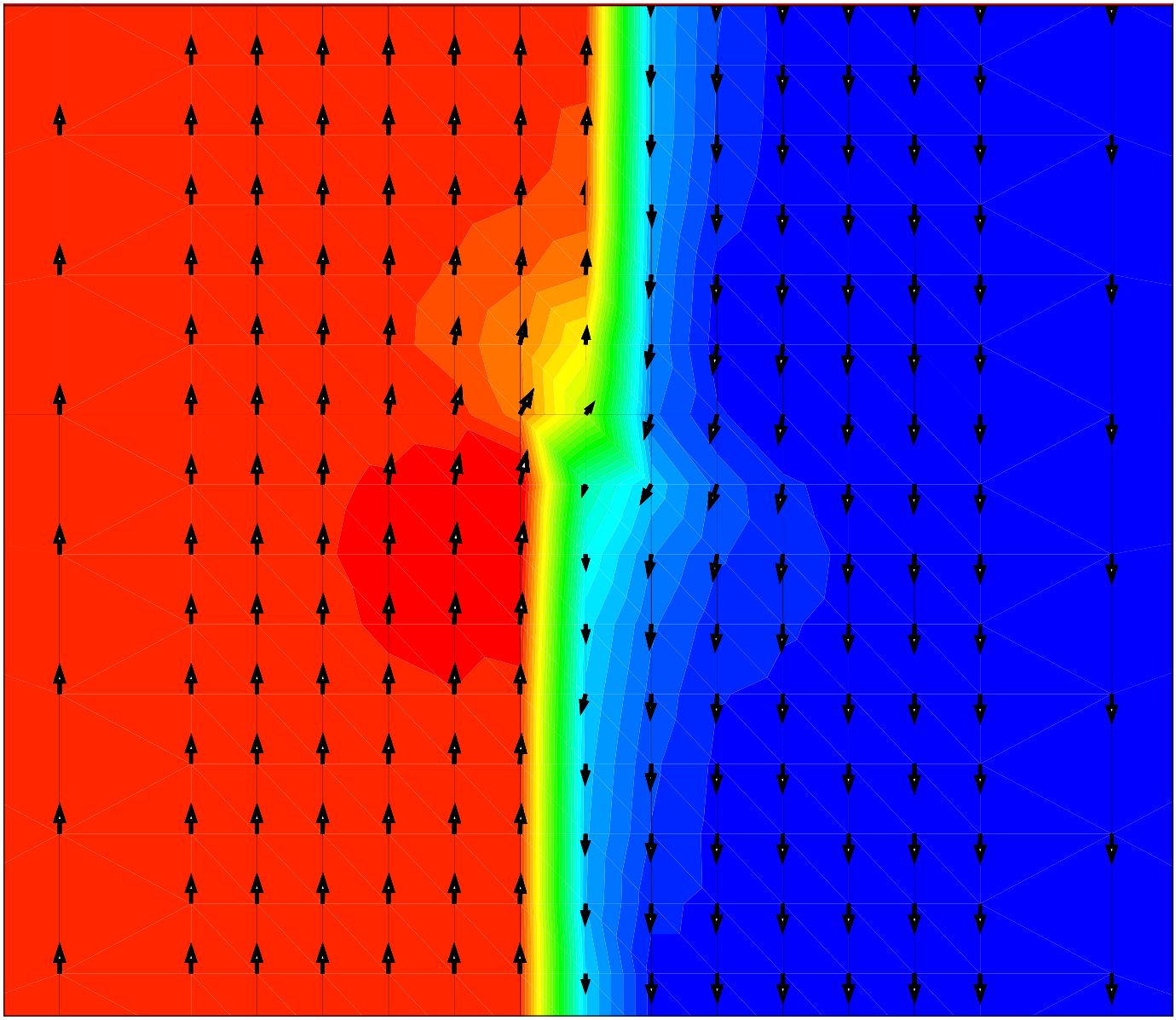

Figure 10.4: Polarization at the step after equilibration, two-dimensional equilibration, X polarization contour.

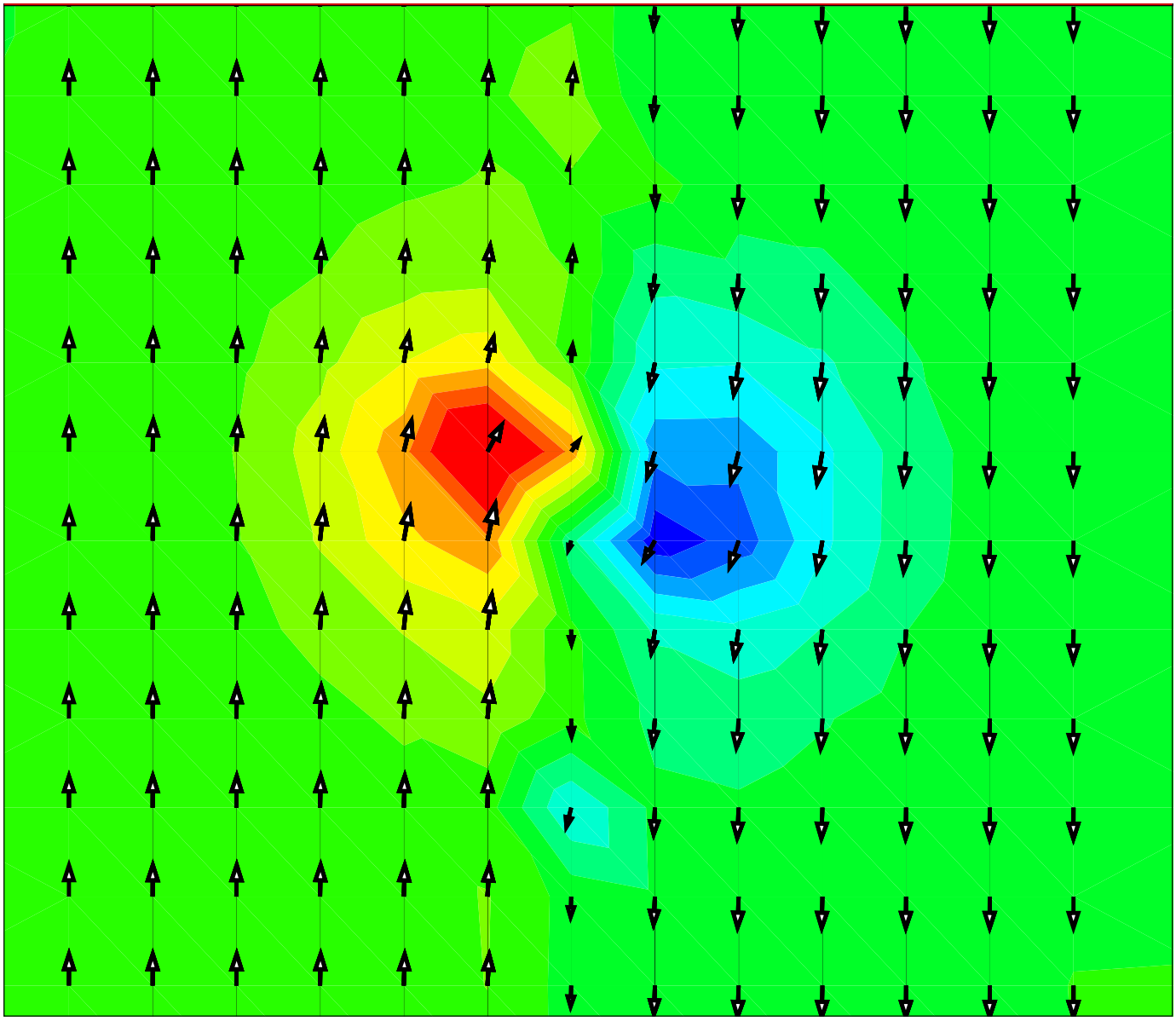

Figure 10.5: Polarization at the step after equilibration, two-dimensional equilibration, Z polarization contour.

10.3 Conclusions

We calculated the equilibrium configuration of a step of one unit cell on a 180 degree domain wall surface in $PbTiO_3$. We calculated the step configuration with relaxation in one-dimension (the polarization direction) and two-dimensions (both polarization direction and the direction perpendicular to the domain wall). We were able to obtain equilibrium configurations in both cases.

The simulations we calculated on an atomistic level of precision give very interesting results. We see that the polarization around the step tends to arrange in a way to minimize the net bounded polarization charge at the interface and smooth out the sharp step transition. Similar activity has been mentioned in the literature before, but only using a large scale continuum approach.

Steps on domain walls are charged defects on an atomistically thin interface which is itself a result of very complicated electromechanical coupling and boundary conditions. To date, it is unclear how to model such systems with continuum theories. Molecular dynamics can consider fine resolution, but misses the long ranging effects which are very important when considering such systems.

Our results could bring much of the needed atomistic scale investigations into study of domain wall dynamics and polarization switching problems. We not only give atomistic level insights into the phenomena but also give the larger scale theories the correct mechanisms and parameters for modeling such phenomena.

Chapter 11

Conclusions

We developed and extended Quasicontinuum theory to be able to model crystals with a complex lattice structure. The interpolation of atoms and approximation of energy and representative forces which were used in Quasicontinuum theory as previously developed could not be used where the crystal consisted of more than one type of atom. We resolved these issues by separating the sample into discrete homogeneous sublattices. We treated each sublattice as separately as possible, with separate representative atoms, separate triangulations, separate shape functions and separate sets of cluster sites. Coupling of the sublattices was accomplished by using the real microscopic forces between the atoms in them, as given by the appropriate potential. This approach of coupling at a very low level of the algorithm substantially reduced the computational effort needed.

We implemented complex lattice Quasicontinuum theory as a C++ extension to existing C code, which itself required extensive modification.

Ferroelectrics are a very good example for the application of complex Quasicontinuum theory. The nature of defects in ferroelectric materials is atomistic, but their influence over the material is long ranged due to induced elastic and electric fields.

We applied complex lattice Quasicontinuum theory in the context of a 180 degree domain wall in $BaTiO_3$. We simulated the equilibrium configuration of a large sample without the need to impose periodic boundary conditions. Our results accorded with experiment and recent ab initio molecular dynamic simulations in showing the atomistic thickness of the

domain wall of between 4-6 unit cells or 1.5-2.5 nm. More than this, we also were able to show long range effects arising from the presence of the wall which molecular dynamics simulations have not been able to do.

We also simulated quasistatic loading of a crack in $BaTiO_3$ using automatic resolution adjustment with increasing crack load. We showed that a systematic pattern of domain layers builds around the crack tip, and that the pattern grows and becomes more distinct with growing crack load. This agrees with experimental results showing an increase in fracture toughness in ferroelectric samples, which is attributed to domain switching near the crack tip.

We then were able to model the equilibrium configuration of a 180 degree domain wall in $PbTiO_3$. We found that the polarization switching occurred in the 2-6 unit cells adjacent to the wall, which indicates that the domain wall thickness is 1 nm to 2.5 nm. While this is in agreement with experiments and recent ab initio molecular dynamics calculations, we were able to calculate much larger regions around the domain wall than possible with molecular dynamics. In doing so, we were able to see a long "tail" of polarization adjustments extending from the domain wall into the bulk of the sample.

Last, we calculated the equilibrium configuration of a step in a 180 degree domain wall in $PbTiO_3$. We were able to show, at an atomistic resolution and also with consideration of long scale effects, an arrangement of polarization around the step which works to minimize the net bounded polarization charge at the interface and smooths out the sharp step transition.

As future directions for application of complex Quasicontinuum theory to ferroelectrics, we would like to suggest simulations of fatigue cracks and indentation in ferroelectrics. Also of a great interest would be research of obstacles and vacancies in ferroelectrics, their dynamics, their interaction with domain walls, surfaces and each other. All of those calculations could be performed with finite temperature, after merging finite temperature with complex lattice Quasicontinuum implementations.

Bibliography

[1] E.B. Tadmor, R. Phillips, and M. Ortiz. Mixed atomistic and continuum models of deformation in solids. *Langmuir*, 12(19):4529–4534, 1996.

[2] E.B. Tadmor, M. Ortiz, and R. Phillips. Quasicontinuum analysis of defects in solids. *Philosophical Magazine A*, 73:1529–1563, 1996.

[3] M. Ortiz, A.M. Cuitino, J. Knap, and M. Koslowski. Mixed atomistic continuum models of material behavior: The art of transcending atomistics and informing continua. *MRS Bulletin*, 26:216–221, 2001.

[4] M. Ortiz and R. Phillips. Nanomechanics of defects in solids. *Advances in Applied Mechanics*, 36:1–79, 1999.

[5] Ronald E. Miller and E.B. Tadmor. The quasicontinuum method: Overview, applications and current directions. *Journal of Computer-Aided Materials Design*, 9:203–239, 2002.

[6] J. Knap and M. Ortiz. An analysis of the quasicontinuum method. *Journal of the Mechanics and Physics of Solids*, 49:1899–1923, 2001.

[7] M.E. Lines and A.M. Glass. *Principles and Applications of Ferrolectrics and Related Materials*. Oxford University Press, New York, 1977.

[8] E.B. Tadmor, G.S. Smith, N. Bernstein, and E. Kaxiras. Mixed finite element and atomistic formulation for complex crystals. *Physical Review B*, 59:235–245, 1999.

[9] P. Zhang, Z. Huang, P.H. Geubelle, P.A. Klein, and K.C. Hwang. The elastic modulus of single-wall carbon nanotubes: a continuum analysis incorporating interatomic potentials. *International Journal of Solids and Structures*, 39:3893–3906, 2002.

[10] Bjarne Stroustrup. *The C++ Programming Language (Special 3rd Edition)*. Addison-Wesley, 2002.

[11] Stanley B. Lippman and Josee LaJoie. *C++ Primer, 3rd Edition*. Addison-Wesley Professional, 1998.

[12] Brian W. Kernighan and Dennis M. Ritchie. *The C Programming Language, Second Edition*. Prentice Hall, Inc., 1988.

[13] J.F. Scott. *Ferroelectric Memories*. Springer-Verlag Berlin Heidelberg, 2000.

[14] H.D. Megaw. Ferroelectricity and crystal structure.2. *Acta Crystallographica*, 7:187–194, 1954.

[15] F. Jona and G. Shirane. *Ferroelectric Crystals*. Pergamon Press, Oxford, 1962.

[16] E. Fatuzzo and W.J. Merz. *Ferroelectricity*. North-Holland, Amsterdam, 1967.

[17] T. Mitsui, I. Tatsuzaki, and E. Nakamura. *An Introduction to the Physics of Ferroelectrics*. Maki-Shoten, Tokyo (english translation: Gordon and Breach, London, 1976), 1969.

[18] Dragan Damjanovic. Ferroelectric, dielectric and piezoelectric properties of ferroelectric thin films and ceramics. *Reports on Progress in Physics*, 61:1267–1324, 1998.

[19] T.M. Shaw, S. Trolier-McKinstry, and P.C. McIntyre. The properties of ferroelectric films at small dimensions. *Annual Review of Matterials Science*, 30:263–298, 2000.

[20] M. Kamlah. Ferroelectric and ferroelastic piezoceramics - modeling of electromechanical hysteresis phenomena. *Continuum Mechanics and Thermodynamics*, 13:219–268, 2001.

[21] Raffaele Resta. Ab initio simulation of the properties of ferroelectric materials. *Modelling and Simulation in Materials Science and Engineering*, 11:R69–R96, 2003.

[22] A.I. Kingon, Streiffer, C. Basceri, and S.R. Summerfelt. High-permittivity perovskite thin films for dynamic random-access memories. *MRS Bulletin*, 21:46–52, 1996.

[23] D.E. Kotecki, J.D. Baniecki, H. Shen, R.B. Laibowitz, and et al. K.L. Saenger. (Ba,Sr)TiO_3 dielectrics for future stacked-capacitor DRAM. *IBM Journal of Research and Development*, 43:367–382, 1999.

[24] O. Auciello, J.F. Scott, and R. Ramesh. The physics of ferroelectric memories. *Physics Today*, 51:22–27, 1998.

[25] R.E. Jones and S.B. Desu. Process integration for nonvolatile ferroelectric: Memory fabrication. *MRS Bulletin*, 21:55–58, 1996.

[26] William A. Goddard III, Qingsong Zhang, Mustafa Uludogan, Alejandro Strachan, and Tahir Cagin. The ReaxFF polarizable reactive force fields for molecular dynamics simulation of ferrolectrics. In *AIP Conference Proceedings*, volume 626, pages 45–55, 2002.

[27] Qingsong Zhang, Tahir Cagin, and William A. Goddard III. Polarizable charge equilibration force field and application to ferroelectrics. in preparation, 2004.

[28] M. Sepliarsky, Z. Wu, A. Asthagiri, and R.E. Cohen. Atomistic model potential for $PbTiO_3$ and PMN by fitting first principles results. To be submitted to Conference Proceedings for EMF 2003, 2003.

[29] D. Wolf, P. Keblinski, S.R. Phillpot, and J. Eggebrecht. Exact method for the simulation of Coulombic systems by spherically truncated, pairwise r^{-1} summation. *Journal of Chemical Physics*, 110(17):8254–8282, 1999.

[30] Lukas M. Eng and H.-J. Güntherodt. Scanning force microscopy and near-field scanning optical microscopy of ferroelectric and ferroelastic domain walls. *Ferroelectrics*, 236:35–46, 2000.

[31] M. Tanaka and G. Honjo. Electron optical studies of Barium Titanate single crystal films. *Journal of the Physical Society of Japan*, 19:954, 1964.

[32] J. Padilla and David Vanderbilt. First-principles investigation of 180 degrees domain walls in $BaTiO_3$. *Physical Review B*, 53(10):R5969–R5973, 1996.

[33] V.A. Zhirnov. A contribution to the theory of domain walls in ferroelectrics. *Soviet Physics JETP-USSR*, 8(5):822–825, 1959.

[34] Robert M. McMeeking. Toward a fracture mechanics for brittle piezoelectric and dielectric materials. *International Journal of Fracture*, 108:25–41, 2001.

[35] G.A. Schneider and V. Heyer. Influence of the electric field on vickers indentation crack growth in $BaTiO_3$. *Journal of the European Ceramic Society*, 19:1299–1306, 1999.

[36] B. Meyer and David Vanderbilt. Ab initio study of ferroelectric domain walls in $PbTiO_3$. *Physical Review B*, 65:104111, 2002.

[37] Y.G. Wang, J. Dec, and W. Kleemann. Surface and domain structures of $PbTiO_3$ crystals studied by atomic force microscopy. *Journal of Applied Physics*, 84:6795–9, 1998.

[38] Gerald Wempner. *Mechanics of Solids and Shells.* CRC Press, 2003.

[39] Y.C. Fung. *Foundations of Solid Mechanics.* Prentice-Hall, Inc., 1965.

[40] Y.C. Fung. *A First Course in Continuum Mechanics.* Prentice-Hall, Inc., 1977.

[41] Pei Chi Chou and Nicholas J. Pagano. *Elasticity. Tensor, Dyadic, and Engineering Approach.* D. Van Nostrand Company, Inc., 1967.

[42] Charles Kittel. *Introduction to solid state physics.* Wiley, New York, 1996.

[43] Gerd Otter and Raimund Honecker. *Atome, Molekuele, Kerne I. Atomphysik.* Teubner Verlag, 1993.

[44] Gerd Otter and Raimund Honecker. *Atome, Molekuele, Kerne, Bd. 2, Molekuelphysik und Kernphysik.* Teubner Verlag, 1997.

[45] V.B. Shenoy, R. Miller, E.B. Tadmor, D. Rodney, R. Phillips, and M. Ortiz. An adaptive finite element approach to atomic-scale mechanics - the quasicontinuum method. *Journal of the Mechanics and Physics of Solids*, 47:611–642, 1999.

[46] V.B. Shenoy, R. Miller, E.B. Tadmor, R. Phillips, and M. Ortiz. Quasicontinuum models of interfacial structure and deformation. *Physical Review Letters*, 80:742–745, 1998.

[47] R. Miller, E.B. Tadmor, R. Phillips, and M. Ortiz. Quasicontinuum simulation of fracture at the atomic scale. *Modelling and Simulation in Materials Science and Engineering*, 6:607–638, 1998.

[48] R. Miller, M. Ortiz, R. Phillips, V.B. Shenoy, and E.B. Tadmor. Quasicontinuum models of fracture and plasticity. *Engineering Fracture Mechanics*, 61:21–48, 1998.

[49] D. Rodney and R. Phillips. Structure and strength of dislocation junctions: An atomic level analysis. *Physical Review Letters*, 82:1704–1707, 1999.

[50] E.B. Tadmor, R. Miller, R. Phillips, and M. Ortiz. Nanoindentation and incipient plasticity. *Journal od Materials Research*, 14:2233–2250, 1999.

[51] Vivek Shenoy, R. Phillips, and E.B. Tadmor. Nucleation of dislocations beneath a plane strain indenter. *Journal od the Mechanics and Physics od Solids*, 48:649–673, 2000.

[52] G.S. Smith, E.B. Tadmor, and E. Kaxiras. Multiscale simulation of loading and electrical resistance in silicon nanoindentation. *Physical Review Letters*, 84:1260–1263, 2000.

[53] J. Knap and M. Ortiz. Effect of indenter-radius size on Au(001) nanoindentation. *Physical Review Letters*, 90:226102, 2003.

[54] Vijay B. Shenoy. Multi-scale modeling strategies in material science - the quasicontinuum method. *Bulletin of Materials Science*, 26:53–62, 2003.

[55] www.qcmethod.com. WWW site for quasicontinuum method resources.

[56] S.P. Timoshenko and J.N. Goodier. *Theory of Elasticity.* McGraw-Hill Book Company, 1970.

[57] J. Beck. Engineering mathematical principles class notes. 2000-2001.

[58] I.S. Sokolnikoff. *Mathematical Theory of Elasticity.* McCraw-Hill Book Company, Inc., 1956.

[59] Christian Gerthsen and Helmut Vogel. *Physik.* Springer-Lehrbuch, 1997.

[60] O.C. Zienkiewicz. *The Finite Element Method, Volume 1-2.* McGraw-Hill, London, 1991.

[61] J.N. Reddy. *An Introduction to the Finite Element Method.* McGraw-Hill, Inc., 1984.

[62] Thomas J.R. Hughes. *The Finite Element Method. Linear Static and Dynamic Finite Element Analysis.* Dover Publications, 2000.

[63] Robert D. Cook. *Concepts and Applications of Finite Element Analysis.* John Wiley and Sons, 1981.

[64] Stephen P. Timoshenko and James M. Gere. *Mechanics of Materials.* D. Van Nostrand Company, 1972.

[65] Alexander L. Walecka and J. Fetter. *Quantum Theory of Many-Particle Systems (International Series in Pure and Applied Physics.* McGraw-Hill College, 1971.

[66] E. Schrödinger. Die erfüllbarkeit der relativitätsforderung in der klassischen mechanik. *Annalen der Physik*, 77:325–336, 1925.

[67] E. Schrödinger. Quantisierung als eigenwertproblem (zweite mitteilung). *Annalen der Physik*, 79:489–527, 1926.

[68] E. Schrödinger. Quantisierung als eigenwertproblem (dritte mitteilung: Störungtheorie, mit anwendung auf den starkeffect der balmerlinien. *Annalen der Physik*, 80:437–490, 1926.

[69] E. Schrödinger. Quantisierung als eigenwertproblem (vierte mitteilung). *Annalen der Physik*, 81:109–139, 1926.

[70] L. de Broglie. *Nature*, 112:540, 1923.

[71] P.A.M. Dirac. The quantum theory of the emission and absorption of radiation. *Proceedings of the Royal Society London*, A114:243, 1927.

[72] P.A.M. Dirac. The quantum theory of the electron. *Proceedings of the Royal Society London*, A117:610, 1928.

[73] P.A.M. Dirac. *The Principles of Quantum Mechanics.* Oxford, Clarendon Press, 1930.

[74] M. Born. On quantum mechanics II. *Zeitschrift fü Physik*, 35:557, 1926.

[75] W. Heisenberg. Ueber den anschaulichen inhalt der quantentheoretischen kinematik and mechanik. *Zeitschrift fü Physik*, 43:172–198, 1927.

[76] N. Bohr. Das quantenpostulat und die neuere entwicklung der atomphysik. *Die Naturwissenschaften*, 16:239–255, 1928.

[77] N. Bohr. Wirkungsquantum und naturbeschreibung. *Die Naturwissenschaften*, 17:483–486, 1929.

[78] Albert Messiah. *Quantum Mechanics, Volume I.* North-Holland, Amsterdam, 1961.

[79] L.D. Landau and E.M. Lifshitz. *Quantum Mechanics, non-relativistic theory.* Pergamon Press LTD., 1958.

[80] David Bohm. *Quantum Theory.* Prentice-Hall, Inc., 1951.

[81] Julian D. Gale and Andrew L. Rohl. The general utility lattice program (GULP). *Molecular Simulation*, 29:291–341, 2003.

[82] J. D. Gale. Empirical potential derivation for ionic materials. *Philosophical Magazine*, 73:3–19, 1994.

[83] Jerome L. Rosenberg and Lawrence Epstein. *Schaum's Outline of College Chemistry.* McGraw-Hill, 1996.

[84] N.W. Ashcroft and D. Mermin. *Solid State Physics.* International Thomson Publishing, 1976.

[85] Scott L. Needham and David L. Dowe. Message length as an effective Ockham's razor in decision tree induction. In *Proc. 8th International Workshop on Artificial Intelligence and Statistics*, pages 253–260, 2001.

[86] Stanley B. Lippman. *Essential C++.* Addison Wesley Longman, 2000.

[87] Herbert Edelsbrunner, P.G. Ciarlet, A. Iserles, R.V. Kohn, and M.H. Wright. *Geometry and Topology for Mesh Generation (Cambridge Monographs on Applied and Computational Mathematics*. Cambridge University Press, 2001.

[88] B. Joe. GEOMPACK – a software package for the generation of meshes using geometric algorithms. *Advances in Engineering Software and Workstations*, 13:325–331, 1991.

[89] Jonathan Richard Shewchuk. An introduction to the conjugate gradient method without the agonizing pain. Unpublished notes, 1994.

[90] A.K. Rappe and W.A. Goddard III. Charge equilibration for molecular dynamics simulations. *Journal of Physical Chemistry*, 95:3358–3363, 1991.

[91] Z. Gong and R.E. Cohen. Molecular dynamics study of $PbTiO_3$ using non-empirical potentials. *Ferroelectrics*, 136:113–124, 1992.

[92] P. Ghosez, E. Cockane, U. Waghmare, and K. Rabe. Lattice dynamics of $BaTiO_3$, $PbTiO_3$, and $PbZrO_3$: A comparative first-principles study. *Physical Review B*, 60:836–843, 1999.

[93] P.P. Ewald. Die berechnung optischer und elektrostatischer gitterpotentiale. *Annalen der Physik (Leipzig)*, 64:253–287, 1921.

[94] H.M. Evjen. On the stability of certain heteropolar crystals. *Physical Review*, 39:675–687, 1932.

[95] D.E. Parry. The electrostatic potential in the surface region of an ionic crystal. *Surface Science*, 49(2):433–440, 1975.

[96] D.E. Parry. Correction. *Surface Science*, 54(1):195–195, 1976.

[97] L Greengard and V. Rokhlin. A fast algorithm for particle simulations. *Journal of Computational Physics*, 73:325–348, 1987.

[98] L. Greengard. Fast algorithms for classical physics. *Science*, 265(5174):909–914, 1994.

[99] H.Y. Wang and R. LeSar. An efficient fast-multipole algorithm based on an expansion in the solid harmonics. *Journal of Chemical Physics*, 104(11):4173–4179, 1996.

[100] E. Madelung. Das electrische feld in systemen von regelmaessig angeordneten punktladungen. *Physikalische Zeitshrift*, 19:524, 1918.

[101] J.H.R. Clarke, W. Smith, and L.V. Woodcock. Short range effective potentials for ionic fluids. *Journal of Chemical Physics*, 84(4):2290–2294, 1986.

[102] L.V. Woodcock. *Advances in Molten Salt Chemistry.* Plenum, New York, 1975.

[103] O. Emersleben. Über die konvergenz der reihen epsteinscher zetafunktionen. *Mathematische Nachrichten*, 4:468–480, 1951.

[104] E. Wainer and A.N. Salomon. *Titanium Alloy Manufacturing Company, Elec. Rep.*, 8, 1942.

[105] F. Jona and G. Shirane. *Ferroelectric Crystals.* Dover Publications, New York, 1993.

[106] B. Jaffe. *Piezoelectric ceramics, (Non-metallic solids).* Academic Press, 1971.

[107] Q.M. Zhang, J. Zhao, T. Shrout, N. Kim, L.E. Cross, A. Amin, and B.M. Kulwicki. Characteristics of the electromechanical response and polarization of electric-field biased ferroelectrics. *Journal of Applied Physics*, 77:2549–2555, 1995.

[108] H.F. Cheng. Structural and optical properties of laser deposited ferroelectric $(Sr_{0.2}Ba_{0.8})TiO_3$ thin films. *Journal of Applied Physics*, 79:7965–7971, 1996.

[109] A.D. Hilton and B.W. Ricketts. Dielectric properties of $Ba_{1-x}Sr_xTiO_3$ ceramics. *Journal of Physics D- Applied Physics*, 29:1321–1325, 1996.

[110] R.N. Schwartz, B.A. Wechsler, and R.A. McFarlane. Photo-EPR study of light-sensitive impurity and defect centers in photorefractive $BaTiO_3$. *Physical Review B*, 46:3263–3272, 1992.

[111] A.F. Devonshire. Theory of barium titanate. part I. *Philosophical Magazine*, 40:1040–1063, 1949.

[112] A.F. Devonshire. Theory of barium titanate. part II. *Philosophical Magazine*, 42:1065–1079, 1951.

[113] H.D. Megaw. Crystal structure of Barium Titanate. *Nature*, 155:484–485, 1945.

[114] Y.C. Shu and K. Bhattacharya. Domain patterns and macroscopic behavior of ferroelectric materials. *Philosophical Magazine B*, 81:2021–2054, 2001.

[115] J. Fousek and V. Janovec. Orientation of domain walls in twinned ferroelectric crystals. *Journal of Applied Physics*, 40:135, 1969.

[116] S. Tinte, M.G. Stachiotti, M. Sepliarsky, R.L. Migoni, and C.O. Rodriguez. Atomistic modeling of $BaTiO_3$ based on first-principles calculations. *Journal of Physics - Condensed Matter*, 11:9679–9690, 1999.

[117] S. P*ö*ykk*ö* and D.J. Chadi. Ab initio study of 180 degrees domain wall energy and structure in $PbTiO_3$. *Applied Physics Letters*, 75:2830–2832, 1999.

[118] S. P*ö*ykk*ö* and D.J. Chadi. Ab initio study of dipolar defects and 180° domain walls in $PbTiO_3$. *Journal of Physics and Chemistry of Solids*, 61:291–294, 2000.

[119] W.N. Lawless. 180 degrees domain-wall energies in $BaTiO_3$. *Physical Review*, 175:619, 1968.

[120] Walter J. Merz. Domain properties in $BaTiO_3$. *Physical Review*, 88(2):421–422, 1952.

[121] Walter J. Merz. Domain formation and domain wall motions in ferroelectric $BaTiO_3$ single crystals. *Physical Review*, 95(3):690–698, 1954.

[122] N. Floquet, C.M. Valot, M.T. Mesnier, J.C. Niepce, L. Normand, A. Thorel, and R. Kilaas. Ferroelectric domain walls in $BaTiO_3$: Fingerprints in XRPD diagrams and quantitative HRTEM image analysis. *J Phys. III France*, 7:1105–1128, 1997.

[123] S. Stemmer, S.K. Streiffer, F. Ernst, and M. Ruehle. Atomistic structure of 90° domain walls in ferroelectric $PbTiO_3$ thin films. *Philosophical Magazine A*, 71:713–724, 1995.

[124] M. Foeth, A. Sfera, P. Stadelmann, and P.-A. Buffat. A comparison of HREM and weak beam transmission electron microscopy for the quantitative measurements of the thickness of ferroelectric domain walls. *Journal of Electron Microscopy*, 48:717–723, 1999.

[125] J. Fousek and M. Safrankova. On equilibrium domain structure of $BaTiO_3$. *Japanese Journal of Applied Physics*, 4:403, 1965.

[126] L.N. Bulaevskii. Thermodynamic theory of domain walls in ferroelectric materials with the perovskite structure. *Soviet Physics - Solid State*, 5:2329–2332, 1964.

[127] T.-Y. Zhang, M.H. Zhao, and P. Tong. Fracture of piezoelectric ceramics. *Advances in Applied Mechanics*, 38:147–289, 2002.

[128] G.G. Pisarenko, V.M. Chushko, and S.P. Kovalev. Anisotropy of fracture-toughness of piezoelectric ceramics. *Journal of the American Ceramic Society*, 68(5):259–265, 1985.

[129] K. Mehta and A.V. Virkar. Fracture mechanisms in ferroelectric-ferroelastic lead zirconate titanate [Zr-Ti=0.54-0.46] ceramics. *Journal of the American Ceramic Society*, 73(3):567–574, 1990.

[130] Z. Zhang and R. Raj. Influence of grain size on ferroelastic toughening and piezoelectric behavior of lead zirconate titanate. *Journal of the American Ceramic Society*, 78(12):3363–3368, 1995.

[131] C.S. Lynch, L. Chen, Z. Suo, R.M. McMeeking, and W. Yang. Crack growth in ferroelectric ceramics driven by cyclic polarization switching. *Journal of Intelligent Material Systems and Structures*, 6:191–198, 1995.

[132] F. Meschke, A. Kolleck, and G.A. Schneider. R-curve behaviour of $BaTiO_3$ due to stress-induced ferroelastic domain switching. *Journal of the European Ceramic Society*, 17:1143–1149, 1997.

[133] F. Guiu, B.S. Hahn, H.L. Lee, J.M. Caderon, and M.J. Reece. Growth of indentation cracks in poled and unpoled PZT. *Journal of the European Ceramic Society*, 17:5025–512, 1997.

[134] A. Kolleck, G.A. Schneider, and F.A. Meschke. R-curve behavior of $BaTiO_3$- and PZT ceramics under the influence of an electric field applied parallel to the crack front. *Acta Materialia*, 48:4099–4113, 2000.

[135] S.L. dos Santos e Lucato, J. Lindner, D.C. Lupascu, and J. Rodel. Influence of electrical and geometrical boundary conditions on crack growth in PZT. *Key Engineering Materials*, 206:609–612, 2002.

[136] F. Fang and W. Yang. Indentation-induced cracking and 90° domain switching pattern in barium titanate ferroelectric single crystals under different poling. *Materials Letters*, 57:198–202, 2002.

[137] S. Hackemann and W. Pfeiffer. Domain switching in process zones of PZT: characterization by microdiffraction and fracture mechanical methods. *Journal of the European Ceramic Society*, 23:141–151, 2003.

[138] G.A. Schneider, F. Felten, and R.M. McMeeking. The electrical potential difference across cracks in PZT measured by Kelvin Probe Microscopy and the implications for fracture. *Acta Materialia*, 51:2235–2241, 2003.

[139] R. Niefanger, V.-B. Pham, G.A. Schneider, H.-A. Bahr, H. Balke, and U. Bahr. Quasi-static straight and oscillatory crack propagation in ferroelectric ceramics due to moving electric field: experiments and theory. *Acta Materialia*, 52:117–127, 2004.

[140] Chad M. Landis and Robert M. McMeeking. A self-consistent constitutive model for switching in polycrystalline barium titanate. *Ferroelectrics*, 255:13–34, 2001.

[141] H.G. Beom and S.N. Atluri. Effect of electric fields on fracture behaviour of ferroelectric ceramics. *Journal of the Mechanics and Physics of Solids*, 51:1107–1125, 2003.

[142] K.M. Jeong and H.G. Beom. Conducting crack growth in ferroelectric ceramics subjected to electric loading. *Smart Materials and Structures*, 13:275–282, 2004.

[143] Jianxin Wang and Chad M. Landis. On the fracture toughness of ferroelectric ceramics with electric field applied parallel to the crack front. *Acta Materialia*, 52:3435–3446, 2004.

[144] T.L. Anderson. *Fracture Mechanics, Fundamentals and Applications*. CRC Press, 1995.

[145] D. Berlincourt and H. Jaffe. Elastic and piezoelectric coefficients of single-crystal barium titanate. *Physical Review*, 111:143–148, 1958.

[146] T. Ishidate and S. Sasaki. Coupled acoustic modes in tetragonal $BaTiO_3$. *Journal of the Physical Society of Japan*, 56:4214–4217, 1987.

[147] M. Zgonik, P. Bernasconi, M. Duelli, R. Schlesser, P. Guenter, M.H. Garrett, D. Rytz, Y. Zhu, and X. Wu. Dielectric, elastic, piezoelectric, electro-optic, and elasto-optic tensors of $BaTiO_3$ crystals. *Physical Review B*, 50(9):5941–5949, 1994.

[148] K. Bhattacharya. Mechanics of structures and solids class notes. 2000-2001.

[149] J.F. Nye. *Physical Properties of Crystals*. Clarendon, Oxford, 1957.

[150] O. Beckstein, J.E. Klepeis, G.L.W. Hart, and O. Pankratov. First-principles elastic constants and electronic structure of alpha-Pt_2Si and PtSi. *Physical Review B*, 63:134112, 2001.

[151] J. Harada, J.D. Axe, and G. Shirane. Neutron-scattering study of soft modes in cubic $BaTiO_3$. *Physical Review B*, 4:155, 1971.

[152] H. Takahasi. A note on theory of Barium Titanate. *Journal of the Physical Society of Japan*, 16:1685, 1961.

[153] Zhao-Xu Chen, Yi Chen, and Yuan-Sheng Jiang. Comparative study of ABO_3 perovskite compounds. 1. $ATiO_3$ (A=Ca, Sr, Ba, and Pb) perovskites. *The Journal of Physical Chemistry B*, 106:9986–9992, 2002.

[154] Ronald E. Cohen and Henry Krakauer. Electronic structure studies of the differences in ferroelectric behavior of $BaTiO_3$ and $PbTiO_3$. *Ferroelectrics*, 136:65–83, 1992.

[155] L.F. Mattheiss. Energy-bands for $KNiF_3$, $SrTiO_3$, $KMoO_3$, and $KTaO_3$. *Physical Review B*, 6:4718–4740, 1972.

[156] R.E. Cohen. Origin of ferroelectricity in perovskite oxides. *Nature*, 358:136–138, 1992.

[157] Kaoru Miura and Masahiro Tanaka. Electronic structures of $PbTiO_3$: I. covalent interaction between Ti and O ions. *Japanese Journal of Applied Physics*, 37:6451–6459, 1998.

[158] Kaoru Miura and Masahiro Tanaka. Electronic structures of $PbTiO_3$: II. properties of Pb ion displacement. *Japanese Journal of Applied Physics*, 37:6460–6464, 1998.

[159] Kunio Nishida, Shigeharu Kasai, Katsuhiko Tanaka, Yukio Sakabe, Fumiyuki Ishii, and Tamio Oguchi. First-principles studies on elastic and spontaneous polarizations of $PbTiO_3$. *Japanese Journal of Applied Physics*, 40:5806–5808, 2001.

[160] A. Yavari. private communication, 2004.

[161] J. Marian. private communication, 2004.

[162] A. Gordon. Tricritical phase-transitions in ferroelectrics. *Physica*, 122B:321–332, 1983.

[163] Wenwu Cao and L.E. Cross. Theory of tetragonal twin structures in ferroelectric perovskites with a 1st-order phase transition. *Physical Review B*, 44:5–12, 1991.

[164] P. Lehnen, J. Dec, and W. Kleemann. Ferroelectric domain structures of $PbTiO_3$ studied by scanning force microscopy. *Journal of Physics D - Applied Physics*, 33:1932–1936, 2000.

[165] X.R. Huang, X.B. Hu, S.S. Jiang, and D. Feng. Theoretical model of 180° domain-wall structures and their transformation in ferroelectric perovskites. *Physical Review B*, 55(9):5534–5537, 1997.

[166] P. Hohenberg and W. Kohn. Inhomogeneous electron gas. *Physical Review B*, 136:B864, 1964.

[167] D.M. Ceperley and B.J. Alder. Ground-state of the electron-gas by a stochastic method. *Physical Review Letters*, 45:566–569, 1980.

[168] D. Vanderbilt. Soft self-consistent pseudopotentials in a generalized eigenvalue formalism. *Physical Review B*, 41:7892–7895, 1990.

[169] J.C. Slater. The Lorentz correction in Barium Titanate. *Physical Review*, 78:748–761, 1950.

[170] G. Arlt, H. Dederichs, and R. Herbiet. 90°-domain wall relaxation in tetragonally distorted ferroelectric ceramics. *Ferroelectrics*, 74:37–53, 1987.

[171] S. Li, W. Cao, and L. Cross. The extrinsic nature of nonlinear behavior observed in lead zirconate titanate ceramic. *Journal of Applied Physics*, 69:7219–7224, 1991.

[172] E. Burcsu, G. Ravichandran, and K. Bhattacharya. Large strain electrostrictive actuation in barium titanate. *Applied Physics Letters*, 77:1698–1700, 2000.

[173] E. Burcsu, G. Ravichandran, and K. Bhattacharya. Large electrostrictive actuation of barium titanate single crystals. *Journal of the Mechics and Physics of Solids*, 52:823–846, 2004.

[174] F. Xu, S. Trolier-McKinstry, W. Ren, Baomin Xu, Z.-L. Xie, and K.J. Hemker. Domain wall motion and its contribution to the dielectric and piezoelectric properties of lead zirconate titanate films. *Journal of Applied Physics*, 89:1336–1348, 2001.

[175] W. Kinase and H. Takahasi. On the 180-degrees-type domain wall of $BaTiO_3$ crystal. *Journal of the Physical Society of Japan*, 12:464–476, 1957.

[176] R.C. Miller and A. Savage. Velocity of sidewise 180-degrees domain-wall motion in $BaTiO_3$ as afunction of the applied electric field. *Physical Review*, 112:755–762, 1958.

[177] C.F. Pulvari and W. Kuebler. Phenomenological theory of polarization reversal in $BaTiO_3$ single crystals. *Journal of Applied Physics*, 29:1315–1321, 1958.

[178] E. Fatuzzo and W.J. Merz. Switching mechanism in triglycine sulfate and other ferroelectrics. *Physical Review*, 116:61–68, 1959.

[179] R.C. Miller and A. Savage. Further experiments on the sidewise motion of 180-degrees domain walls in $BaTiO_3$. *Physical Review*, 115:1176–1180, 1959.

[180] P.W. Anderson. Unpublished notes, 1953.

[181] M.E. Drougard. Detailed study of switching current in barium titanate. *Journal of Applied Physics*, 31:352–355, 1960.

[182] R. Abe. Theoretical treatment of the movement of 180-degrees domain in $BaTiO_3$ single crystal. *Journal of the Physical Society of Japan*, 14:633–642, 1959.

[183] Robert C. Miller and Gabriel Weinreich. Mechanism for the sidewise motion of 180° domain walls in barium titanate. *Physical Review*, 117:1460–1466, 1960.

[184] Mitsuhiko Hayashi. Kinetics of domain wall motion in ferroelectric switching. I. general formulation. *Journal of the Physical Society of Japan*, 33:616–628, 1972.

[185] Alexander Sidorkin. Dynamics of domain walls in ferroelectrics and ferroelastics. *Ferroelectrics*, 191:109–128, 1997.

[186] A. S. Sidorkin and A.A. Shevchenko. The interaction of domain wall in ferroelectric-ferroelastic crystal with dilatation center. *Ferroelectrics*, 141:235–242, 1993.

[187] Biao Wang and Zhongmin Xiao. On the dynamic growth of a 180° domain in a ferroelectric material. *Journal of Applied Physics*, 88:1464–1472, 2000.

[188] A.K. Kolmogorov. Statistical theory of crystallization in metals. *Bulletin Acad. Sci. USSR Mat. Sci.*, 1:355–359, 1937.

[189] M. Avrami. Kinetics of phase change I. *Journal of Chemical Physics*, 7:1103–1112, 1939.

[190] M. Avrami. Kinetics of phase change II. *Journal of Chemical Physics*, 8:212–224, 1940.

[191] M. Avrami. Kinetics of phase change III. *Journal of Chemical Physics*, 9:177–184, 1941.

[192] Y. Ishibashi. Theory of polarization reversals in ferroelectrics based on Landau-type free-energy. *Japanese Journal of Applied Physics Part 1-Regular Papers Short Notes and Review Papers*, 31:2822–2824, 1992.

[193] H. Orihara and Y. Ishibashi. A statistical-theory of nucleation and growth in finite systems. *Journal of the Physical Society of Japan*, 61:1919, 1992.

[194] C.L. Wang and S.R.P. Smith. The size effect on the switching properties of ferroelectric films: a one-dimensional lattice model. *Journal of Physics: Condensed Matter*, 8:4813–4822, 1996.

[195] T. Tybell, P. Paruch, T. Giamarchi, and J.-M. Triscone. Domain wall creep in epitaxial ferroelectric $Pb(Zr_{0.2}Ti_{0.8})O_3$ thin films. *Physical Review Letters*, 89:(097601)1–4, 2002.

[196] C.L. Jia and K. Urban. Atomic-resolution measurement of oxygen concentration in oxide materials. *Science*, 303:2001–2004, 2004.

[197] Junji Ohgami, Yasuhiro Sugawara, Seizo Morita Eiji Nakamura, and Toru Ozaki. Time evolution of surface topography around a domain wall in ferroelectric $(NH_2CH_2COOH)_3 \cdot H_2SO_4$. *Japanese Journal of Applied Physics*, 35:5174–5177, 1996.

[198] W. Zhang and K. Bhattacharya. A computational model of ferroelectric domains. part I: Model formulation and domain switching. *Acta Materialia*, 2004. submitted.

[199] E.B. Tadmor, U.V. Waghmare, G.S. Smith, and E. Kaxiras. Polarization switching in $PbTiO_3$: an ab initio finite element simulation. *Acta Materialia*, 50:2989–3002, 2002.